Evaluation of lift force acting on a cylindrical blade by a longitudinal vortex and examination of mechanism of lift generation

（円柱翼に作用する縦渦による揚力の評価と発生機構の解明）

Shota　NAKADA

A Thesis for the Degree of Doctor of Science of Technology Innovation
Nagaoka University of Technology
Niigata, Japan

January 2022

様式Form

論 文 内 容 の 要 旨
Abstract of Dissertation

氏　名Name　仲田翔太（Shota Nakada）

In this paper, experiments and numerical analyses were conducted to clarify the generation mechanism of longitudinal vortex acting fluid force on a cruciform circular-cylinder/strip-plate system and to improve its performance considering practical conditions of wind power generation.

Chapter 1 describes the development process of the cylindrical blade wind turbine driven by the longitudinal vortex that is the subject of this study. In addition, the position of the cylindrical blade wind turbine is shown by explaining the general wind turbine and the power generation using vortex oscillation, which has been the focus of attention in recent years.

Chapter 2 summarizes the experimental apparatus used in this paper and describes the basic experimental methods.

In Chapter 3, wind tunnel experiments were conducted to measure the rotational speed and torque of a cylindrical blade wind turbine driven by a longitudinal vortex by attaching drag-reducing components such as end plates to the blade tips, and the effect of blade tip shape factors on the power characteristics of the cylindrical blade wind turbine was clarified.

In Chapter 4, the objective is to reduce the size of the flat part of the crossed cylinder-flat plate system and to consider multi-blade. The outflow position of the longitudinal vortex was confirmed by visualization, and the necessary length of the flat plate behind the rotational direction was examined. The effect of the increase in the flow rate to the intersection on the outflow position of the longitudinal vortex was also clarified.

In Chapter 5, the objective is to clarify the suitable driving conditions for a cylindrical blade wind turbine considering the torque fluctuation. Experiments were conducted by changing the diameter of the cylindrical blade, the blade length, the width of the flat plate, the clearance ratio, and the initial rotation speed, and the temporal characteristics of the power of the cylindrical blade wind turbine were clarified.

In Chapter 6, wind tunnel experiments are conducted to confirm that flow-induced elastic vibration is induced by stationary Necklace vortex, as suggested by previous studies. A method to estimate the vibration amplitude based on the quasi-steady theory is proposed and compared with the experimental results.

In Chapter 7, to clarify the behavior of Necklace vortex in response to changes in the flow field caused by the yaw angle, a motor was attached to the rotating shaft of a cylindrical single-blade wind turbine, and the blades were forced to rotate at a specified speed to investigate the relationship between torque and blade rotation angle for various conditions determined by the flow field and rotation speed.

In Chapter 8, the important conclusions of the chapters in this paper are summarized, and the generation of longitudinal vortices and stability conditions are summarized to contribute to the improvement of performance when actually designing wind turbines.

Acknowledgments

Publications and conference data

1. Introduction

In this chapter, the important research subject of vortex excitation, which has been widely applied in the fields of mechanical engineering and civil engineering, is first explained. Next, the outflow of longitudinal vortex, its control and the longitudinal vortex excitation in the system of crossed cylinders and flat plates are explained. Furthermore, it is shown that a steady lift force acts on a cylinder moving parallel to a flat plate, and an example of the development of a circular cylinder blade wind turbine driven by this principle is described. The basic power characteristics of the circular cylinder blade wind turbine obtained from numerical analysis and experiments are also presented.

Next, the conventional types and applications of general wind turbines are presented, and the position of circular cylinder blade wind turbines is clarified. In addition, the problems of general wind turbines which are common to the circular cylinder blade wind turbines and the research examples for them are shown, and the problems to be solved for the practical use of the circular cylinder blade wind turbines are clarified. Finally, the purpose of this study and the outline of each chapter are explained.

1.1 Conventional research

In this section, the general flow-induced vibration engineering problems and the efforts that have been made for them are presented.

1.1.1 Vortex excitation and galloping and their control and applications

Among various flow-induced vibrations, the vibration of a cylinder placed in a flow is one of the most important research subjects in various fields. Therefore, a lot of research has been done on this phenomenon in order to clarify the generation mechanism and criteria of this vibration, to control dangerous vibration and to induce vibration for the purpose of energy harvesting (e.g., Bearman, 1984; Blevins, 2001). At present, there are two well known vibration mechanisms of a single cylinder in a homogeneous steady flow: vortex induced vibration (VIV) and galloping.

VIV is caused by periodic vortex outflows that occur when the cylinder is stationary. Since the periodic vortex outflow generates alternating fluid forces acting on the cylinder, the amplitude of the vibration can become very large due to resonance caused by the coincidence of the vortex outflow frequency and the natural frequency of the system. Karman vortex induced vibration (KVIV) is the most widely studied phenomenon in cylinders because of its fundamental properties and practical importance in fluid mechanics (Bearman, 2011; Dorogi and The KVIV is basically explained as a resonance, but it can also be predicted by the feedback of the cylinder motion to the excitation fluid force, such as the synchronization of the vortex outflow with the oscillation of the cylinder. However, there is no theoretical method to predict the KVIV because the vortex outflow is synchronized with the oscillation of the cylinder.

A significant engineering accident caused by VIV was the collapse of the former Tacoma Narrows Bridge, as shown in Fig. 1-1. In this accident, the KVIV of the bridge induced torsional flutter, and the bridge eventually collapsed at a wind speed that was much lower than the design limit of the wind load (Fuller et al., 2000).

Fig. 1-1 Collapse of Tacoma Narrows Bridge (Fuller et al., 2000).

In order to avoid these serious accidents, many attempts have been made to suppress the VIV. As one of the passive control methods that do not require external energy, a method to suppress vortex excitation by attaching an add-on device to the surface of a cylinder as shown in Fig.1-2 was proposed (Blevins, 1990). In addition, an attempt has been made to amplify the vibration of a cylinder by adding protrusions or projections on the surface of the cylinder to control the detachment point for energy utilization (Gang Hu et al., 2018, Wan Sun et al., 2019). Active control that requires other power sources includes the use of synthetic jets (Kim M et al., 2016) and plasma actuators (Sung Y et al., 2006). VIVACE is a typical method of energy acquisition using KVIV (Bernitsas et al., 2008).

On the other hand, the mechanism of galloping is completely different from that of VIV and is classified as fluid elastic vibration (FEV). In general, a fluid force is generated when an elastic body placed in a flow is subjected to a motion, and the motion becomes unstable when the direction of the fluid force coincides with the direction of the motion. Galloping, which is observed in a columnar object in a steady and uniform flow, is one of the most well-known oscillations in FEV, and an analytical method has been established to predict the amplitude and critical flow velocity (start of oscillation) based on the quasi-steady theory (Parkinson et al., 1964). In other words, the flow relative to a columnar object oscillating in the cross-flow direction in a uniform flow is assumed to be stationary at any phase angle of the oscillation. Then, the relative flow around the columnar object has an angle of attack, and the pressure distribution becomes asymmetric even if the cross-sectional shape of the columnar object is symmetric like a rectangular object. Therefore, if the direction of the total pressure force has a component in the direction of the oscillatory motion, the motion of the columnar

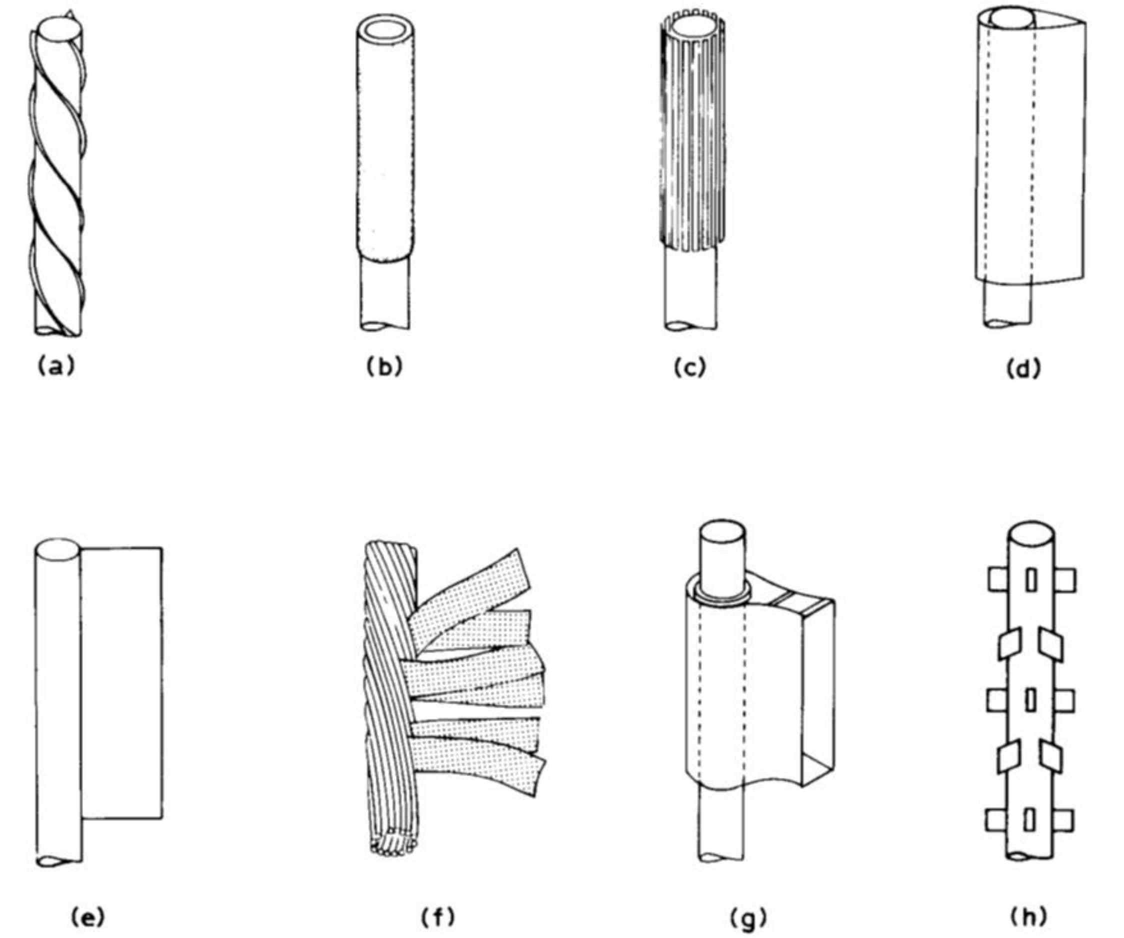

Fig. 1-2 Add-on devices for suppression of vortex induced vibration of cylinders: (a) helical strake; (b) shroud; (c) axial slats; (d) streamlined (d) streamlined fairing; (e) splitter; (f) ribboned cable; (g) pivoted guiding vane; (h) spoiler plates (Blevins, 1990).

object will be unstable and oscillation will be induced. This galloping has the following characteristics:

1) Galloping does not occur in a single cylinder, but a kind of FEV is generated in a cylinder when there is an adjacent object (Korkischko and Meneghin, 2010).

2) The velocity range of galloping is much larger than that of KVIV.

3) the oscillation frequency is fixed close to the natural frequency, which is much lower than the vortex outflow frequency;

4) the oscillation amplitude increases divergently with the flow velocity (Kawabata et al., 2013; Azhar et al., 2021)

It has also been found that there is a hysteresis region in the amplitude-velocity characteristics during prismatic galloping (Parkinson et al., 1964). It is concluded that this hysteresis region is due to intermittent shear layer reattachment (Luo et al., 2003). It has also been reported that blunt-headed objects with different cross-sectional shapes other than prisms also induce galloping (Ding et al., 2015). In particular, cylinders with point-symmetric cross-sectional shapes have been reported to induce galloping when a splitter plate is installed in the back basin or when a thin rod with a different cross-sectional shape is installed. When splitter plates were installed, the amplitude response to the converted wind speed was larger for solid plates than for slotted plates (Assi et al., 2015). When thin rods were installed at an angle of ±60 deg from the direction of wind angle of attack, it was observed that rods with triangular prisms in cross section had larger amplitudes than rods such as cylinders and prisms (Gang Hu et al., 2018).

1.1.2 Longitudinal vortex and their control

Recently, it has been found that two longitudinal vortices (LVs), i.e., Trailing vortex (TV) and Necklace vortex (NV), as shown in Fig.1-3, periodically flow out from a cruciform system with two cylinders in a uniform flow depending on the gap ratio *s/d* between the two cylinders (Koide et al., 2017; Takahashi et al., 1999) Because the two LVs generate fluid forces that act alternately on the upstream cylinder, if the upstream cylinder is elastically supported, they can induce resonant cross-flow oscillations in the upstream cylinder, which This can be characterized as a synchronous phenomenon similar to KVIV. Therefore, they are collectively referred to as longitudinal vortex excitation (LVIV), which consists of Trailing vortex excitation (TVIV) and Necklace vortex excitation (NVIV) (Kato et al. 2012; Nguyen et al. 2012). These two LVIVs have been confirmed to occur in a cross-shaped two-column system with different cross-sectional shapes, i.e., a cylinder/planar plate system (CC/SP) and a prismatic column/planar plate system (Kato et al., 2012) Among the three

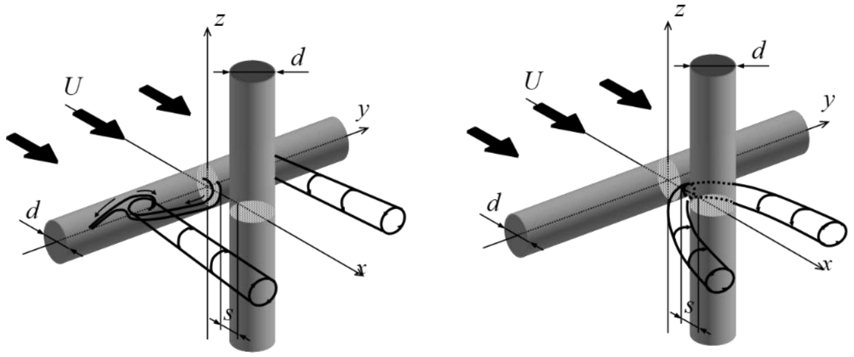

(a) Trailing vortex, s/d≤0.25 **(b) Necklace vortex, 0.25≤s/d≤0.5**

Fig. 1 -3 Longitudinal vortices from a cruciform system with two circular cylinders (Takahashi, et al., 1999)

systems, the CC/SP showed the widest TVIV velocity range (Kato et al, 2012). In this cruciform system, the method to control the vibration by the gap between the objects was investigated (Shirakashi et al., 1994, Takahashiet al., 1999, Kato et al., 2007). In the crossover system, the formation of longitudinal vortices inhibits the formation of Kalman vortices and suppresses KVIV (Bae et al., 1993).

1.1.3 Generation of steady lift force by longitudinal vortex

The LVIV has a stronger excitation force than the KVIV. Therefore, we paid attention to the strong lift force induced by the longitudinal vortex and found a method to suppress the periodicity of the longitudinal vortex and make it exist steadily at a specific position. A completely new concept of circular cylinder blade wind turbine was reported (Takahashi et al., 2016a, Takahashi et al., 2016b), which induces an orthogonal force against the uniform flow using the lift force exerted on the frontal column by the stationary longitudinal vortex as the driving force, and uses this as the rotational force.

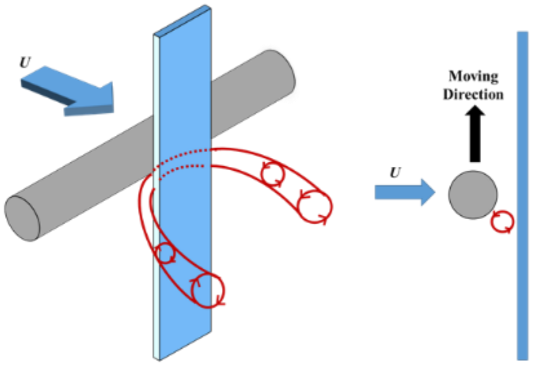

Necklace Vortex (0.25<s/d<0.5)

Fig. 1-4 Necklace vortex of cruciform system of upstream circular cylinder and downstream strip-plate.

As shown in Fig. 1-4, when the cylinder moves parallel to the wake plate with a constant gap in a uniform flow, a necklace vortex, which is one of the longitudinal vortex, is formed near the intersection and exists steadily on the opposite side of the moving direction. As a result, a steady lift force acts on the cylinder in the same direction as the movement. The details of the flow field and the lift force acting on the cylinder were clarified by numerical calculations (Hemsuwan et al., 2018a). If the wake plate is changed to a ring shape and a rotation axis is attached so that the forward cylinder can turn along it, the lift force due to the Necklace vortex becomes a rotational force and a wind turbine with the cylinder as a blade can be built. The relationship between the shape factor and the power characteristics of this wind turbine has been reported from the visualization of the longitudinal vortex and the results of performance tests (Sakamoto et al., 2021a). Furthermore, they clarified that the Necklace vortex, which generates the driving force of this wind turbine, forms a strong suction flow from the drag force acting on the cylinder and clarified the effect of the shape factor on the drag force (Sakamoto et al., 2021b). These previous studies suggested that hydrodynamically unstable oscillations are induced by stationary NV because the motion of the cylinder generates a force acting in the initial motion direction. It is also shown that the circular cylinder blade wind turbine is a low rotation, high torque type wind turbine similar to the drag type wind turbine, although it is a horizontal axis type wind turbine often used as a lift type wind turbine. When used as a wind turbine, the simple cylindrical shape of the blade makes it easy to maintain structural strength, and the blade can be fabricated from light and soft materials. Together with the low rotational speed, it is possible to design a safe and low-noise wind turbine.

1.2 Wind power generation

1.2.1 Types and characteristics of wind power

Based on the driving principle, wind turbines are classified into two types: lift-type wind turbines, where the driving force is the lift force acting on the blade, and drag-type wind turbines, where the driving force is the drag force received by the blade. In general, the tip speed of drag type wind turbines is low and less than or equal to the mainstream speed, and the maximum tip speed is about twice that of the mainstream speed (El-Askary et al., 2015). Lift-type wind turbines are driven at a high peripheral speed, which is 2~10 times higher than the mainstream speed. In some cases, wind turbines are classified into horizontal axis type and vertical axis type based on the direction of the axis of rotation relative to the main stream, not on the driving principle (Ushiyama, 2013). In general, power and torque coefficients are used to evaluate the performance of a wind turbine in relation to the tip speed ratio, which is the ratio of tip speed to mainstream speed. As shown in Fig.1-6, propeller type and Darrieus type wind turbines, which are lift type, have high rotation speed and low torque, and are suitable for rotating a generator at high speed. On the other hand, the drag type wind turbines such as

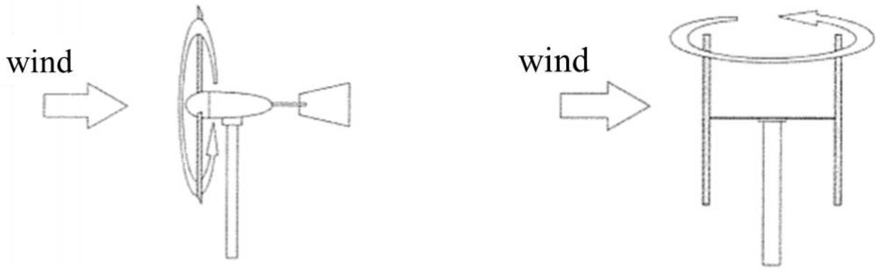

(a) Horizontal axis wind turbine (HAWT) **(b) Vertical axis wind turbine (VAWT)**

Fig. 1-5 Categorization by direction of rotation of wind turbine (Ushiyama, 2013)

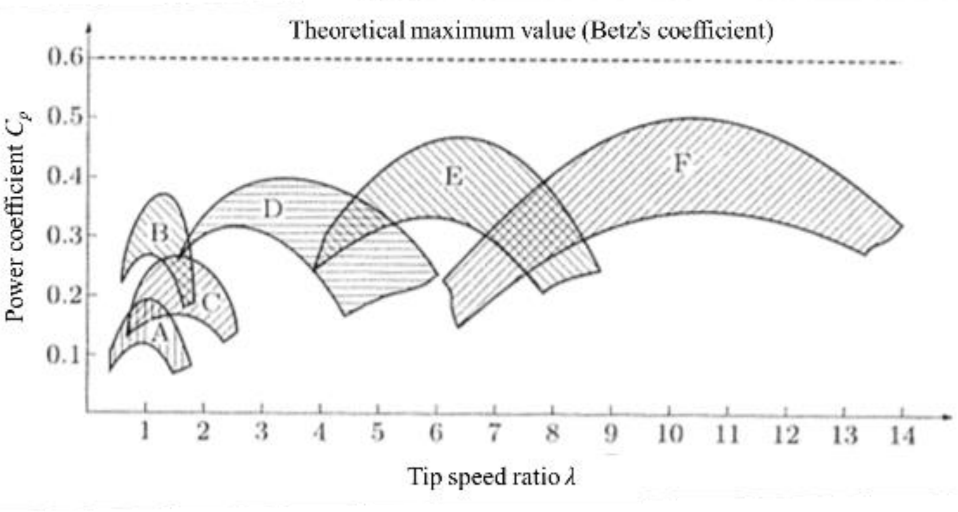

(a) Power coefficient

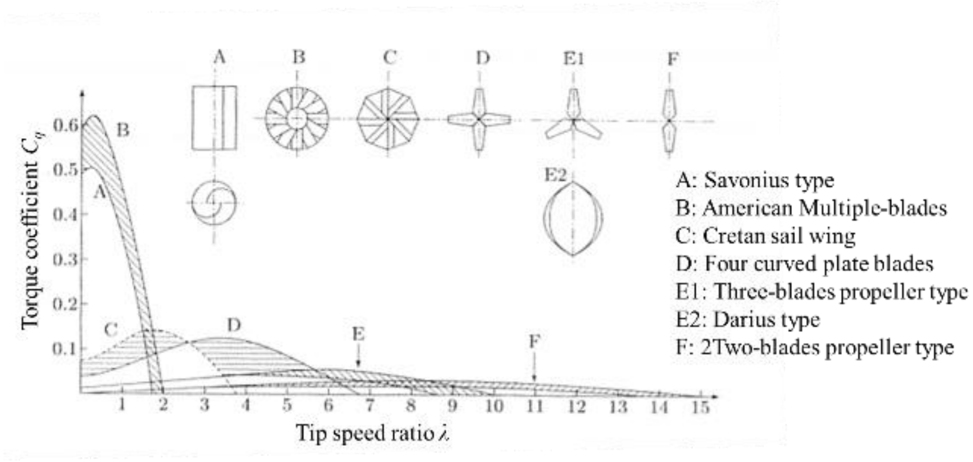

(b) Torque coefficient

Fig. 1-6 Performances of various wind turbines (Ushiyama, 2013).

Savonius and American multi-blade wind turbines have low rotation and high torque and are suitable for high load generators and pumping (Ushiyama, 2013).

1.2.2 Recent research

In this section, we will discuss the recent wind turbine and other methods using wind energy, such as the wind-lens wind turbine proposed by Ohya et al. (Ohya, 2011). The vortex near the outlet created by the diffuser at the outer edge of the wind turbine sucks in the fluid inside the diffuser and increases the internal flow velocity. By increasing the length of the diffuser, the internal velocity increases further. In order to create a high velocity in a shorter diffuser, Ohya et al. generated a large vortex at

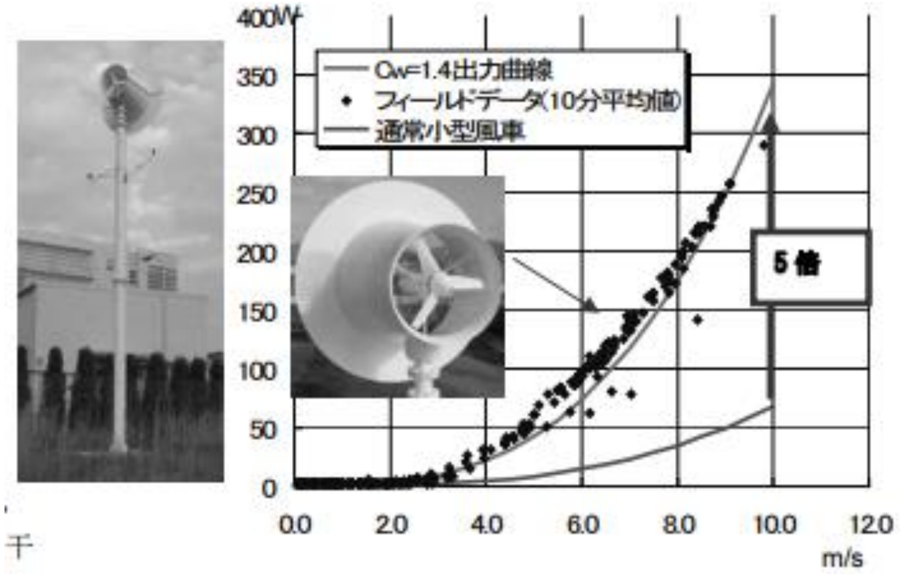

Fig. 1-7 Field experiment results of 500W wind lens wind turbine (Ohya, 2011).

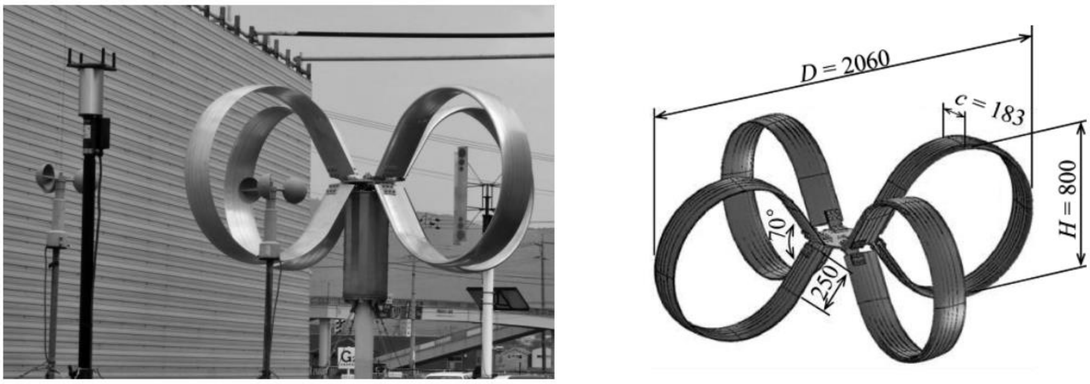

Fig. 1-8 Aluminium circular-blade butterfly wind turbine (ACBBWT) (Hara et al., 2014)

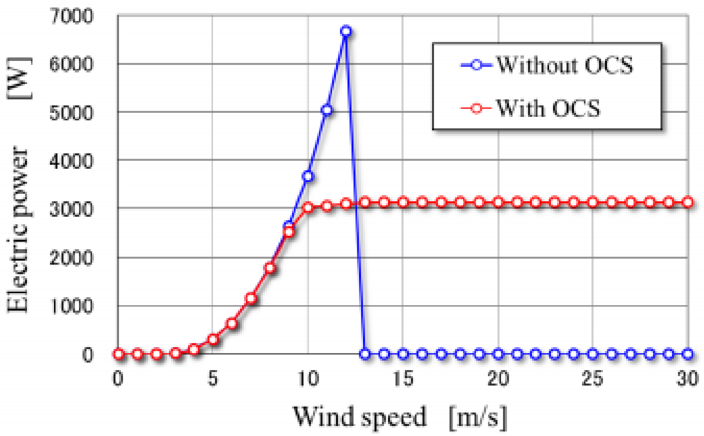

Fig. 1-9 Comparison of electric power between the BWTs with and without the over-speed control system (Hara et al., 2016).

the exit of the diffuser by attaching a brim to increase the internal velocity. As a result, the power of the wind turbine was increased by a factor of five at a flow velocity of U=10 m/s. This wind turbine not only increases the power output, but also improves the safety by avoiding bird strikes due to its high visibility to birds.

Fig.1-8 shows a vertical axis wind turbine called butterfly wind turbine (BWT) proposed by Hara et al. (Hara et al., 2014). We have developed a method to suppress the increase in the rotational speed at high wind speeds by adding an over-rotation suppression mechanism to the BWT, as shown in Fig.1-9. As shown in Fig. 1-9, it was predicted that the BWT with a radius of 3.5 m could obtain stable power at high wind speeds by suppressing the over-rotation (Hara et al., 2016).

Vortex bladeless wind turbine, shown in Fig.1-10, is a vortex-driven wind turbine similar to the circular cylinder blade wind turbine driven by a longitudinal vortex. This generator was designed to improve the efficiency of wind energy harvesting and to solve the problems of installation and maintenance of conventional wind turbines. The device uses the VIV principle to vibrate a circular cylinder in the horizontal direction, and converts it into electrical energy using an electromagnetic generator at the bottom of the cylinder. The cylinder is made of carbon fiber to reduce the weight of the device and the natural frequency, and the start-up wind speed is reduced to 3 m/s. Four types of cylinders were used and the effect of the cylinder shape on the performance was investigated, and it was found that the best performance was obtained when a rigid conical cylinder was attached to a flexible beam. (Chizfahm et al., 2018).

Fig. 1-10 The bladeless wind turbines (Chizfahm et al., 2018).

1.3 Objectives of this thesis

The purpose of this paper is to evaluate the fluid force acting on a circular cylinder blade and to clarify the mechanism of longitudinal vortex generation. The main objectives of the experiments and their contents are described below.

1. The effect of the blade tip vortex on the longitudinal vortex outflow and the fluid force was clarified by installing an end plate at the end of a circular cylinder blade and evaluating the dynamic characteristics.
2. The outflow position of the longitudinal vortex was quantitatively evaluated by changing the flat plate of the single circular cylinder blade wind turbine from the ring shape to the fin shape and conducting visualization experiments. By changing the width and angle of the fin-shaped plate, the area of the plate necessary for the fluid force to act on the cylinder was investigated. Power measurements were carried out using the fin-shaped plates.
3. The cyclic fluctuation of the longitudinal vortex was investigated by measuring the cyclic torque fluctuation during the steady rotation of a stepped circular cylinder blade. The stability of the fluid force due to the longitudinal vortex was also examined by measuring the torque fluctuation when the rotation condition was changed.
4. It is confirmed that the Necklace vortex, which is a starting condition of a circular cylinder blade wind turbine, can induce large amplitude galloping, and a prediction method of the galloping condition is proposed.
5. The fluid forces were measured when the wind turbine had a Yaw angle, and the conditions for the generation and disappearance of the longitudinal vortex were investigated under more practical conditions.

The results of the above research will accumulate basic knowledge about the circular cylinder blade wind turbine powered by the longitudinal vortex, for which the operating principle has just been proposed and the research has just started, and will provide information on improving the efficiency and optimizing the operating conditions for practical use.

1.4 Overview of each chapter

This paper is composed of eight chapters. The main contents in each chapter are as follows.

Chapter 1: Introduction

This paper describes the development process of circular cylinder blade wind turbines driven by longitudinal vortices, and shows the position of circular cylinder blade wind turbines by explaining general wind turbines and power generation using vortex induced vibration, which has been the focus of attention in recent years.

Chapter 2 Experimental apparatus and procedure

The conditions and procedures related to the experiments necessary for the discussion of this paper are described, and the methods compared with previous literature are discussed.

Chapter 3 Verification of the Blade Tip Effect on the Power of a Circular cylinder Blade Wind Turbine Driven by a Longitudinal Vortex

The power characteristics of a stepped circular cylinder blade wind turbine were measured by attaching an attachment to the blade tip, and the performance improvement by changing the shape was investigated.

Chapter 4: Effect of Fin Type Flat Plate on Power Characteristics of Single Circular cylinder Blade Wind Turbine

The required length of the flat plate was investigated by making the plate fin-like and confirming the outflow position of the longitudinal vortex by visualization experiments. In addition, the power characteristics were measured and the performance improvement by the fin-shaped plate was examined.

Chapter 5 Effects of Geometry and Load Variation on Power Fluctuation Characteristics of a Stepped Circular cylinder Blade Wind Turbine

The relationship between the cyclic fluctuation of the torque generated during the steady-state rotation of a wind turbine and the operating conditions of the wind turbine is clarified from experiments, and the recommended conditions for driving the wind turbine are presented. In addition, the stability of the torque when the rotating condition of the wind turbine is suddenly changed is investigated.

Chapter 6: Generation of galloping using necklace vortex

A prediction method of the fluid force acting on a cylinder moving along a flat plate is proposed based on the measurement results of the fluid force.

Chapter 7: Elucidation of Wind Direction Characteristics

The effect of the cyclic variation of the relative wind speed on the power characteristics was clarified from the experiment when there is a Yaw angle in the mainstream velocity flowing into the wind turbine. The generation and disappearance conditions of the longitudinal vortex were also investigated from the change of the fluid power during one cycle.

Chapter 8 Conclusion

The characteristics obtained from the experimental results in each chapter are summarized, and the conditions for the generation of the longitudinal vortex and the stability of the wind turbine are clarified. In addition, the points to be considered for the improvement of the performance are summarized, and the knowledge for the practical use of the circular cylinder blade wind turbine is shared.

Chapter 1 References

Azhar, M., Sheikh Ahmad Zaki, Shirakashi, M., Mohamed Sukri Mat Ali, Muhammad Zulfahmi Samsudin, Ahmad Faiz Mohammad, 2021. Experimental investigation on vortex-induced vibration and galloping of rectangular cylinders of varying side ratios with a downstream square plate. J. Wind Eng. Ind. Aerodynamics, 211, 104563, 27 pages.

Bae, H. M., Takahashi, T. and Shirakashi, M., Suppression of Karman vortex excitation of a circular cylinder by another cylinderlocated downstream in cruciform arrangement, Transactions of the Japan Society of Mechanical Engineers, Series B, Vol. 59, No. 557 (1993), pp. 1-7 (in Japanese)

Bearman, P., 1984. Vortex shedding from oscillating bluff bodies, Annu. Rev. Fluid Mech. 16, 195-222. http://dx.doi.org/10.1146/annurev.fl.16. 010184.001211.

Bernitsas, M. M., Raghavan, K., Ben-Simon, Y. and Garcia, E. M. H., VIVACE (Vortex Induced Vibration Aquatic Clean Energy): a new concept in the generation of clean and renewable energy from fluid flow, Journal of Offshore Mechanics and Arctic Engineering, Vol. 130, Issue 4 (2008), 041101.

Blevins, R., 2001. Flow-Induced Vibration, second ed. Krieger Publishing Company, Florida.

Bearman, P., 2011. circular cylinder wakes and vortex-induced vibrations. J. Fluid Struct. 27 (5-6), 648-658. http://dx.doi.org/10.1016/j. fluidstructs.2011.03.021.

Chizfahm, A., Yazdi, A. E., and Eghtesad, M., Dynamic modeling of vortex induced vibration wind turbines, Renewable energy, Vol. 121 (2018), pp. 632-643

Dorogi, D. and Baranyi, L., 2020. Identification of the upper branch for vortex-induced vibration of a circular cylinder at Re=300. J. Fluids and Struct. 98, 27pages. https://doi.org//10.1016/j.jfluidstructs.2020.103135.

Gabbai, D. and Benaroya, H., 2005. An overview of modeling and experiments of vortex-induced vibrations of circular cylinders. J. Sounds and Vibr. 282, 575-616.

Gang Hu, K.T. Tse, Minghai Wei, R. Naseer, A. Abdelkefi, K.C.S. Kwok, 2018, Experimental investigation on the efficiency of a circular cylinder-based wind energy harvester with different rod-shaped attachments, Applied Energy, 226, 682-689

Hara, Y., Shiozaki, A., Nishiono, H., Saito, S., Shioya, K., Kogo, S. and Takagaki, K., Experiments of a Butterfly Wind Turbine with Aluminium Circular Blades and Performance Predictions, Journal of JWEA, Vol.38, No.1 (2014), pp.16-21 (in Japanese)

Hemsuwan, W., Sakamoto, K. and Takahashi, T., Numerical investigation of lift-force generation on a moving circular cylinder in a uniform flow driven by longitudinal vortex, Journal of Fluids and Structures, Vol. 83, Issue 20 (2018a), pp. 448-470.

Kawabata, Y., Takahashi, T., Haginoya, T., Shirakashi, M., 2013. Interference effect of downstream strip-plate on the crossflow vibration of a square J. Fluid Science and Technology, JSME, 8 (3), 348-363.

Kato, N., Koide, M., Takahashi, T. and Shirakashi, M., Vibration control for a circular cylinder by a strip-plate set downstream in cruciform arrangement : 1st report, Influence of a downstream strip-plate on the shedding of longitudinal vortices from fixed system, Transactions of the Japan Society of Mechanical Engineers, Series B, Vol. 73, No. 728 (2007), pp. 957-964 (in Japanese)

Kato, N., Koide, M., Takahashi, T., Shirakashi, M., 2012. VIVs of a circular cylinder with a downstream strip-plate in a cruciform arrangement. J. Fluids. Struct. 30, 97-114.

Kim M, Lee B, Lee J, Kim C (2016) Experimental and computational study on separation control performance of synthetic jets with circular exit. Int J Aeronaut Sp Sci 17(3):296-314.

Koide, M., Takahashi, T., Shirakashi, M. and Sheikh Ahmad Zaki Bin Shaikh Salim, 2017. Three-dimensional structure of longitudinal vortices shedding from cruciform two-cylinder systems with different geometries. J. Visualization Society, Japan. 20 (4), 753-763.

Korkischko, I., Meneghin, J. R., 2010. Experimental investigation of flow-induced vibration on isolated and tandem circular cylinders fitted with strakes. J. Fluids Struct. 26 (4), 611-625.

Lin Ding, Li Zhang, Chunmei Wu, Xinru Mao, Deyi Jiang, 2015, Flow induced motion and energy harvesting of bluff bodies with different cross sections, Energy Conversion and Management 91 416-426

Morse, L. and Williamson, C.H.K., 2009. Fluid forcing, wake modes, and transitions for a cylinder undergoing controlled oscillations. J. Fluids and Struct. 25, 697-712.

Nguyen, T., Koide, M., Takahashi, T., Shirakashi, M., 2012. Influence of mass and damping ratios on VIVs of a cylinder with a downstream counterpart in cruciform arrangement. J. Fluids Struct., 28, 40-55.

Ohya, Y., New wind turbine with wind-lens technology, Wind Engineers, JAWE, Vol.36, No.1 (No.126) (2011), pp.19-22

Parkinson, G.V., Smith, J.D., 1964. The square prism as an aeroelastic nonlinear oscillator, Quart. J. Mech. Appl. Math., (17), 225-239.

Robert D. Blevins, 1990. Flow Induced Vibration, Van Nostrand Reinhold Inc. v. U.S.

Robert G. Fuller, Charles R. Lang, Roberta H. Lang, 2000. Twin Views of the Tacoma Narrows Bridge Collapse, American Association of Physics Teachers, US.

Sakamoto, K., Udaka, K., Hemsuwan, W. and Takahashi T., Development of circular cylinder blade wind turbine driven by longitudinal vortex, Transactions of the JSME, Vol. 87, No. 894 (2021a) DOI:10.1299/transjsme.20-00365

Sarpkaya, T., 2004. A critical review of the intrinsic nature of vortex-induced vibrations, J. Fluid Struct. 19 (4), 389-447.

Shirakashi, M., Bae, H. M., Sano, M. and Takahashi, T., Characteristics of periodic vortex shedding from two cylinders in a cruciform arrangement, Journal of Fluids and Structures, Vol. 8, Issue 3 (1994), pp. 239-256.

S.C. Luo, Y.T. Chew, Y.T. Ng, 2003, Hysteresis phenomenon in the galloping oscillation of a square cylinder, JFS 18 103-118

Sung Y, Kim W, Mungal MG, Cappelli MA (2006) Aerodynamic modification of flow over bluff objects by plasma actuation. Exp Fluids 41:479-486 Fluids 41:479 -486.

Takahashi, T., Baranyi, L., Shirakashi, M., 1999. Configuration and frequency of longitudinal vortices shedding from two cylinders in a cruciform J.Visual. Soc. Jpn. 19(75), 328-336.

Takahashi, T., Yoshitake, Y., Komata, N. and Ueki, Y., Rotary device for fluid power generation and fluid power generation Device, Japanese Patent Application No. 2016-568339 (2016a).

Takahashi, T., Yoshitake, Y., Sakamoto, K. and Hemsuwan, W., An innovative wind/water turbine with circular propeller driven by longitudinal vortex, Proceedings of the 15th WWEC2016 TOKYO conference (2016b), PS-A-5.

Ushiyama, Izumi, 2013. Introduction to Wind Turbine Engineering, 2nd Edition - From Basic Theory to Operational Know-How, Morikita Publishing Corporation, pp. 1~5, 46~65.

W.A. El-Askary, M.H. Nasef, A.A. AbdEl-hamid, H.E. Gad, 2015, Harvesting wind energy for improving performance of Savonius rotor, J. Wind Eng. Ind. Aerodyn. 139, 8-15

Wan Sun, Soohwan Jo, Jongwon Seok, 2019, Development of an optimal bluff body for wind energy harvesting using the synergetic effect of coupled vortex induced vibration and galloping phenomena, International Journal of Mechanical Sciences, 156, 435-445

2. Experimental equipment

2.1 Wind Tunnel Experimental Apparatus

An experiment was conducted using a blowout type wind tunnel apparatus as shown in Fig. 2-1. The exit of the wind tunnel is a square with a side of 350 mm. The diameter of the test section is a square with 320 mm on one side, which is smaller than the wind tunnel outlet, to prevent the boundary layer near the wall of the wind tunnel outlet from entering the test section. The length of the test section is 1200 mm. The wind speed range of the experiment is from 2 m/s to 20 m/s. The turbulence intensity at 2 m/s is 0.6 %, and that at wind speeds above 11 m/s is 0.3 % (Kato et al., 2012). Mainstream velocities for the experiments were measured by a ring anemometer (Koide et al., 2001) at a location 200 mm downstream from the entrance of the test section.

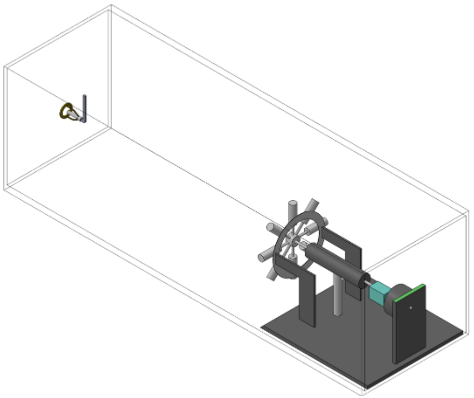

Fig. 2-1 Schematic diagram of test section and wind turbine setting.

2.2 Wind turbine equipment

2.2.1 Single circular cylinder blade wind turbine

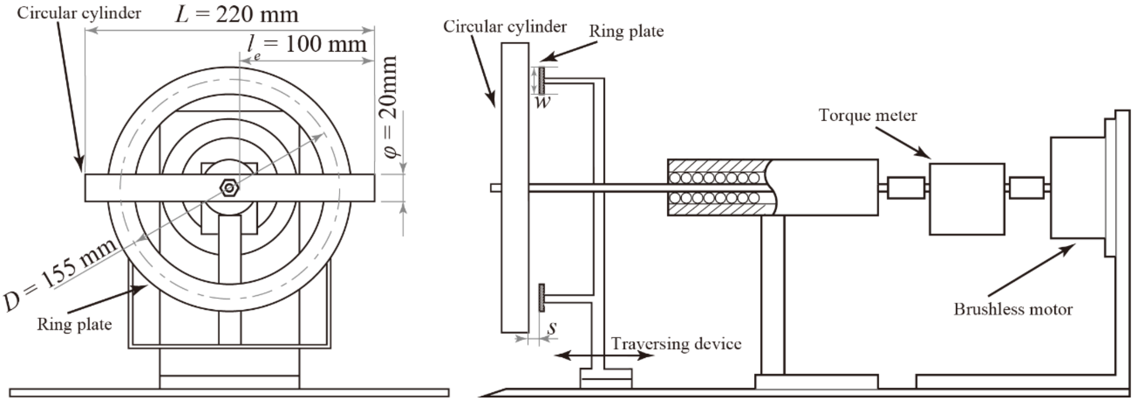

Fig. 2-2 Wind-turbine-type system for fluid-force measurement.

The single circular cylinder blade wind turbine shown in Fig.2-2 was used for the fluid force measurement. This device is a single circular cylinder blade wind turbine driven by a longitudinal vortex, which was developed by Sakamoto et al. The upstream cylinder has a diameter d = 20 mm and a length L = 220 mm, and the downstream ring-shaped plate has a width $w = d$, a thickness t = 3 mm, and a central diameter D = 155 mm. The gap s between the cylinder and the ring plate was set to an arbitrary value by the traverse device. The dimensions of the device are shown in Table 2-1. The wind turbine is installed in the test section of the wind tunnel, and the rotational plane of the wind turbine is located 840 mm downstream from the entrance of the test section. The center of the rotation axis is located at the center of the test section.

Table 1Dimensions of wind-turbine-type measurement system.

Diameter of upstream cylinder, d [mm].	20
Diameter of ring plate, D [mm]	155
Circular cylinder length, L [mm].	220
Effective blade length, l_e[mm].	100
Ring plate width, w [mm].	20

2.2.2 Stepped circular cylinder blade wind turbine

The blade of the wind turbine shown in Fig. 2-3 is a stepped circular cylinder blade that has been reported to stabilize the Necklace vortex by Sakamoto et al. The inside of the cylinder is used as a support part to fix the wing and as a thin cylinder to reduce drag. The wing part is a cylinder with a diameter of d=20 mm and an effective length of *l,* and the support part is a thin cylinder with a *diameter of* 6 mm connected concentrically. The supports are radially fixed to a hub of 30 mm diameter attached to the rotating shaft. The ring-shaped flat plate installed in the wake of the circular cylinder blade has a central diameter of D=155 mm, a thickness of t=3 mm, and a width of W=20 mm. The center of the effective length of the cylinder coincides with the center of the width of the ring-shaped plate. The gap *s* between the ring-shaped plate and the circular cylinder blade is set so that the ratio of *s/d* to the cylinder diameter is 0.35.

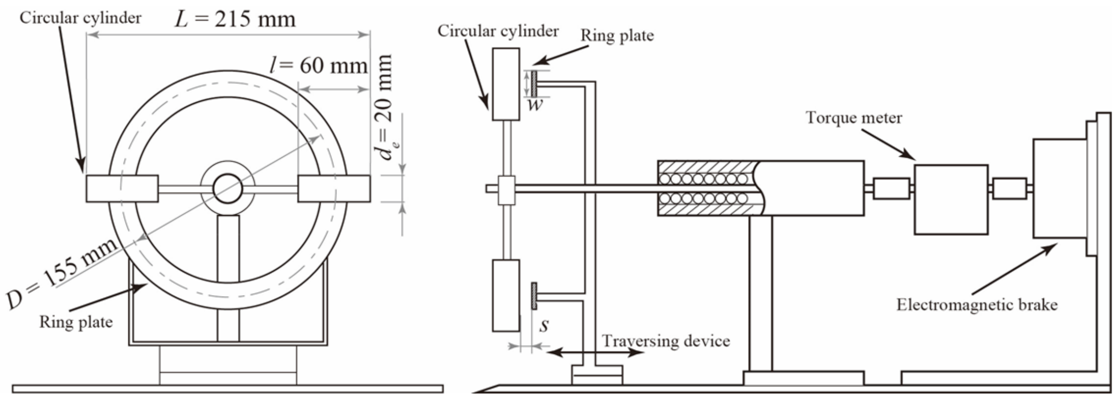

Fig. 2-3 Schematic diagrams of stepped cylinder blades wind turbine and measurement instrument.

2.2.3 Fin type flat plate - circular cylinder blade wind turbine

The effect of the flat plate shape on the power characteristics is investigated using the finned circular cylinder blade wind turbine shown in Fig.2-4. When the fin shape is used for the flat plate, the fluid force due to dynamic pressure is expected to increase by bending the upper part of the flat plate. In addition, an end plate is installed at the blade tip to serve as a support, which simultaneously suppresses the blade tip vortex. Furthermore, the connection between the support and the flat plate was made 10 mm thinner than the circular cylinder blade diameter d=20 mm, and the upper end of the connection was aligned with the edge of the circular cylinder blade projected in the mainstream direction to limit the outflow point of the longitudinal vortex and control the direction of rotation.

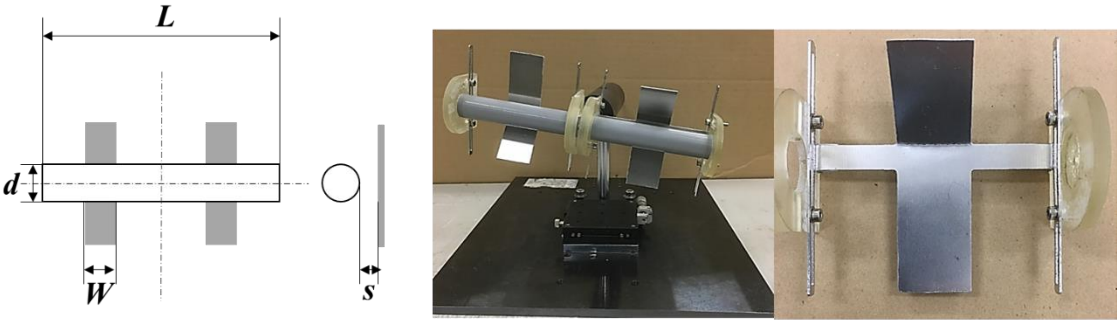

Fig. 2-4 Schematic diagrams and photographs of fin attached cylinder blade wind turbine.

2.2.4 Pendulum-type amplitude measurement device

A pendulum-type apparatus shown in Fig.2-5 was used for the vibration experiment. A cylinder of diameter d and length $l=5d$ was suspended from an aluminum rod of 5 mm in length with a square cross section and fixed to a bearing. The radius of the rotational motion, R=250 mm, was set at the middle of the span of the cylinder. The displacement of the rod at the top of the bearing was measured with a laser displacement meter (OMRON ZX-LD100), and the output signal was converted into the displacement angle θ using a previously obtained calibration curve.

An electromagnetic damper was used to control the damping coefficient. An aluminum plate with a thickness of 1.4 mm was attached to the top of the square bar. The damping coefficient was set to an arbitrary value by adjusting the length of the aluminum plate in the magnetic field.

An arc-shaped aluminum plate with a width of $w = d$, a chord length of 280 mm, and a thickness of 5 mm was used as the plate that crosses the cylinder at the downstream side. The radius of the centerline of the arc plate is R, which is the same as the radius of rotation, and the arc plate is attached to the downstream side of the pendulum with a gap s that can be adjusted by the traverse device. The pendulum was installed in a frame on the upper wall of the test section of the wind tunnel as shown in Fig. 2-5.

The pendulum-type device was modeled as a point mass suspended by a zero-mass string. The effective mass m_e, natural frequency f_n and logarithmic damping coefficient δ of the simplified model I were determined based on the free-damping vibration in air at rest (i.e., U = 0 m/s) as follows The

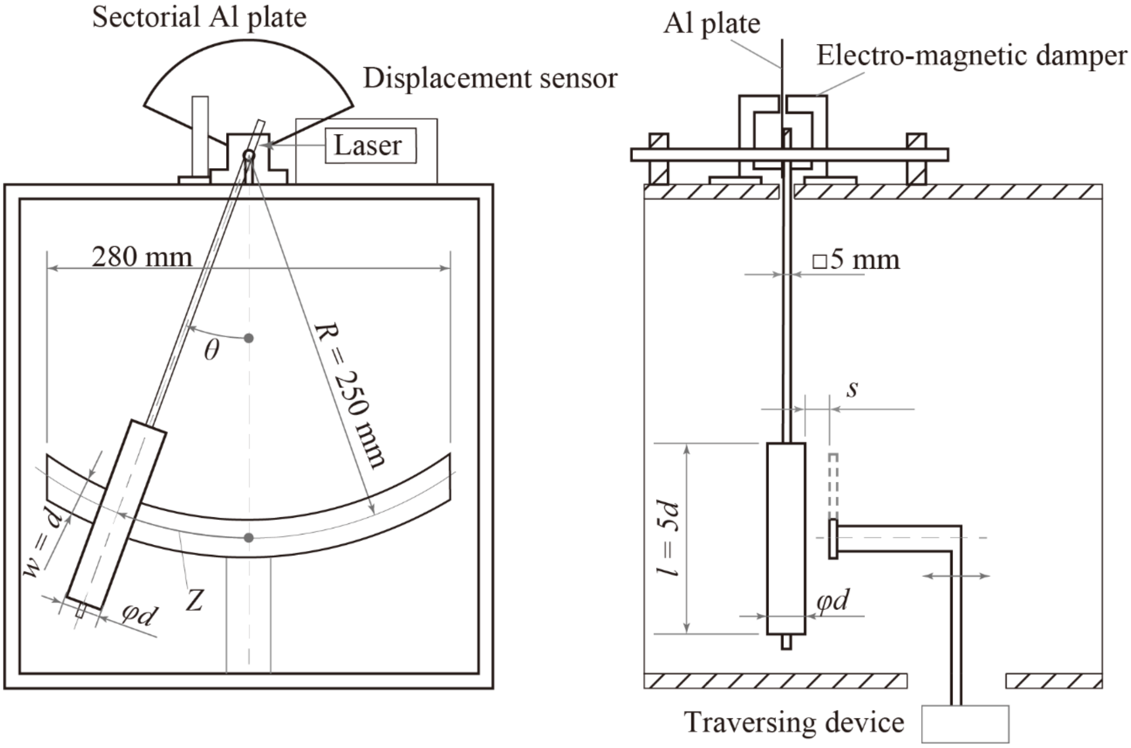

Fig. 2-5 Pendulum-type measurement system for vibration experiment.

natural frequency f_n and the logarithmic damping coefficient δ *were* determined from the oscillogram of the free-damped vibration displacement $Z = R\theta$. Then, the effective mass m was $_e$calculated using Equation (2-1).

$$m_e = 1/\{(2\pi f_n)^2 k\} \tag{2-1}$$

Here, k *is the* virtual spring constant of the pendulum-type device, which is calculated by $k=mg/R$. It was confirmed that the mass m *of the* cylinder measured separately was almost equal to m_e. Therefore, $m = m_e$ was used to simplify the analysis. The dynamic characteristics of the two pendulum-type devices determined in this way are shown in Table 2-2. The mass ratio was determined as follows.

$$m_e^* = m_e/(\rho\, dl) \tag{2-2}$$

where ρ *is the* density of air.

The flow velocity, U, *was* increased in steps to a predetermined maximum value (approximately U=4 m/s for Model I and approximately 6 m/s for Model II). These maximum velocities were determined from the maximum allowable amplitude of the experimental apparatus. In this procedure, the pendulum cylinder remained almost stationary until the maximum flow velocity was reached under all experimental conditions. Then, the pendulum cylinder was subjected to a constant displacement and the final displacement was measured. When a stable oscillation with a large amplitude was finally obtained, the flow velocity U was decreased step by step until the oscillation was stopped. In this study, the amplitude of the vibration was expressed as the root mean square of the displacement Z measured along the centerline of the arc plate, as shown in Fig.2-5. The vibration frequency f_c was set to the highest peak frequency in the power spectrum of the output signal of the displacement sensor.

Table 2-2 Dimensions and dynamic characteristics of pendulum-type measurement systems.

	Model I	Model II
Diameter of upstream cylinder d [mm].	26	18
Cylinder length l [mm]	130	90
Arc plate width w [mm].	26	18
Pendulum length R [mm].	250	250
Elastic modulus k [N/m].	2.33	1.07
Effective mass m_e[kg].	0.059	0.025
Natural frequency f_n[Hz].	0.957	0.951
Mass ratio m_e*	714	912

2.3 Measuring instruments

2.3.1 Power measurement equipment

In order to measure the torque and rotation speed acting on the rotating shaft, the drive side of a torque transducer (UTM II-0.2 N・m, Unipulse Co., Ltd.) was attached to the rotating shaft of the wind turbine, and an electromagnetic brake (HB2.5, OGURA CLUTCH Co., Ltd.) was attached to the load side of the torque transducer. The electromagnetic brake (HB2.5, OGURA CLUTCH Co. A stabilized power supply is attached to the electromagnetic brake, and the brake is loaded when voltage is applied.

2.3.2 Power adding device

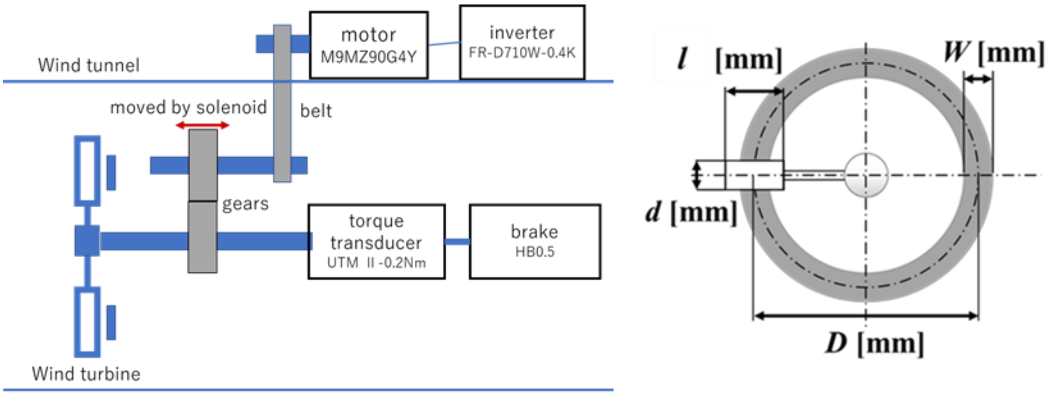

Fig. 1-6 Schematic diagram of the equipment for the load control experiment.

As shown in Fig.2-6, the load of the wind turbine is controlled by the voltage applied to the electromagnetic brake connected to the rotating shaft of the wind turbine, and the rotation speed and torque are obtained by the torque converter. In addition, a three-phase motor (M9MZ90G4Y, Panasonic Co., Ltd.) is installed in parallel via a gear attached to the rotating shaft. An inverter (FR-D710W-0.4K, Mitsubishi Electric Co., Ltd.) was used to control the motor speed. The gears that connect the motor to the rotating shaft can be disconnected instantly by a solenoid.

2.4 Experimental procedure

2.4.1 Measurement method of wind turbine driving force

A load is applied to a wind turbine device rotating steadily in a uniform flow by an electromagnetic brake to suppress the rotation speed, and the rotation speed and torque are obtained from a torque meter when the rotation speed becomes steady. The load is increased step by step and the same operation is repeated until the rotation is stopped. From these outputs, the tip speed ratio λ defined by Equations (2-3) and (2-4), the torque coefficient C_q and the fluid force coefficient C_z are calculated, the power characteristics are obtained for λ, *and the* effect of each parameter that has been changed is evaluated from the change.

$$\lambda = \frac{\pi D m}{U} \tag{2-3}$$

$$C_q = \frac{T}{0.5 \rho U^2 A R} \tag{2-4}$$

2.4.2 Visualization Experiment

In the finned circular cylinder blade wind turbine shown in Fig.2-4, it was expected that the longitudinal vortex outflow position could be controlled by the support, so the vortex outflow position on the flat surface was visualized using the oil film method. To process the visualization results, the distance from the top of the connection to the vortex shedding position was measured at three points, using the 10 mm width of the connection as a reference, and the average value was calculated as a

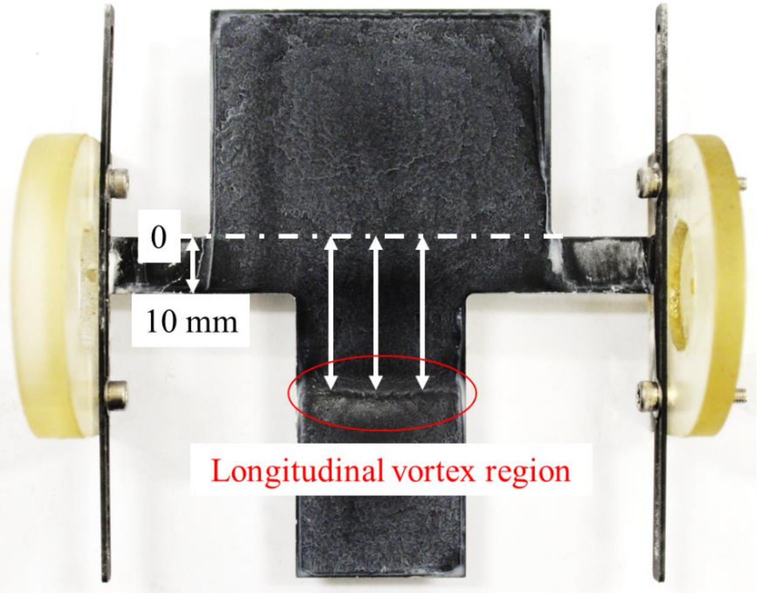

Fig. 2-7 Measurement method from the reference point to the shedding position of the longitudinal vortex

ratio to the circular cylinder blade diameter. Examples of the measurements are shown in Fig. 2-7.

2.4.3 Measurement method of driving force fluctuation

It is known that instantaneous torque fluctuations are repeated periodically even when the wind turbine in this study is rotating at a steady rotation speed in time. By applying Fourier analysis, which is a frequency analysis method, to the time-varying torque waveform, the natural frequency and the fluctuation frequency of the lift force due to the longitudinal vortex were obtained. On the other hand, the time information is lost in Fourier analysis. Time and frequency analysis such as short-time Fourier analysis and wavelet transform is necessary to clarify the phenomena that depend on time progression such as the periodicity of the formation and state change of the longitudinal vortex and the duration of the lift force associated with it. As an example of the application of time-frequency analysis to fluid-related oscillations, there is a report that uses wavelet analysis for fluctuating wind velocity caused by vortices flowing out behind a cylinder to distinguish between galloping and Karman vortex excitation (Matsumoto et al., 2008). In this study, wavelet analysis using morlet wavelets was performed on the time series of torque in order to quantitatively evaluate the phenomenon of temporal variation of torque of a wind turbine driven by a longitudinal vortex.

2.4.4 Load change experiment

Two shape factors, the gap ratio (*s/d)*, which consists of the diameter of the circular cylinder blade (*d)* and the gap between the blade and the ring-shaped plate (*s),* and the *l/W,* which consists of the blade length *(l)* and the width of the ring-shaped plate (*W), are* investigated as the shape factors affecting the power stability of a horizontal-axis circular cylinder blade wind turbine. As static characteristics related to each shape factor condition, the torque and power coefficients against the rotation speed, which vary depending on the load applied to the electromagnetic brake, were obtained. The no-load rotation speed is N_{max} and the maximum load rotation speed is N_{tmax} at this time. Next, the initial rotation speed *Ni* and the steady rotation speed *Ns* by the load given to the electromagnetic brake are examined as the factors that affect the temporal stability of the power in the wind turbine. The load was controlled to be 50 rpm increments from N_{max} to N_{tmax} obtained from the static characteristics, and the temporal change from the initial rotation speed *Ni* forced by the motor to the final steady-state rotation speed *Ns was* measured under the constant load condition. The starting point was the point where the torque was detected when the forced rotation was unloaded, and the time constant τ was used to compare the change in rotation speed ΔN up to 36.8% for $Ni>Ns$ and up to 63.2% for $Ni<Ns$. *The* experimental sequence, the definition of each value and an example of the time constant calculation from the measured transient response are shown in Fig.2-8.

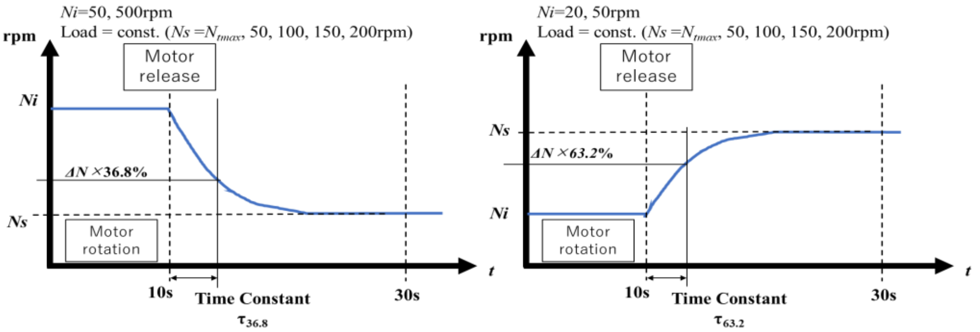

(a) Experimental sequence at *Ni*>*Ns* (b) Experimental sequence at *Ni*<*Ns*

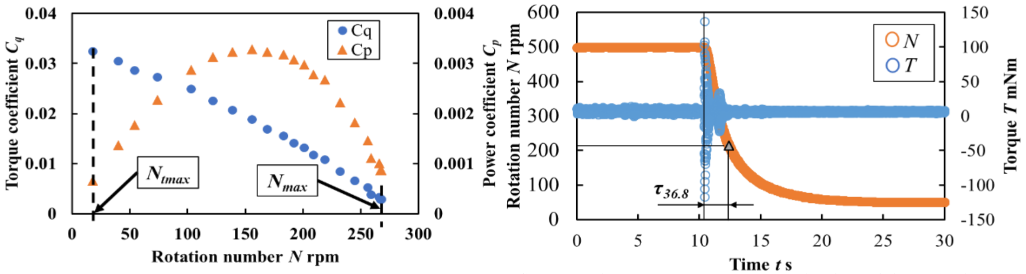

(c) Static characteristics of wind turbine. (d)Transient response of wind turbine (Ni=500 rpm, Ns=50 rpm).

Fig.2-8 Experimental sequence and Experimental results of statistic characteristics and transient response at s/d=0.35, d=20 mm, W=30 mm, l=60 mm.

2.5 Numerical Analysis

In order to observe the state of the longitudinal vortex in relation to the dynamic characteristics obtained in the experiment, a numerical analysis using the same conditions was conducted. SCRYU/Tetra v14.1 and scFLOW v2021, which are general-purpose thermo-fluid analysis software, were used for the numerical analysis. The detailed conditions of the numerical analysis are shown in each chapter.

Chapter 2 References

Matsumoto, M., Yagi, T., Hashimoto, M., Nakase, T. and Maeta, K., Effects of karman vortex on bluffbody aerodynamics, Proc. of the 20th National Symposium on Wind Engineering (2008), p.61

Kato, N., Koide, M., Tahkahashi, T. and Shirakashi, M., VIVs of a circular cylinder with a downstream strip-plate in cruciform arrangement, Journal of Fluids and Structures, Vol. 30 (2012), pp. 97-114.

Koide, M., Takahashi, T. and Shirakashi, M., Development of a ring-type vortex anemometer for low-velocity wind tunnel experiment, Transactions of the Japan Society of Mechanical Engineers, Series B, Vol. 67, No. 657 (2001), pp. 1105-1111 (in Japanese).

Sakamoto, K., Hemswan, W., Takahashi, T., Development of a wind turbine driven by longitudinal vortex: Wind tunnel experiment to investigate the basic J. Wind Eng. Ind. Aerodynamics, 210, 104492 (2021a) 15 pages.

Sakamoto, K., Hemsuwan, W. and Takahashi T., Drag force of circular cylinder blade wind turbines driven by steady lift force of longitudinal vortex, Transactions of the JSME, Vol. 87, No. 894 (2021b) DOI: 10.1299/transjsme.20-00375

3. Effect of blade tip on power of circular cylinder blade wind turbine driven by longitudinal vortex

3.1 Chapter 3 Introduction

A method to improve the blade tip effect and increase the power of a general horizontal axis wind turbine has been proposed by adding a propeller blade shape and auxiliary equipment. Ohya et al. (Ohya et al., 2011) reported that a wind-lens wind turbine with a blade tip covering structure increased the power output by 30 % compared with a conventional wind turbine in an experiment using a 2.5 m class wind turbine with a 5 kW rating, and also reduced blade tip vortices and improved safety. Nishizawa et al. (Nishizawa et al., 2009a) showed that the power output of a small horizontal axis wind turbine could be improved by installing a plate at the blade tip. The blade shape was tapered toward the tip, and a blade tip plate was installed at the tip toward the wake direction. Two-, three-, four-, and five-bladed wind turbines designed with a turning radius of 0.03 m and a tip speed ratio of λ =2~3.4 were compared at a mainstream velocity of U =10 m/s. The results showed that the power coefficient of the six-bladed wind turbine increased by 0.8 % and that of the four-bladed wind turbine increased by 3.2 %. Furthermore, it was reported that the maximum power coefficient at low wind speeds was significantly increased by using a winglet shaped end (Nishizawa et al., 2009b).

A typical wind turbine using a cylinder as a blade is the Magnus effect wind turbine. Nicolas et al. (Nicolas et al., 2012) investigated the effect of the aspect ratio of the cylinder, the diameter ratio of the end plate, and the ratio of the rotational speed on the lift force by installing an end plate at the blade end of the rotating cylinder. The effect of the ratio of the aspect ratio of the cylinder, the diameter ratio of the end plate, and the rotation rate on the lift was investigated. It was reported by the numerical analysis that the drag force decreased and the lift force increased by increasing the diameter of the end plate, and the drag force was large and the lift force was small for the cylinder with a small aspect ratio. In addition, it was shown that the induced drag was increased by increasing the amount of rotation to generate stronger blade tip vortices. Wenjun et al. (Wenjun et al., 2018) investigated numerically the flow field around a single cylinder of finite length with two free ends, and found that the vortices flowing out from the ends changed depending on the aspect ratio. They reported that when the aspect ratio *L/D* becomes smaller than 10, the three-dimensional flow from the end surface develops over the whole cylinder.

Furthermore, for a cylinder that is not a wind turbine but moves parallel along a flat plate, Hemsuwan et al. (Hemsuwan et al., 2018) showed numerically that the Trailing vortex flowing out from near the end of the cylinder interferes with the vortex flowing out from the end face and generates a negative lift coefficient at the end. They further showed that the lift-drag ratio can be improved by 5.5 % by installing a disc-shaped or L-shaped end plate at the end.

In this paper, wind tunnel experiments are conducted to measure the rotational speed and torque of a circular cylinder blade wind turbine driven by a longitudinal vortex by attaching drag-reducing components such as end plates to the blade tips, and the effect of the shape factor of the blade tips on the power characteristics of the circular cylinder blade wind turbine is clarified. Here, all the components that are individually attached to each blade tip are defined as end plates, and are classified as disc-shaped, L-shaped, or arc-shaped L-shaped depending on their shapes. First, the effect of the fairing that covers the blade is examined as a measure to improve the drag at the blade tip. We thought that an end plate, which can be installed on each blade individually, would be more appropriate than a fairing that covers the entire circumference of the blade. Experiments were conducted to determine the power characteristics when various shapes of attachments were installed on the circular cylinder blade ends, and the performance improvement by changing the shapes was investigated.

3.2 Experimental apparatus and procedure

3.2.1 Equipment for measuring blade tip shape and power characteristics

To investigate the power characteristics of a circular cylinder blade wind turbine driven by a longitudinal vortex, a device capable of measuring the rotation speed and torque of the rotating shaft shown in Fig. 2-3 was used. Table 3-1 shows the dimensions of the wind turbine used in the experiment.

Table 3-1 Experimental setup.

Gap ratio *s/d* [-].	0.35
Ring pate width *W* [mm].	20
Blade diameter *d* [mm]	20,25,28
Blade length *l* [mm]	60,80
Ring plate diameter *D* [mm]	155
Blade Number *N* [-].	Two, four, eight.

A fairing-like attachment and an end plate covering the blade tip were prepared to reduce the drag at the blade tip. An overview of the modified wind turbine is shown in Fig. 3-1 to investigate the effect of the circular cylinder blade end shape. Fig. 3-1(a) shows an overview of a circular cylinder blade with a fairing installed at the end. Nicolas et al. (Nicolas et al., 2012) showed that the strength of the blade tip vortex was increased when the ratio of the end plate diameter to the cylinder diameter, d_e/d, was greater than 2. (Nicolas et al., 2012) showed that the strength of the blade tip vortex decreases and the drag coefficient decreases when d /d, the ratio of the end plate diameter to the cylinder diameter, is greater than 2. It is also shown that a uniform pressure distribution in the spanwise direction can be obtained when d_e/d=3. Therefore, the diameters of the disc-shaped end plates were prepared up to 60 mm, where d_e/d=3. The L-shaped end plate shape along the flat plate shown in Fig. 3-1(c) was numerically analyzed by Hemsuwan et al. and the increase in lift was reported when the circular cylinder blade length to diameter ratio l/d=4 or more (Hemsuwan et al., 2018b). The details of the L-shaped end plate are shown in Fig. 3-2. In addition, an L-shaped endplate is shown in Fig. 3-1(d), where the arc-shaped L-shaped endplate in Fig. 3-1(c) is modified to follow the tangent of the radius of rotation as well as the disc-shaped endplate Details of the L-shaped endplate are shown in Fig. 3-2. The dimensions of each part of these end plates are shown in Table 3-2.

(a) Faring on tip end **(b) Circular endplate on tip ends**

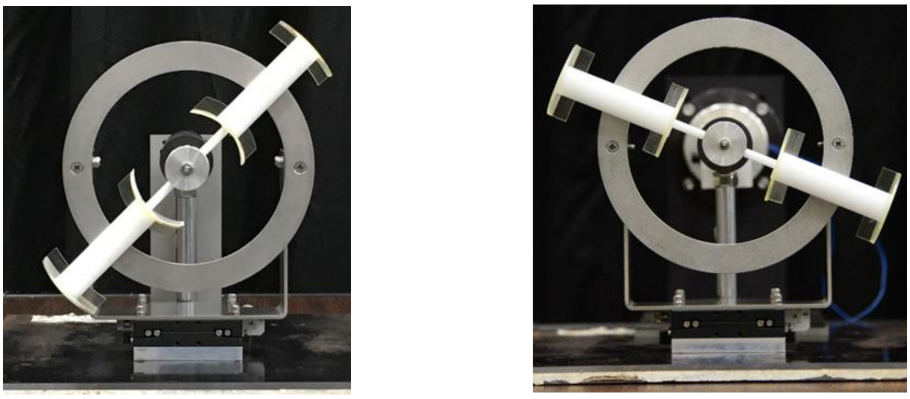

(c) Bended endplate with curvature on tip ends **(d) Bended endplate on tip ends**

Fig. 3-1 Photographs of a stepped wind turbine with attachments on the blade tips.

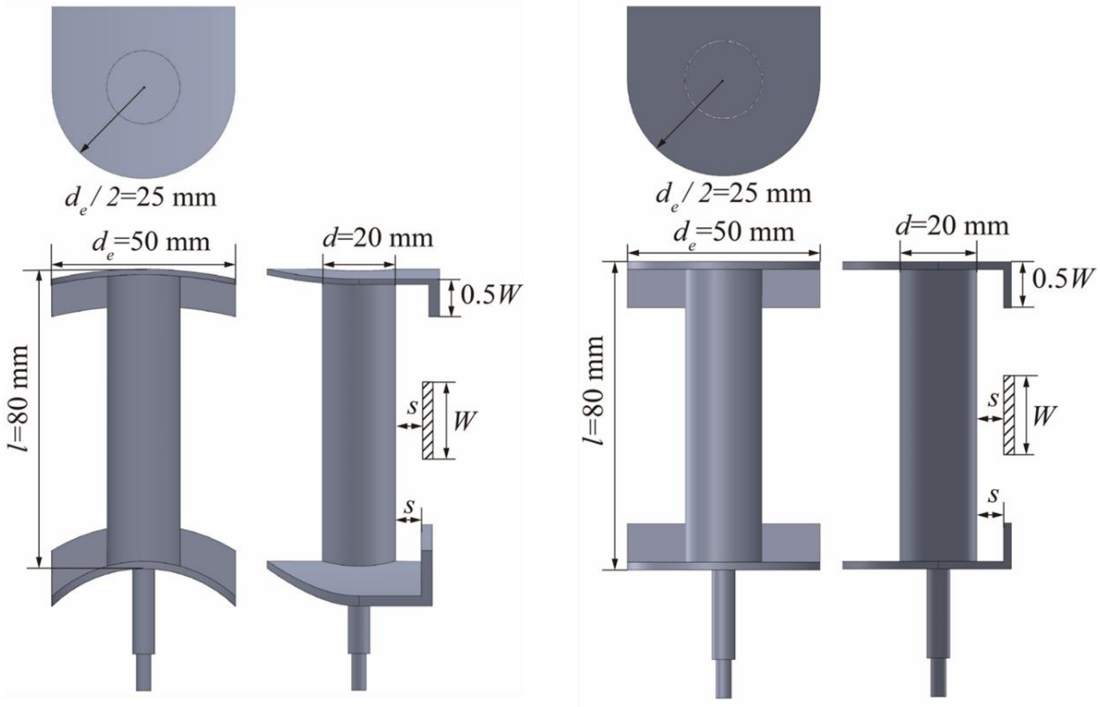

(a) L-type endplate with curvature **(b) L-type endplate**

Fig. 3-2 Detailed view of the L-type endplates attached to both ends of the circular cylinder blade.

Table 3-2 Parameter of endplate.

	Circular plate	Curved L-type plate	L-type plate
Tip end diameter d_e[mm].	20,30,40,50,60	50	50
Bending part length [mm]	-.	10 (0.5W)	10 (0.5W)

3.2.2 Measurement device

In order to evaluate the effect of the blade tip shape, the power characteristics against λ were obtained using the measurement method of the wind turbine driving force explained in Section 2.4.1. The torque of the circular cylinder blade wind turbine driven by the longitudinal vortex is similar to that of the pressure type wind turbine and increases as the load of the electromagnetic brake is increased and the rotation speed is decreased. In order to consider applications that take advantage of this feature of high torque at low rotation speed, it was considered important to improve the torque coefficient rather than the power coefficient in the performance evaluation of this wind turbine. Therefore, in this chapter, the torque coefficient is compared for each shape factor.

3.3 Experimental results and discussion

3.3.1 Improvement of power characteristics by fairing

Fig.3-3 plots the torque coefficients of a circular cylinder blade with and without a fairing in a uniform flow of *U*=15 m/s.C_q Fig.3-3(a)~(c) show the results for three circular cylinder blades with different diameters and the same shape of fairing. For each blade diameter, the gap ratio between the circular cylinder blade and the ring-shaped plate was set to *s/d*=0.35. Fig.3-3(a) shows that the gap ratio between the circular cylinder blade and the ring plate, *s/d*=0.35*,* decreases with increasing the diameter of the circular cylinder blade because the width of the ring plate, *W*=20 mm, is kept constant.C_q decreases linearly with the increase of λ. This behavior is very different from that of a general propeller-blade wind turbine with a horizontal axis and is similar to that of a Savonius-type wind turbine with a vertical axis and pressure (Nasef et al., 2013). And the torque is generated in the range of λ=0.02~0.4, which is even smaller than that of Savonius-type wind turbine, and the linear relationship continues to the point where λ=0. The torque is generated in the range of λ=0.02~0.4, which is even smaller than that of the general propeller-type wind turbine, and the linear relationship continues until λ=0. On the other hand, the maximum value of λ *is* about 0.36 when the electromagnetic brake voltage is zero and the load is only caused by mechanical losses such as friction of bearings. The maximum value of λ is about 0.36. The rotation speed is less than 1/10 of that of a general propeller-type wind turbine, and is also lower than that of a pressure-type wind turbine. According to the report by Sakamoto et al. (Sakamoto et al., 2021a), the lift generated by the Necklace vortex on a circular cylinder blade depends on the relative angle of attack created by the mainstream velocity *U* and the tip speed of the circular cylinder blade at the intersection of the ring-shaped plates. When the load by the electromagnetic brake is increased and the tip speed of the circular cylinder blade is decreased, the relative angle of attack decreases and the lift increases in proportion to this. Therefore, if *U* is constant, the lift force increases linearly when the voltage of the electromagnetic brake is increased and λ is decreased.C_q In Fig.3-3(a), the maximum torque is generated at the value of λ close to zero, that is, at the low rotation speed when the wind turbine is almost stopped. From Fig.3-3(b) and (c), the results for *d*=25 mm and 28 mm without the fairing show that the range of λ where the rotation can be maintained is narrower and the maximum value ofC_q and the maximum value of In addition, the relationship between λ and C_q also deviates slightly from a straight line. As *d* increases, Necklace vortices form in the axial direction of the circular cylinder blade at low rotational speeds. *l*=60 mm is *l*=60 mm was not long enough to form a stable Necklace vortex for these diameters, resulting in a smaller lift than expected.

Next, we examine the results for the case with the fairing installed: for *d*=25 mm and 28 mm as shown in Fig.3-3(b) and (c), the negative tendency of C_q for *d*=25 mm and 28 mm as shown in Fig.3-3(b) and (c), respectively, increases linearly even when λ approaches zero. The rotatable region also becomes almost stationary with low rotation and high torque. In other words, the installation of the fairing stabilizes the formation of the Necklace vortex. In particular, the fairing suppresses the flow generated from the blade tips, which affects the Necklace vortex formation in the region where λ is small, i.e. at low rotational speeds, and the Necklace vortex spreads close to the blade tips, improving lift. The installation of the fairing was shown to be effective in improving the start-up characteristics. On the other hand, at d=20 mm shown in Fig.3-3(a), the fairing reduced the C_q was reduced by the installation of the fairing. This is because the blade diameter is small compared to the fairing width

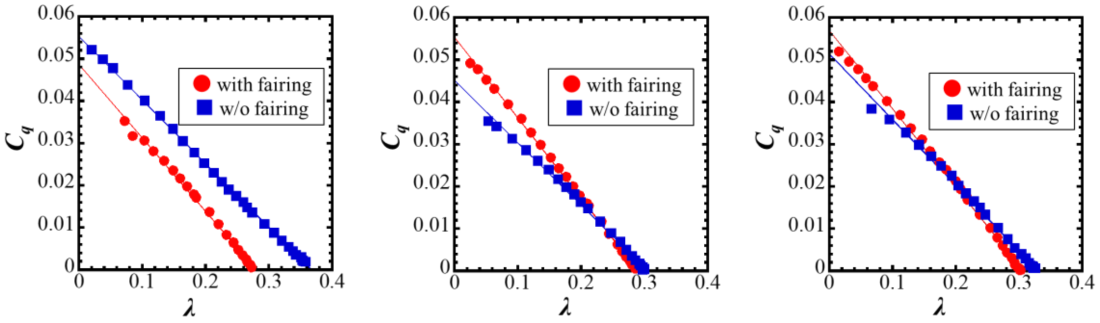

(a) d=20 mm **(b) d=25 mm** **(c) d=28 mm**

Fig. 3-3 Relation between tip speed ratio and torque coefficient with and without the fairing （*U*=15 m/s, （a） *W/d*=1, （b） *W/d*=0.8, （c） *W/d*=0.7, *N*=2）. The torque coefficient is higher without the fairing at *d*=20 mm, the reference value. On the other hand, at *d*=25 mm and 28 mm, where *W/d* becomes smaller, the installation of the fairing suppressed the torque reduction.

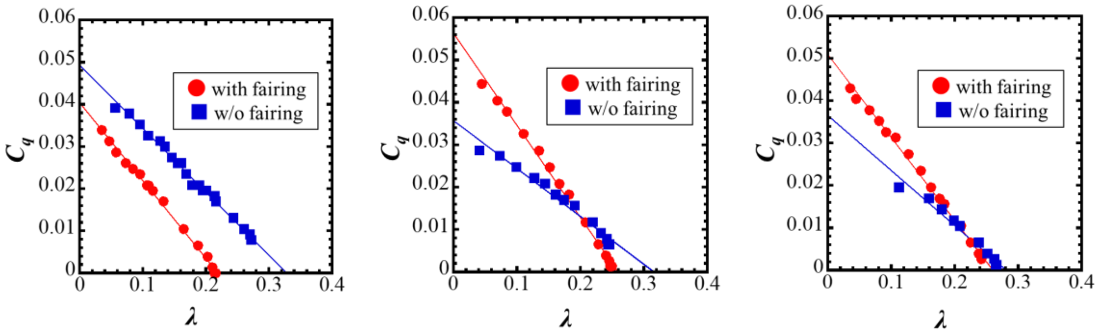

(a) d=20 mm **(b) d=25 mm** **(c) d=28 mm**

Fig. 3-4 Relation between tip speed ratio and torque coefficient with and without the fairing （*U*=6 m/s, （a） *W/d*=1, （b） *W/d*=0.8, （c） *W/d*=0.7, *N*=2）. The torque coefficient is higher without the fairing at *d*=20 mm, the reference value. On the other hand, at *d*=25 mm and 28 mm, where *W/d* becomes smaller, the installation of the fairing suppressed the torque reduction.

(length in the flow direction), and the flow from the leading edge of the fairing to the blade tip induces turbulence. The flow turbulence from the leading edge of the fairing to the blade edge may have been caused by the small diameter of the fairing in relation to the width of the circular cylinder blade.

Fig.3-4 shows the results for the case of U=6 m/s. Compared with the results for 15 m/s shown in Fig.3-3, the values of C_q values for all diameters are not linear, indicating that the formation of the necklace vortex is unstable. The range of possible rotation for λ *is* also narrow. By installing the fairing, the low rotation C_q is improved at d=25 mm and 28 mm. From these results, it is clear that the installation of a properly designed fairing can greatly improve the effect of blade tip flow caused by the insufficient length of the circular cylinder blade and improve the starting characteristics of the wind turbine.

3.2.2 Improvement of power characteristics by end plates

Fig.3-5 shows the effect of the outer end-plate diameter d on the torque coefficient C_q Fig.3-5 shows the effect of the diameter d_e of the outer end plate on the characteristics of the torque coefficient against the tip speed ratio λ under the conditions of U=6 and 15 m/s. The results are obtained by applying disc-shaped end plates with diameters ranging from 20 mm to 60 mm only on the outer end face of a circular cylinder blade with a diameter of 20 mm. The gap ratio s/d=0.35 and the width of the ring plate W=20 mm are kept constant. Fig.3-5(a) shows that for U=6 m/s C_q decreases linearly with λ regardless of the diameter d of the end plate. The results for d_e=40 mm are slightly lower than those for d_e=20 mm, where the end plate has the same diameter as the cylinder diameter. C_q is slightly lower for d =40 mm, but otherwise C_q is improved. In addition, if the tip speed ratio at the maximum

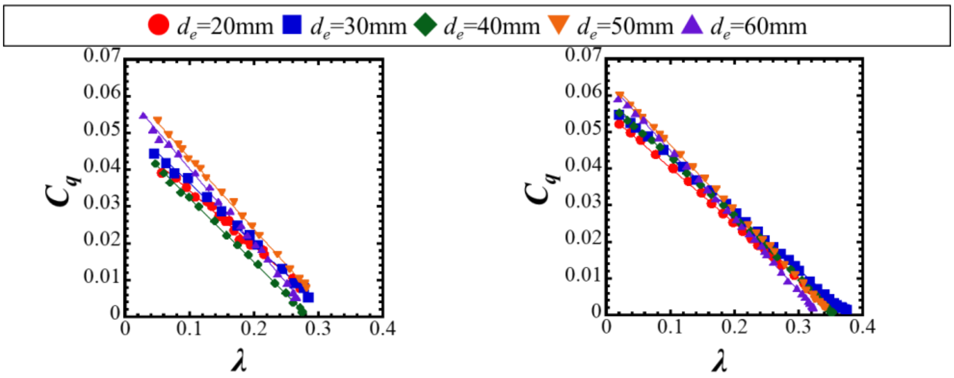

(a) U=6 m/s

(c) U=15 m/s

Fig. 3-5 Torque coefficient against tip speed ratio when the diameter is varied by installing endplates at the outer blade tip for each wind velocity. In addition, the torque coefficient increased at low tip speed ratios. In addition, the torque coefficient increased at low tip speed ratios. It is possible to increase the maximum torque coefficient and reduce the rotation It is possible to increase the maximum torque coefficient and reduce the rotation speed with the endplates.

torque, i.e., at the limit where rotation can be maintained, is defined as $\lambda_{\mathrm{min},}$ installing an end plate thicker than the cylinder diameter reduces λ_{min}, and a higher C_q By installing an end plate thicker than the diameter of the cylinder, we can reduce λ and obtain a higher When the flow velocity is set to U=15 m/s, as shown in Fig.3-5(b), there is no significant change depending on the value of $d_{e.}$ However, at d_e=50 mm and 60 mm C_q-λ at $d = 50$ mm and 60 mm, the negative orientation of the λ line becomes larger and λ_{min} becomes smaller. C_qThe value of (C_{qmax}) is about 11 % higher than that of d_e =20 mm.

It was found that the installation of a disc-shaped end plate extended the stable rotation range to the lower rotation side, which enabled high torque to be generated. Therefore, the relationship between the diameter d_e of the end plate and the maximum torque coefficient C_q The relationship between the diameter d of the end plate and the maximum value of the torque coefficient is investigated in more detail. Fig.3-6 summarizes the effect of the end-plate diameter de on the maximum value of C_{qmax} in the λ-C_q characteristics obtained for each wind speed U. Fig.3-6(a) shows the results for the case where the end plates are installed only on the outer end face. However, the larger the d_e, the clearer the improvement in C_{qmax}, but the effect becomes almost the same at the size of 50 mm to 60 mm. On the other hand, in the case of the end plates on both sides as shown in Fig.3-6(b), C_{qmax} decreases with the increase of de when U is 15 m/s and 20 m/s. From the comparison with the results in Fig.3-6(a), it can be seen that the inner end plates decrease C_{qmax} and the decrease is larger with the increase of d_e. The inner endplate decreases C_{qmax}, and the larger d_e is, the larger the decrease becomes. The end plates on the outer end face are shaped to introduce air to the circular cylinder blade side in the direction of rotation, while the inner end plates are shaped to exclude air that would have been introduced to the circular cylinder blade as the diameter increases. However, in the circular

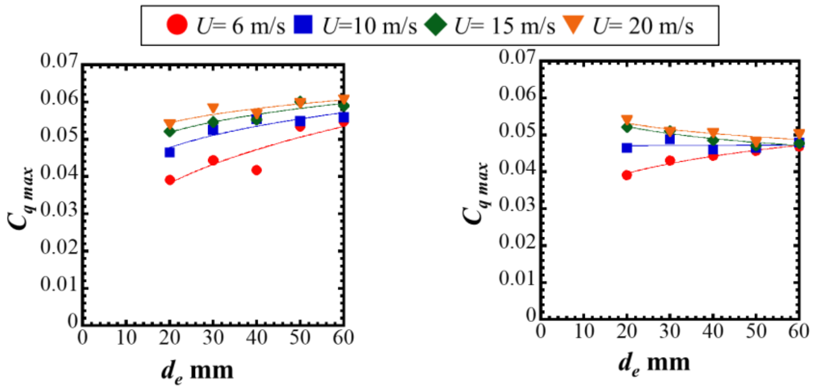

(a) Outer end **(b) Both ends**

Fig. 3-6 Maximum torque coefficient against blade tip diameter for each wind speed. When endplates were installed at the outer blade tip, the maximum When endplates were installed at the outer blade tip, the maximum torque coefficient tended to increase with the increase in blade tip diameter at all wind speeds. When endplates were installed at both blade tips, the increase in blade tip diameter became a source of resistance to the increase in wind speed.

cylinder blade wind turbine, the increase in the d_e of the inner end plate interfered with the longitudinal vortex formation region and affected the stable formation of the longitudinal vortex.

Fig.3-7 shows the maximum torque coefficient per blade obtained by dividing the maximum torque coefficient by the number of blades for the wind turbine with N=2, 4 and 8 blades. The maximum torque coefficient per blade was obtained by dividing the maximum torque coefficient obtained for wind turbines with four or eight blades by the number of blades. In Fig. 3-7(a), when the mainstream speed is set to U=6 m/s, C_{qmax}/N tends to increase with respect to de for all blade numbers. In Fig.3-7(b) and (c), the effect of de becomes smaller because the C_{qmax}/N improves even without the end plate (de =20 mm) due to the increase of the flow velocity. The effect of de becomes smaller. However, in the results for U=20 m/s shown in Fig. 3-7(d), C_{qmax}/N decreases with an increase in de at N=8. This may be due to the fact that the distance between the blades is narrowed by increasing the number of blades and the distance between the blades at the tip of the blade is further narrowed by increasing the end-plate diameter, and the flow is affected by the adjacent blades. These results indicate that the end-plate diameter cannot be increased too much when the number of blades is increased.

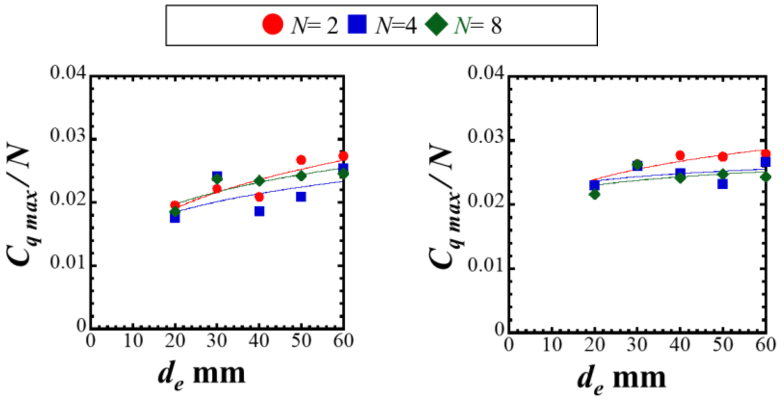

(a) U= 6 m/s **(b) U= 10 m/s**

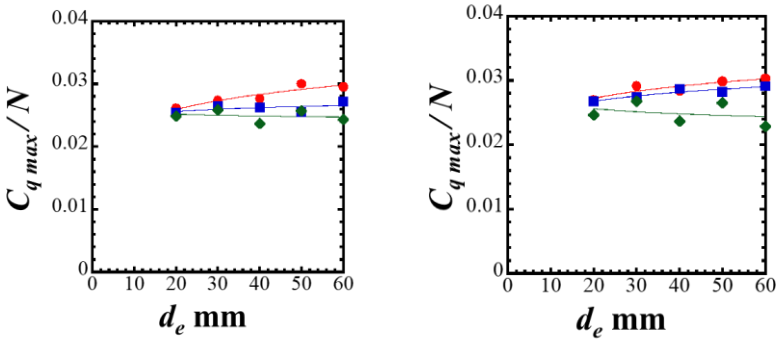

(c) U= 15 m/s **(d) U= 20 m/s**

Fig. 3-7 Relationship between blade tip diameter and maximum torque coefficient for each number of blades. As the number of blades increases, the torque As the number of blades increases, the torque increase due to the end diameter is suppressed. This tendency becomes stronger with an increase in wind speed. Increasing the blade tip diameter results in a larger decrease in torque.

3.2.3 Improvement of power characteristics by end plate shape

Hemsuwan et al. conducted a numerical analysis of a circular cylinder translating along a straight flat plate, and showed that a part of the end plate at the end of the cylinder was bent so that it was parallel to the back-flowing plate to form an L-shape, which caused new vortices to flow out from the bent part and increased the driving force. In particular, when the diameter of the cylinder was d=20 mm, the lift-drag ratio was improved by 5.5 % compared to that of the cylinder alone when the blade length was l=80 mm (l/d=4) and the blade tip diameter was d_e=50 mm (d_e/d=2.5) (Hemsuwan et al., 2018b). In this section, the L-shaped endplate is fabricated and compared with the disc-shaped endplate shown in the previous section. l/d must be greater than 4 for the L-shaped endplate to be effective according to Hemsuwan et al.'s report, so experiments are conducted on a circular cylinder blade with l = 80 mm. Since the L-shaped end plates of Hemsuwan et al. were designed for circular cylinder blades moving straight in one direction, an arc-shaped L-shaped end plate was also fabricated and compared with the simple L-shaped end plate considering the rotational motion of circular cylinder blades. The results were compared.

First, the change in the effect of the end-plate due to the increase in blade length is compared with a disc-shaped end-plate; for circular cylinder blades of l = 80 mm and 60 mm, with and without an end-plate of d_e= 50 mm, λ-C_q with and without d =50 mm end plates. The results are shown in Fig. 3-8. The main flow velocity was kept constant at U=10 m/s. In Fig. 3-8(a), the value of $C_q$decreased significantly by increasing the blade length l to 80 mm compared with the results without the end plate.C_q value was greatly reduced by increasing the blade length l to 80 mm. This result is similar to that reported by Hemsuwan et al. (Hemsuwan et al., 2021), who found that the highest torque was

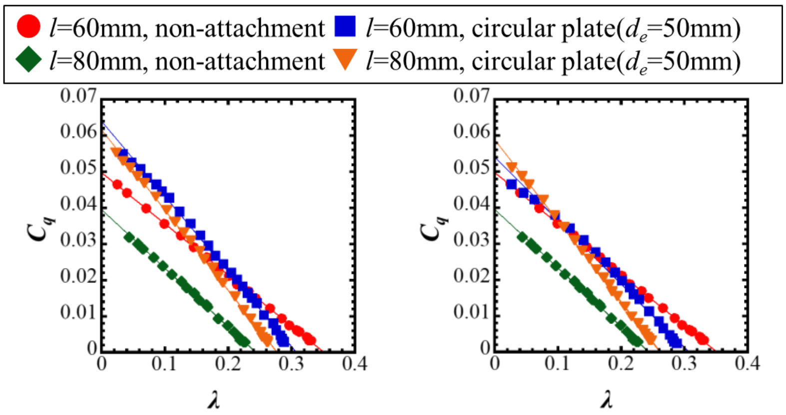

(a) Outer end **(b) Both ends**

Fig. 3-8 Torque coefficient against tip speed ratio for each blade tip shape （U=10 m/s, N=2, l=60, 80 mm, d_e=50 mm）. The performance at l=80 mm is reduced because the drag at the blade tip increases with the increase in blade length. The performance is improved by installing an endplate at the outer tip end. Installing the endplate on the inside does not affect the stabilization of the longitudinal vortex but increases the drag.

generated by a circular cylinder blade with d = 20 mm for a ring width of W = 20 mm when l/d = 3. On the other hand, the difference between l=60 mm and 80 mm becomes much smaller when the end plates are installed only on the outer side of this blade, indicating that the effect of the flow field at the blade tip is the cause of the performance degradation for blade lengths of l/d=3 or more. It is contrary to the general feeling that the performance degradation due to the blade tip effect is more pronounced for longer blade lengths, but the negative pressure at the trailing edge of a cylinder tends to generate flow from the blade tip in the span direction. However, the negative pressure at the trailing edge of a circular cylinder blade tends to generate flow in the spanwise direction from the blade tip. In the case of l=80 mm, on the other hand, C_q decreases and the performance deteriorates. On the other hand, the performance of the l=80 mm blade is generally well improved, indicating that the adverse effect of the inner end plates is not so great.

Fig.3-9 shows the λ-C_q characteristics without end plates, with disc, L-shaped and arcuate L-shaped end plates attached only at the outer end, at the inner end and at both ends. The number of blades is N=2. The number of blades is N=2, and the main flow velocity is kept constant at U=10 m/s. Fig.3-9(a) shows that the end plates installed at the outer blade tips increase the C_q of both shapes compared to that of the circular cylinder blades, showing a significant improvement. Looking at the behavior at the low RPM side, the disk shape rotates more stably at low RPM, and the L-shaped end plate and the arc-shaped L-shaped end plate deteriorate the low RPM characteristics in that order. In the range of λ = 0.1 or less, rotation stops for the bent plate and the bent plate with curvature, and the rate of decrease of C_q with respect to λ (negative orientation) decreases in the order of the L-shaped end plate, the disk type, and the arc-shaped L-shaped end plate. Fig. 3-9(b) shows the results with end plates installed only on the inner blade tip. The disk-shaped end plate plots on the same line as the result without the end plate, but the range of rotatable λ

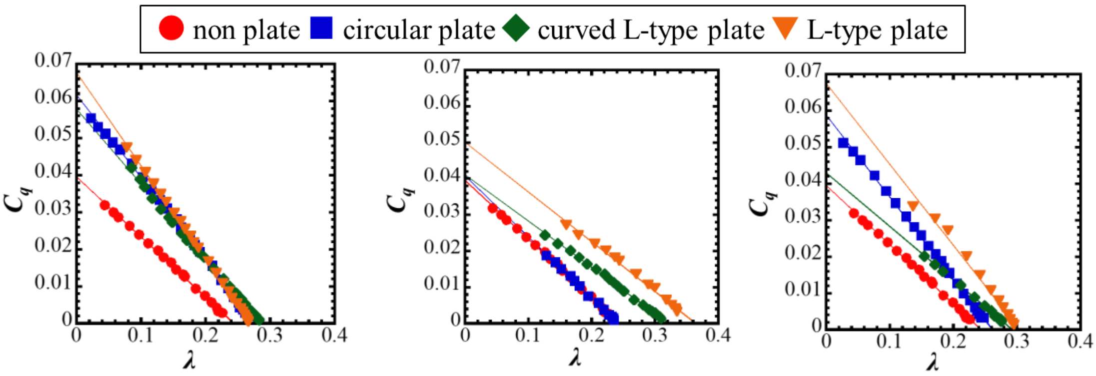

(a) Outer end **(b) Inner end** **(c) Both ends**

Fig. 3-9 Torque coefficient against tip speed ratio for each blade tip shape (U=10 m/s, N=2, l=80 mm, d_e =50 mm). The torque characteristics are not improved by shaping the edge along the direction of rotation. By changing the end shape, the characteristics of low speed and high torque can be changed to high speed and low torque.

becomes much narrower, resulting in a smaller C_{qmax}. On the other hand, the installation of L-shaped and arcuate L-shaped end plates results in high rotation. The effect is higher for the L-shaped end plate with a bent flat plate than for the arc-shaped L-shaped end plate with reduced rotational resistance, and it rotates up to the high rotation range. As shown in Fig.3-9(c), the effect of the inner end plates on the performance of the disk type is not so great, while the effect of the inner end plates on the performance of the L-shaped and arcuate L-shaped blades is not so great. On the other hand, in the case of the L-shaped and arcuate L-shaped end plates, the characteristics of the inner end plate were more apparent. In the case of the arcuate L-shape, the performance was worse when the end plates were installed on both sides than when they were installed only on the inside. This indicates that the torque characteristics cannot be expressed by simple addition of the effects of each end plate when the end plates are installed on the outer and inner end faces.

In the region where λ is small, the rotational speed is small and the tip speed of the circular cylinder blade is small. When the circular cylinder blade is stationary, Necklace vortices are periodically formed in front and behind the gap between the wake plate and the cylinder. As the cylinder rotates in one direction and obtains a tip speed, the flow has a relative angle of attack to the cylinder. The relative angle of attack causes the Necklace vortex to form stationarily behind the cylinder in the direction of motion. This is the principle of the longitudinal vortex wind turbine, but when the rotation speed is low, the rotation stops because the tip speed is small and it becomes difficult to stabilize the Necklace vortex. Therefore, the performance improvement by controlling the blade tip flow of the circular cylinder blade wind turbine driven by the longitudinal vortex has the effect of increasing the rotational speed by suppressing the flow resistance, which can be applied to the ordinary wind turbine, and also the effect of promoting the stable formation of the longitudinal vortex at low rotational speeds, which enables the wind turbine to rotate at lower rotational speeds. Since the torque increases linearly as the rotation speed decreases, the fact that the vortex can rotate stably in the low rotation speed range means that it can generate enough torque to start up even at high loads, and this feature of low rotation speed and high torque is more strongly demonstrated, which greatly contributes to the improvement of the practicality of the wind turbine. On the other hand, since the wind turbine is driven by Necklace vortices, if the flow fields of the outer and inner blade tips have an adverse effect on the formation of Necklace vortices, the adverse effect will dominate even if one of them has an effect on the performance, and the characteristics of the wind turbine will deteriorate. The flow field at the blade tip has a significant effect on the overall flow of the blade, which is very different from that of an ordinary wind turbine.

3 .3 Chapter 3 Conclusion

The torque characteristics of a circular cylinder blade wind turbine driven by a longitudinal vortex are greatly affected by the flow field at the blade tip. Experiments have shown that the torque coefficient can be increased by attaching an end plate to the blade tip and that the rotational force can be obtained stably even at very low speeds. The effects of the end plates on the blade tips were newly clarified as follows.

In the case of circular cylinder blade wind turbines, the installation of fairings or end plates enables the turbines to rotate stably at low speeds even under high loads, and also reduces drag at high speeds and increases the maximum speed. However, the shape and size of the fairing must be suitable for the diameter of the circular cylinder blade, and if the fairing is wider than the diameter of the circular cylinder blade, the torque coefficient will be reduced. In the case of the fairing, if the width is wider than the diameter of the circular cylinder blade, the torque coefficient will be reduced. In the case of the disk end plates, the torque coefficient can be improved by up to 20% by attaching a disk end plate with a diameter 2.5 to 3 times the diameter of the circular cylinder blade to the outer blade tip only. The L-shaped end plates predicted by Hemsuwan et al. have the effect of shifting the characteristics to the high rotation side and increase the torque coefficient at the same tip speed ratio. However, the lower limit of stable rotation becomes higher, and as a result, the value of the maximum torque coefficient obtained at high load becomes lower.

When endplates are attached to the outer and inner blade tips of a circular cylinder airfoil, the effect is not the sum of the effect of attaching the endplate to the outer end only and the effect of attaching the endplate to the inner end only. When the inner endplate adversely affects the stable formation of Necklace vortices, the effect of the inner endplate dominates the torque characteristics and degrades performance regardless of the performance improvement of the outer endplate. In particular, it is difficult to obtain high torque due to the inhibition of rotation at low speeds under high loads.

Chapter 3 References

Hemsuwan, W., Sakamoto, K. and Takahashi, T., Lift Force Generation of a Moving Circular Cylinder with a Strip-Plate Set Downstream in Cruciform Arrangement: Flow Field Improving Using Tip Ends, International Journal of Aeronautical and Space Sciences, Vol. 19, Issue 3 (2018), pp. 606-617

Hemsuwan, W., Sakamoto, K. and Takahashi, T., Steady lift-force generation on a circular cylinder utilising a longitudinal vortex: Influence of geometrical parameters, Journal of Wind Engineering & Industrial Aerodynamics, 212(2021), 104612

Nasef, M.H., El-Askary, W.A., AbdEL-hamid, A.A. and Gad, H.E., Evaluation of Savonius rotor performance: static and dynamic studies, J. Wind Eng. Ind. Aerodyn. 123 (2013),pp.1-11.

Nicolas T., Christian B. and Nikolaus A. A., Numerical Analysis of a Rotating Cylinder with Spanwise Disks, AIAA Journal Vol. 50, No. 2 (2012), pp. 271-283

Nishizawa, Y., Suzuki, M., Taniguchi, H. and Ushiyama, I., An experimental study on the low tip speed ratio type horizontal-axis small wind turbines with winglets, Journal of JWEA, Vol.33, No.2 (2009a), pp.98-103 (in Japanese)

Nishizawa, Y., Suzuki, M., Taniguchi, H. and Ushiyama, I., An experimental study of vertical-axis wind turbines, Transactions of the Japan Society of Mechanical Engineers, Series B, Vol.75, No.751 (2009b), pp.164-166

Ohya, Y., New wind turbine with wind-lens technology, Wind Engineers, JAWE, Vol.36, No.1 (No.126) (2011), pp.19-22

Sakamoto, K., Udaka, K., Hemsuwan, W. and Takahashi T., Development of circular cylinder blade wind turbine driven by longitudinal vortex, Transactions of the JSME, Vol. 87, No. 894 (2021a) DOI:10.1299/transjsme.20-00365

Sakamoto, K., Hemsuwan, W. and Takahashi T., Drag force of circular cylinder blade wind turbines driven by steady lift force of longitudinal vortex, Transactions of the JSME, Vol. 87, No. 894 (2021b) DOI: 10.1299/transjsme.20-00375

Wenjun G., Daniel N., Zhenxia L. and Yaguo L., Numerical investigation off low around one finite circular cylinder with two free ends, Ocean Engineering, Vol. 156 (2018) pp. 373-380

4. Influence of Fin-Shaped Flat Plate on Power Characteristics of Single Circular cylinder Blade Wind Turbine

4.1 Chapter 4 Introduction

In general, a large wind power generation system has a structure with a rotating part and a nacelle on the top of the tower which supports the wind turbine, and it is designed considering the load acting on the tower during driving. Yamamoto et al. (Yamamoto et al., 2009) proposed a formula for calculating the maximum horizontal load acting on a rotating wind turbine for a large wind power generation system. Using the proposed formula, a comparison with the measured values is made. Yoshida (Yoshida, 2010) modeled the fatigue load acting on a general variable speed and pitch controlled wind turbine and proposed a controller to reduce the fatigue load.

A circular cylinder blade wind turbine driven by a longitudinal vortex requires a flat plate that crosses behind the columnar object used as a blade because of its operating principle. When considering the practical use of wind turbines, it is necessary to expand the wind turbine system not only for large wind turbines such as those used in wind power plants but also for small and medium-sized wind turbines that can be installed in residential areas. As the flat part of the wind turbine becomes larger, the load on the wind turbine is expected to increase significantly compared to that of a normal wind turbine. Therefore, it is necessary to maintain the fluid force by the longitudinal vortex and to minimize the flat plate.

In this chapter, the ring-shaped plate was changed to a fin-shaped plate to minimize the flat part. The fin-shaped plate is designed to change the width at the front (upper part) and at the back (lower part) of the rotation direction. First, the outflow position of the longitudinal vortex was confirmed for the fin with a fixed width as well as the conventional ring-shaped plate by visualization, and the necessary length of the plate in the rear of the rotating direction was examined. Similarly, the outflow position of the longitudinal vortex was confirmed by visualization when the width and angle of the upper part were changed, and the effect of the increase in the flow rate to the intersection on the outflow position of the longitudinal vortex was examined. The power characteristics of these fin-shaped plates were measured experimentally, and the effect of the fin-shaped plates on the increase of power was examined.

4.2 Procedures of visualization and power measurement experiments

4.2.1 Visualization Experiment

The wind tunnel experimental apparatus shown in Section 2.1 was used for the visualization experiment. The flow velocity was kept constant at U=10 m/s. The cylinder used was a single cylinder with d=20 mm and the length was L=220 mm. The fin-shaped plate was attached to the cylinder via an end plate. The shape of the end plate was the same as that of the top plate of the L-shaped end plate described in Chapter 3. In order to visualize the flow on the plate surface by the oil film method, toothpaste dissolved in water was applied to the fin-shaped plate. A fin-shaped plate was attached to one side of a single cylinder, fixed to the outlet of the test section, and held until the toothpaste-coated surface dried, as shown in Fig.2-7. As shown in Fig.2-7, the connection with the end plate was used as the reference position, and the distance was measured at the outflow position of the longitudinal vortex.

4.2.2 Power measurement

The power measurement was carried out using the method shown in Section 2.4.1. As in the visualization experiment, the flow velocity was kept constant at U=10 m/s. Two fin-shaped plates were attached to a single cylinder with d=20 mm and L=220 mm. The power and torque coefficients were calculated by measuring the rotation speed and torque at different angles about the upper part of the fin-shaped plate.

4.3 Observation of the position of longitudinal vortex generation on a fin-shaped plate by visualization experiment

4.3.1 Effect of the width of the top surface of the flat plate

In this section, we show the visualization results when the width of the upper surface of the plate is changed and compare the distance between the top of the cylinder and the outflow position of the longitudinal vortex when viewed from the mainstream. The widths of the fin-like plates were set to w=30 mm at the bottom and 30, 60, and 90 mm at the top. Fig.4-1 shows the results of longitudinal

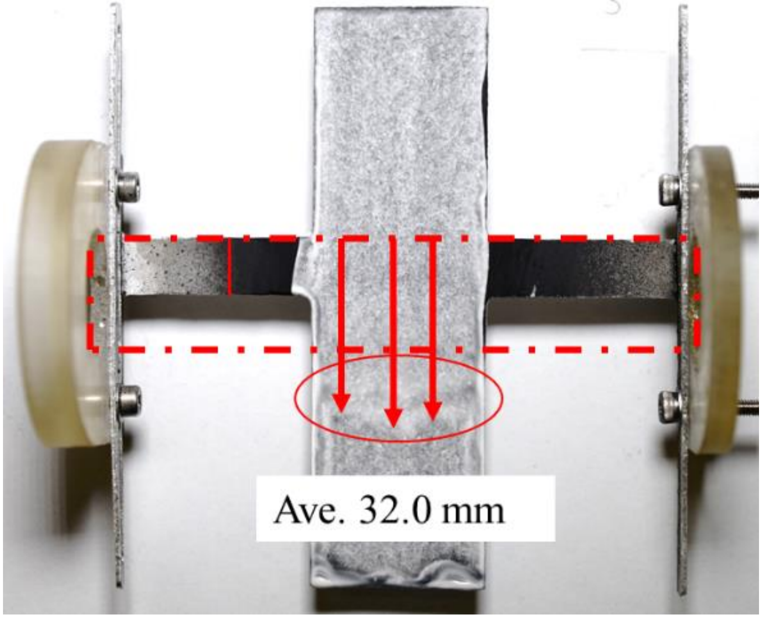

(a) *w*=30 mm

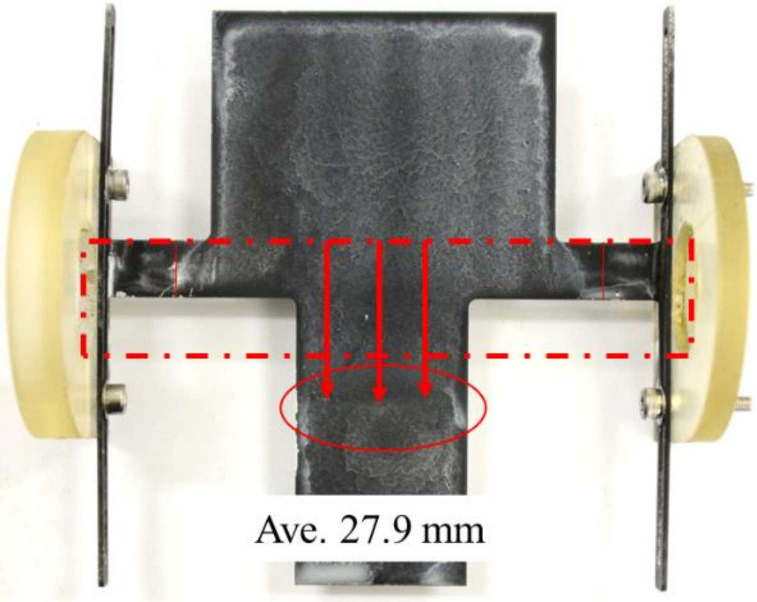

(b) *w*=60 mm

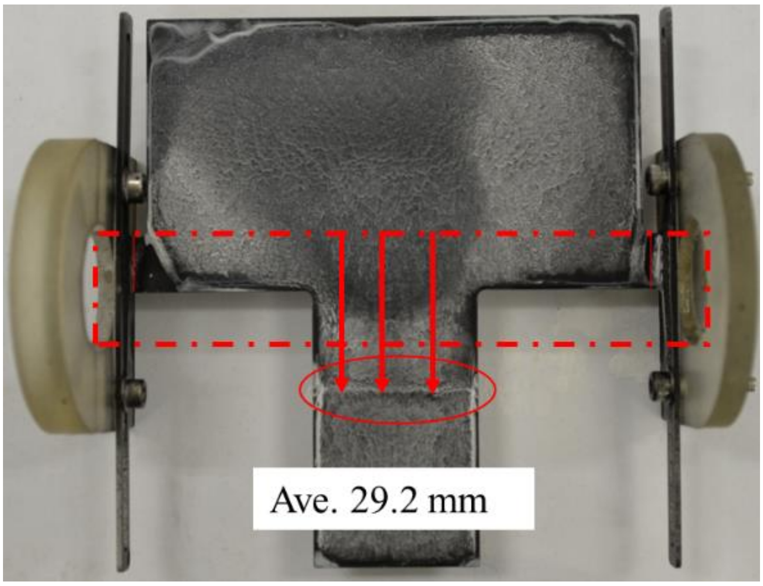

(c) *w*=90 mm

Fig. 4-1 Distance from the top of the cylinder to the outflow position of the longitudinal vortex for each upper width (*U*=10 m/s, *d*=20mm)

vortex shedding position for each width of the upper plate. 3 distances were measured from the top of the cylinder to the lower limit of the white area, and the average value was used as the longitudinal vortex shedding distance. From Fig.4-1(a), it can be seen that the longitudinal vortex outflow distance is 32 mm from the top of the cylinder, that is, 22 mm from the center of the cylinder, and that the vortex outflow occurs at a diameter ratio of 1.*1D* from the center. (b) and (c) show that the outflow distance of the longitudinal vortex is 0.9 *D* and 0.96 *D* from the center of the cylinder, respectively, indicating that the outflow occurs within 1.1 *D* of the cylinder blade diameter ratio, independent of the width of the upper plate.

4.3.2 Effect of the angle of the flat top surface

In this section, the change of the longitudinal vortex outflow distance when the angle of the top surface of the flat plate is changed is compared with the visualization results. The width of the upper surface of the flat plate was kept constant at w=30 mm. The main flow velocity was set to U=10 m/s and the cylinder was fixed horizontally at the outlet of the test section. The results for the angle θ_{plate}=0 deg are the same as those shown in Fig.4-1(a), and those for θ_{plate}=20 and 40 deg are also prepared.

Fig.4-2 shows the visualization results of the outflow distance of the longitudinal vortex when the angle of the upper surface of the plate was changed. 11% of the outflow position of the longitudinal vortex moved to the cylinder side in the result of θ_{plate}=20 deg shown in Fig.4-2(a) compared with θ_{plate}=0 deg in Fig.4-1(a). In the case of θ_{plate}=40 deg in Fig.4-2(b), the outflow position of the longitudinal vortex shifted to the cylinder side by 20% compared with the result of 0 deg. From these results, it was found that inducing the inflow at the intersection of the cylinder and the plate by adding an angle to the upper surface of the plate did not inhibit the formation of the longitudinal vortex. In addition, the outflow of the longitudinal vortex was not separated from the cylinder by the increase of

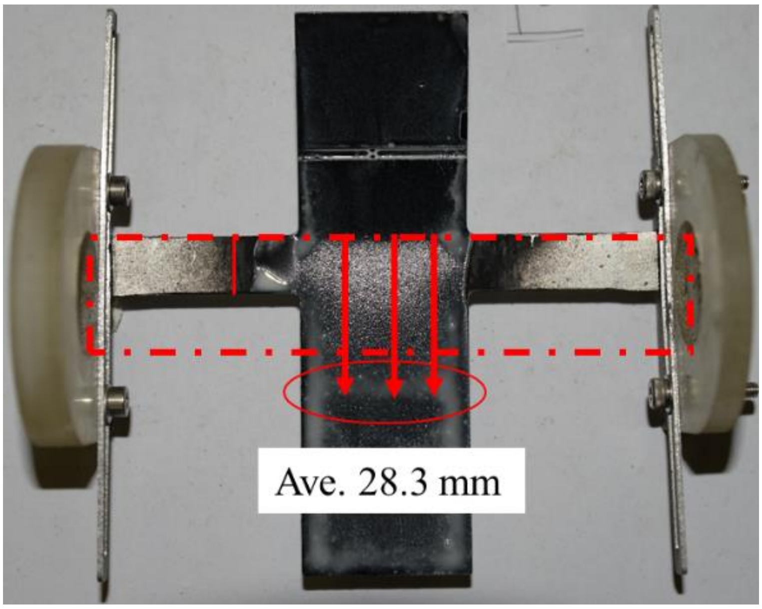

(a) θ_{plate}=20 deg

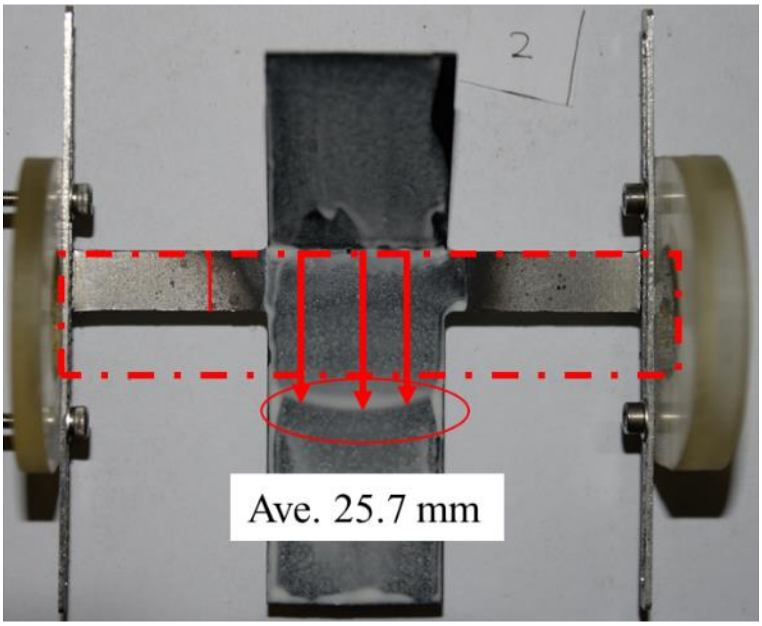

(b) θ_{plate}=40 deg

Fig.4-2 Distance from the top of the cylinder to the outflow position of the logitudinal vortex for each upper angle (*U*=10 m/s, *d*=20 mm)

the vertical flow component, and the outflow position could be brought closer to the cylinder. The outflow position of the longitudinal vortex was moved closer to the cylinder. It is considered that this not only increases the dynamic pressure on the angled top surface of the plate but also increases the effect of the suction force by the longitudinal vortex.

4.4 Power characteristics

4.4.1 Effect of the angle of the flat top surface

Fig.4-3(a) shows the λ-C_q plot of the circular cylinder blade wind turbine with the ring-shaped plate and (b) shows the λ-C plot of the circular cylinder blade wind turbine with the fin-shaped plate.

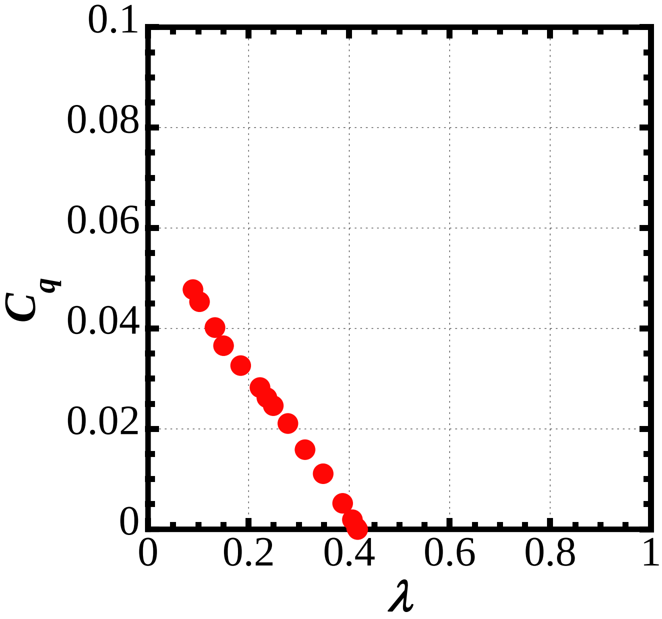

(a) With ring type flat plate

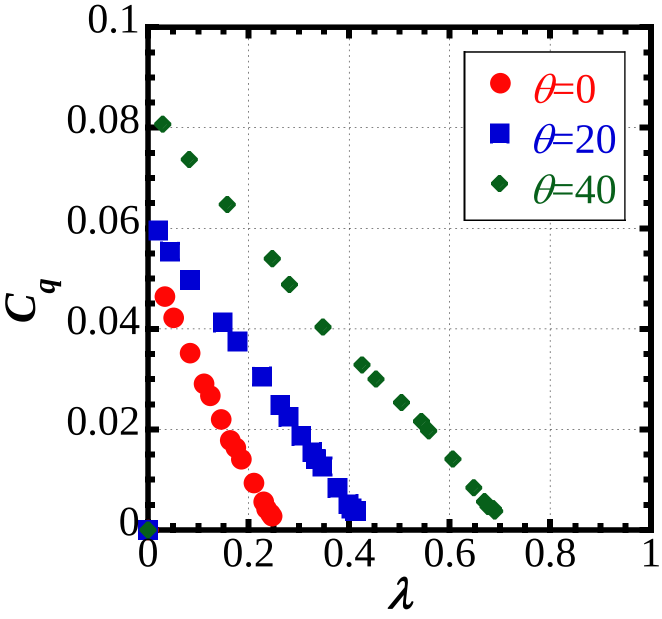

(b) With fin type plate

Fig. 4-3 Comparison of λ-C_q between the case with a ring type flat plate and the case with a fin type plate (U=10 m/s, d=20 mm).

Fig.4-3(a) shows the λ-C plot of a circular cylinder blade wind turbine with a ring-shaped plate, and (b) shows the λ-C_q plot of a circular cylinder blade wind turbine with a fin-shaped plate. $\theta_{\mathrm{plateplate}}$= 0 deg for the fin-shaped plate shows that the maximum torque coefficient $C_{qmaxqmax}$is almost the same as that of the ring-shaped plate, although the range of the driven speed ratio becomes narrower. The maximum torque coefficient C was almost the same as that of the ring-shaped plate. The maximum value of the drive speed ratio also increased with the increase of $\theta._{\text{plate}}$ This means that the rotation speed increases. Therefore, the power coefficient, which is a function of the torque and the rotation speed, is plotted $_{pin}$ Fig. 4-4, and the maximum power coefficient $C_{pmax}$is equal to that of the ring-shaped plate at $\theta_{\text{plateplate}}$= 20 deg. However, the maximum power coefficient C is equal to that of the ring-shaped plate at θ =20 deg, and it is about 2.3 times higher at θ =40 deg.

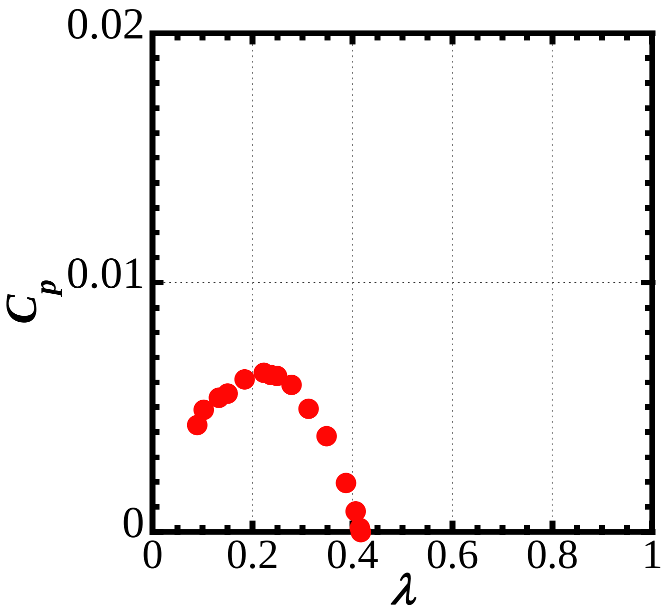

(a) With ring type flat plate

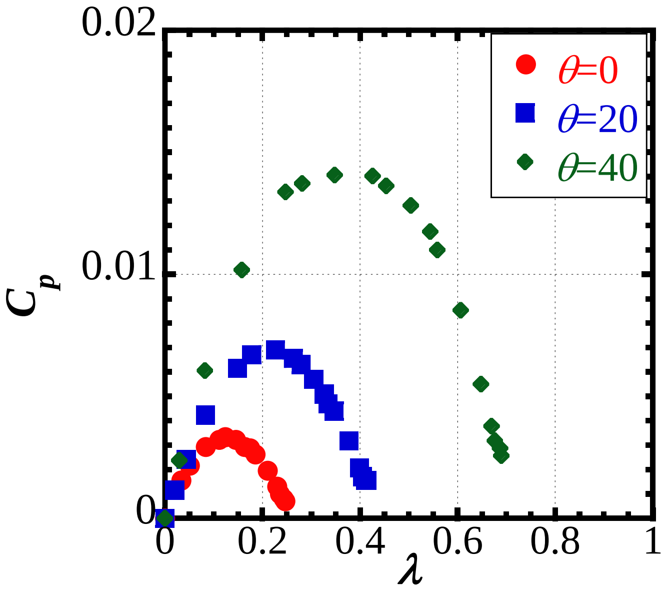

(b) With fin type plate

Fig. 4-4 Comparison of λ-$C_p$between the case with a ring type flat plate and the case with a fin type plate (U=10 m/s, d=20 mm).

4.5 Chapter 4 Conclusion

In this section, the minimum configuration of the flat plate was examined and a fin-shaped flat plate was proposed in order to reduce the drag force on the flat plate when the circular cylinder blade wind turbine driven by the longitudinal vortex becomes larger and has more blades. The visualization results showed that the outflow position of the longitudinal vortex did not change depending on the width of the upper surface of the fin-shaped plate, and that the outflow position of the longitudinal vortex approached the cylinder as the angle of the upper surface increased. It was also found that the outflow position of the longitudinal vortex was generally located within 1.1D from the top of the cylinder. This suggests that the use of the fin-shaped plate with an angled top can increase the dynamic pressure from the main flow and the suction force of the longitudinal vortex. From the measurement results of the power characteristics, it was found that the fin-shaped plate with the same width as the ring-shaped plate could be used to reduce the size of the plate without losing the torque. This makes it possible to reduce the wind load on the wind turbine support column when it is enlarged. In addition, by angling the upper surface of the fin-shaped plate, the conventional circular cylinder blade wind turbine with low rotation and high torque can be made to rotate at high speed.

Chapter 4 References

Yamamoto, M., Kondo, K. and Ohkuma, T., Formula for estimating the maximum along-wind load on a tower of wind turbine in the operational condition, J. Structr. . Eng., AIJ (2009) Vol.74 No.642

Yoshida, S., Variable Speed-Variable Pitch Control Parameters for Aero-elastic Simulations of Wind Turbine Support Structures (in Japanese), Wind Energy, Vol.33, No.4 (2010), pp.104-111.

5. Effects of Geometry and Load Fluctuation on Power Fluctuation Characteristics of a Stepped Circular cylinder Blade Wind Turbine

5.1 Power fluctuation characteristics during steady-state rotation

The strong suction flow in the longitudinal vortex region formed between the circular cylinder blade and the ring-shaped flat plate forms a steady lift force in the wind turbine subjected to this paper, but the numerical analysis showed that the vortex region showed slight periodic fluctuations in size. The results showed that the lift force due to the vortex generated fluctuations with a frequency component of about 80Hz when the tip speed ratio was in the range of $0.125 < \lambda < 0.2$ (Hemsuwan et al., 2018). This is attributed to the reattachment of longitudinal vortices at the surface of the cylinder due to the increase in the tip speed ratio, i.e., the increase in the angular velocity.

In this section, the occurrence of the temporal change of the torque in the new wind turbine powered by the longitudinal vortex predicted by the numerical analysis is confirmed experimentally. Furthermore, the relationship between the operating conditions of the wind turbine and its vibration is clarified experimentally.

5.1.1 Measurement procedure for power fluctuation characteristics

The experiments were carried out using the wind tunnel apparatus shown in Section 2.1. The main flow velocity was set to U=10 and 15 m/s. A stepped circular cylinder blade wind turbine shown in Section 2.2.2 was used for the wind turbine system. The blade is a cylinder with d=20 mm and l=60 mm. The driving conditions of the wind turbine were set to be $0.05 < \lambda < 0.2$ in the range of the tip speed ratio by adjusting the load with an electromagnetic brake. The torque and rotational speed during steady-state rotation were obtained by a torque meter attached to the rotating shaft of the wind turbine.

5.1.2 Frequency analysis

A part of the time-series data of the torque obtained when the tip speed ratio $\lambda = 0.15$ is set by the electromagnetic brake is shown in Fig.5-1. The temporal variation of the torque includes the component due to mechanical causes such as the eccentricity of the rotating shaft, etc. The temporal variation of the torque is measured and frequency analysis is performed under the same conditions as the numerical analysis results of Hemuswan et al. The frequency distributions obtained for various speed ratios λ by adjusting the load with electromagnetic brakes are shown in Fig.5-2. as shown in Fig.5-2, there are peaks of frequency increases with increasing speed ratio and peaks of frequency independent of speed ratio. The frequency peak with the highest spectrum at any tip speed ratio corresponds to the rotational speed, which is caused by mechanical factors such as the eccentricity of the wind turbine. As shown in Fig.5-3, the peak frequencies of the 2, 3, and 4 peaks of each tip speed ratio are defined as f_i/f_1, where f_i is the frequency of the i-th peak divided by f_l is the frequency of the first peak, As can be seen from Fig.5-3, the 2nd, 3rd and 4th peak frequencies of each speed ratio are overtones of the 1st peak frequency independent of the speed ratio. In other words, these are harmonic components. On the other hand, the fifth peak frequency component, f_5, decreases as the speed ratio increases. Therefore, f_5 can be considered to be a component of the periodic variation of the longitudinal vortex that varies with the tip speed ratio. To compare these frequencies, a plot of the frequency against the change in f_i/f_1 is shown in Fig.5-4, and it can be seen from Fig.5-4 that the fifth peak frequency is constant at about 85 Hz at all speed ratios, which is in good agreement with the result of the periodic fluctuation of the fluid force acting on the cylinder by the longitudinal vortex obtained by the numerical analysis of Hemswan et al. The results are in good agreement with the results of Hemswan et al. When the mainstream velocity was increased from U=10 m/s to 15 m/s, there was a tip speed ratio where the fourth peak, which is a harmonic component of the natural frequency, and the fifth peak, which is caused by the longitudinal vortex, almost coincided. When the

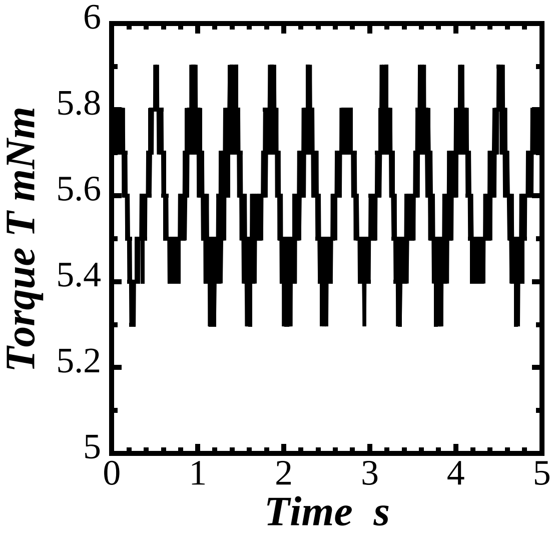

Fig.5-1 Time dependence torque (λ=0.15)

fourth and fifth peaks coincide, the frequency component is detected to be remarkably high as shown in Fig.5-2(b). Fig.5-5 shows the result of comparing the spectrum of the fifth peak frequency f_5 and the amplitude of the torque fluctuation, which is the value obtained by subtracting the time-averaged torque from the maximum torque, in order to see the effect of the fluctuations caused by the harmonic components and the longitudinal vortex. Fig.5-5 shows that the tendency of the amplitude of the torque fluctuation to increase and decrease corresponds well with the magnitude of the spectrum of f, and it can be confirmed that f_5 represents the fluctuation of the longitudinal vortex. In addition, the results for U=10 m/s shown in Fig.5-5(a) show that the torque fluctuation is very large at a tip speed ratio of λ=0.1. The results for U=15 m/s shown in Fig. 5-5(b) show that the torque fluctuation amplitude is large at not only λ=0.1 but also at 0.2. Therefore, it is necessary to avoid the coincidence between the fluctuating frequency caused by the longitudinal vortex and the harmonic components of the mechanical natural vibration in actual operation because the torque fluctuation reduces the power efficiency.

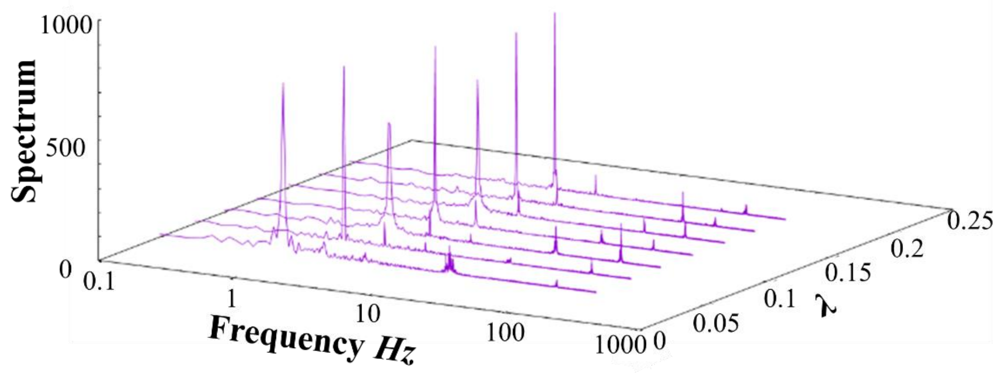

(a) U=10 m/s

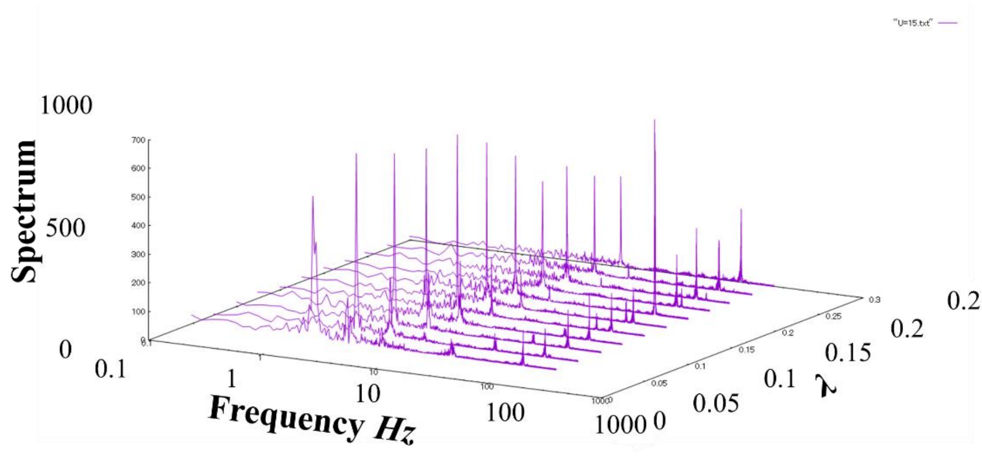

(b) U=15 m/s

Fig. 5-2 FFT result of time series torque at each tip speed ratio.

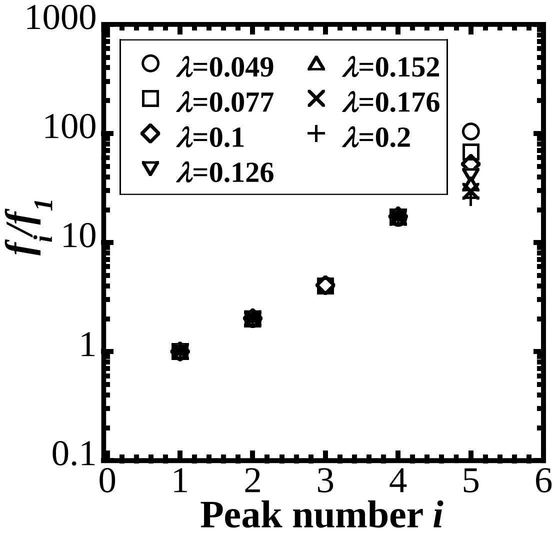

(a) U=10 m/s

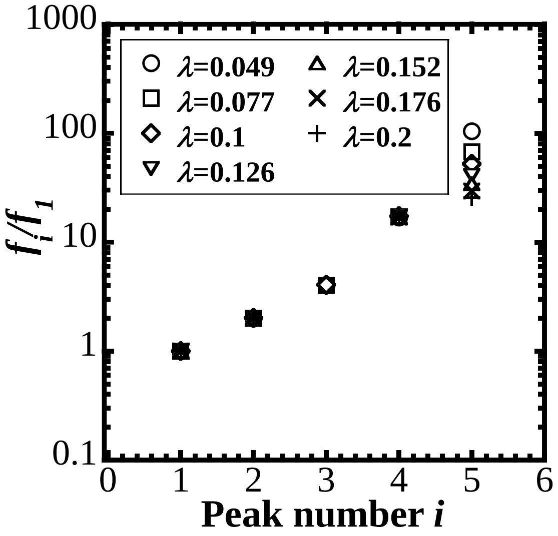

(b) U=15 m/s

Fig. 5-3 Relationship between each peak frequency and primary peak frequency.

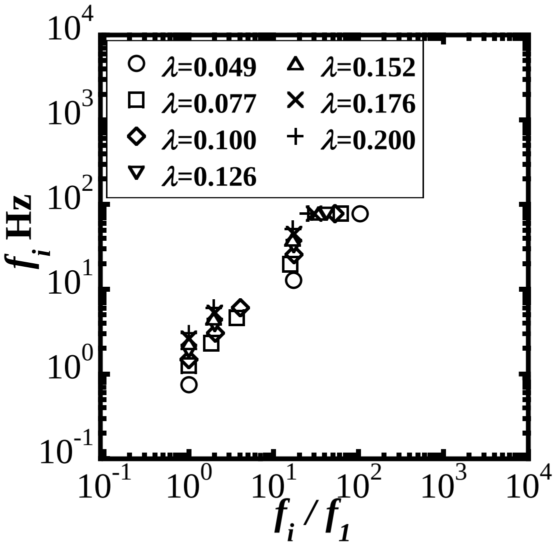

(a) U=10 m/s

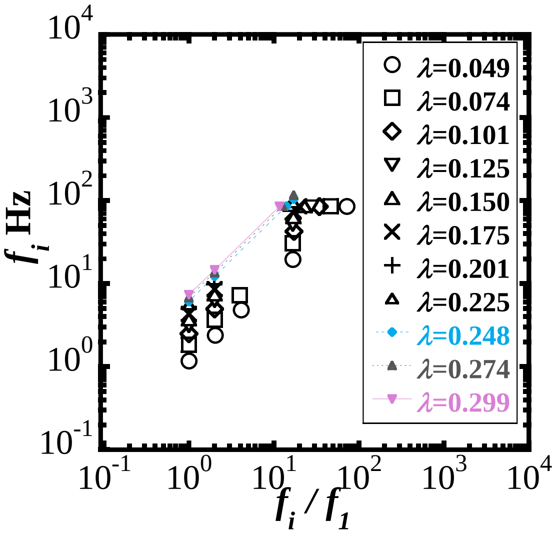

(b) U=15 m/s

Fig. 5-4 Frequency versus order of the peak frequency component at each tip speed ratio.

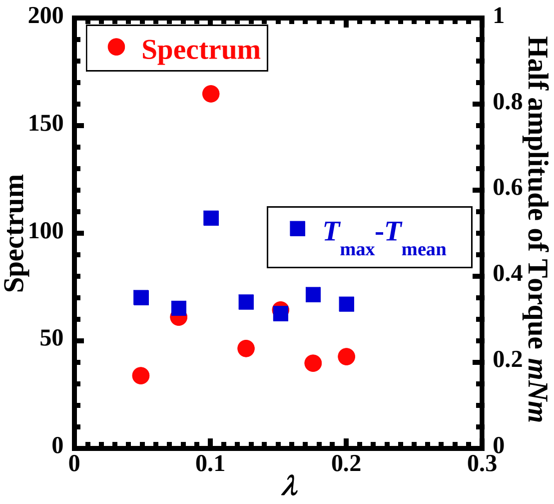

(a) U=10 m/s

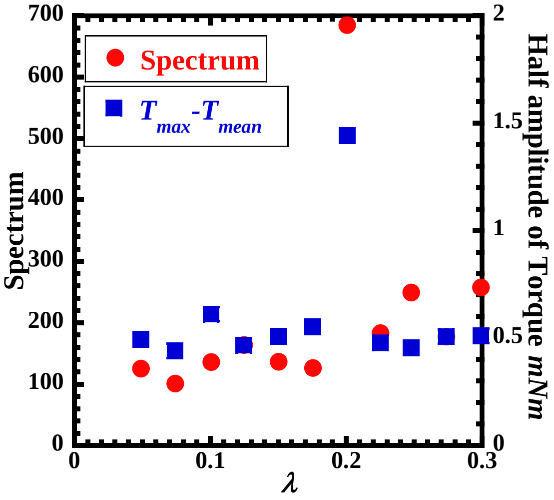

(b) U=15 m/s

Fig. 5-5 Relationship between frequency spectrum and amplitude of torque fluctuation against tip speed ratio

5.1.3 Time-Frequency Analysis

The purpose of this section is to elucidate the occurrence of temporal variation of the fluid force due to the longitudinal vortex, to observe the periodic change of the state of the longitudinal vortex from experiments and numerical analysis, and to investigate the conditions to stabilize the occurrence of the longitudinal vortex.

It is necessary to visualize the temporal changes of the longitudinal vortex in detail in order to correspond the results of the time and frequency analysis by wavelet transform to the outflow of the longitudinal vortex and the lift force acting on the cylinder. Therefore, in this section, numerical analysis is carried out using the same geometry as the experiment where the torque fluctuation was obtained, and the relationship between the shape of the longitudinal vortex and the torque is observed in detail. SCRYU/Tetra v14.1 (Software Cradle), a general-purpose thermo-fluid analysis software, was used for the numerical analysis. The computational domain used in the numerical analysis is shown in Figs. 5-6, and the conditions for generating the computational grid and the computational conditions are shown in Table 5-1. In the present analysis, the cylinder is fixed and the main flow condition is set so that the relative velocity takes into account the rotational velocity. In the present analysis, the cylinder is fixed and the relative velocity is set so that the rotational speed is taken into account. Specifically, the condition is set so that the results can be compared with the results obtained in the experiment where the rotational speed is n=44 rpm and the mainstream velocity is U=10 m/s. In order to shorten the writing time of the data, the graphic file of the analysis area was acquired after 0.4s.

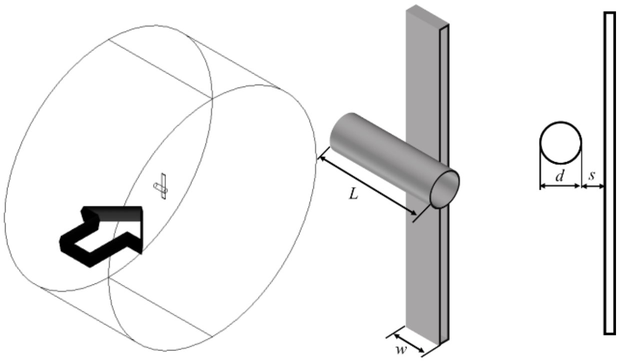

(a)Calculation region (b)Details of objects

Fig. 5-6 Numerical Domains

Table 2 Numerical setup

Test section m	$\phi 60d \times 30d$
Analysis method	LES
Turbulent model	WALE
y+	0.8
Wind velocity *U* m/s	10

Wind velocity V m/s	0.4953
Density ρ kg/m ^{3}	1.205
Viscosity μ Pa s	1.82×10^{-5}
1st boundary layer Δs m	2.193×10^{-5}
Time step Δt s	7.748 x 10 $^{-6}$

Wavelet analysis was performed on the torque signals obtained from the experiments to obtain the scalograms shown in Figs. 5-7 and 5-8, where Fig. 5-7 and Fig. 5-8 show the results for a mainstream velocity of 7.5 m/s and 10 m/s, respectively. In these figures, the horizontal axis shows the measurement time and the first vertical axis shows the frequency. Two frequency regions with high amplitude were observed in Fig.5-7. These oscillations were caused by the fluctuation of the fluid force in the longitudinal vortex and by the eccentricity of the rotating part. In Fig.5-7 and Fig.5-8, the results for high and low rotational speeds are compared, respectively, and it can be seen that the fluctuating component near 90 Hz continues to occur at the same frequency independent of the rotational speed and mainstream speed, while the other component is independent of the mainstream speed but dependent on the rotational speed. The component depending on the rotation speed can be judged to be caused by the eccentricity from its value, and the component fluctuating around 90 Hz is related to the variation of the longitudinal vortex. When the main flow speed increases to 10 m/s, the color shows an amplitude larger than 7.5 m/s, indicating that the increase in wind speed induces an

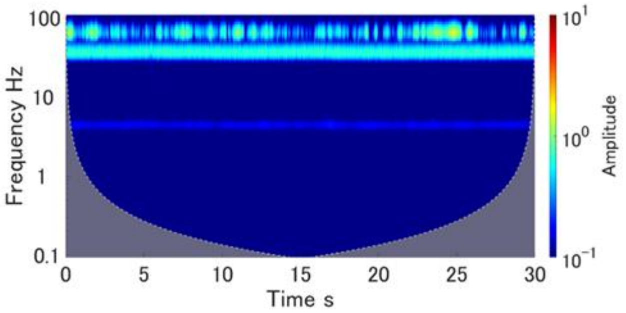

(a) n=133 rpm

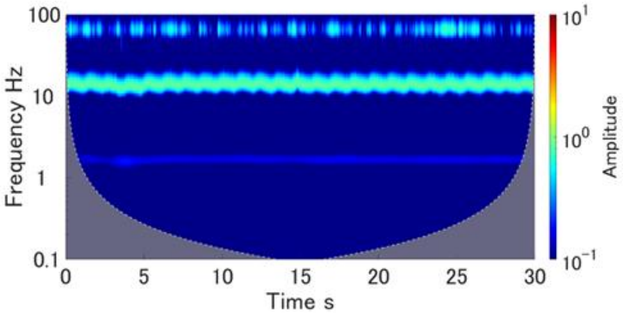

(b) n=49 rpm

Fig. 5-7 Scalogram of torque for each rotation number at U = 7.5 m/s.

increase in torque. The amplitude of the oscillation around 90 Hz fluctuates with time independently of the oscillation frequency, indicating that the larger the flow velocity, the smaller the frequency fluctuation at higher frequencies and the more stable the torque.

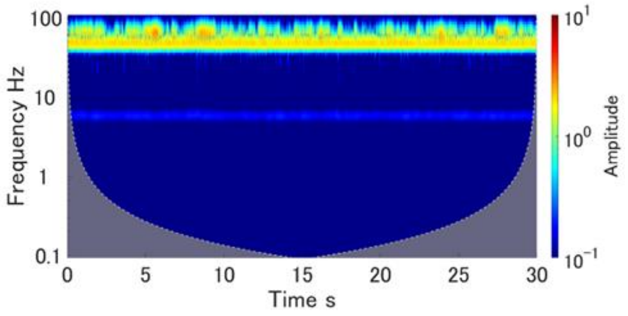

(a) n=177 rpm

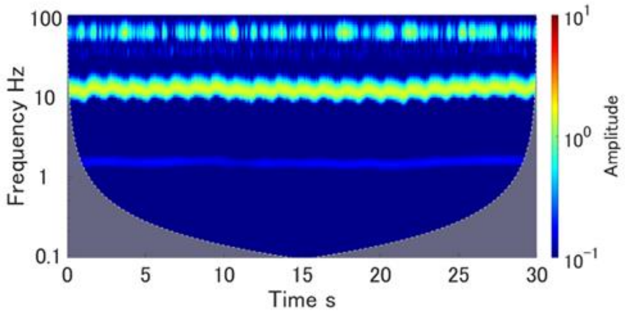

(b) n=44 rpm

Fig. 5-8 Scalogram of torque for each rotation number at U = 10 m/s.

The time series of the lift force acting on the cylinder obtained by the numerical analysis is shown in Fig.5-9, and the visualized image of the characteristic region of the waveform shown in Fig.5-9 is shown in Fig.5-10. In Fig.5-9, the full-scale graph is shown on the left, and the graph with the changed scale is shown on the right for comparison with Fig.5-10. is shown on the right. In Fig.5-10, the isosurface of the second invariant (Q-value) of the velocity gradient tensor (Hunt et al., 1988) is created, and the magnitude of vorticity is indicated by color. The Q-value of the isosurface created here is 4 × 10^{7}1/s^{2}.

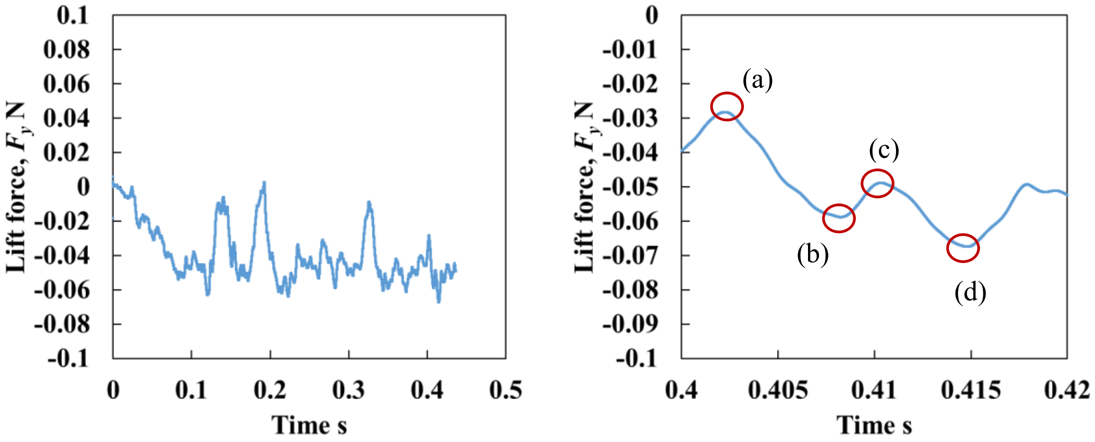

Fig. 5-9 Time varying lift force at *U* = 10 m/s, *V* = 0.4953 m/s.

From Fig.5-9, the lift force of about -0.05N is obtained stably for the time after 0.1s, but there is a part where the lift force suddenly decreases to around 0. However, there is a part where the lift force suddenly decreases to around 0. By reducing this part, it becomes possible to obtain the lift force that is stable in time. In Fig.5-9, the lift force becomes small in the region corresponding to Fig.5-10(a) and (c). On the other hand, compared with the flow fields in the regions of (b) and (d) where the lift is large, the longitudinal vortices away from the cylinder are largely retained in the gap between the cylinder and the flat plate. Therefore, a mechanism that does not retain the longitudinal vortex once it leaves the cylinder and promotes the generation of the next longitudinal vortex is considered to be necessary if high lift is to be obtained stably.

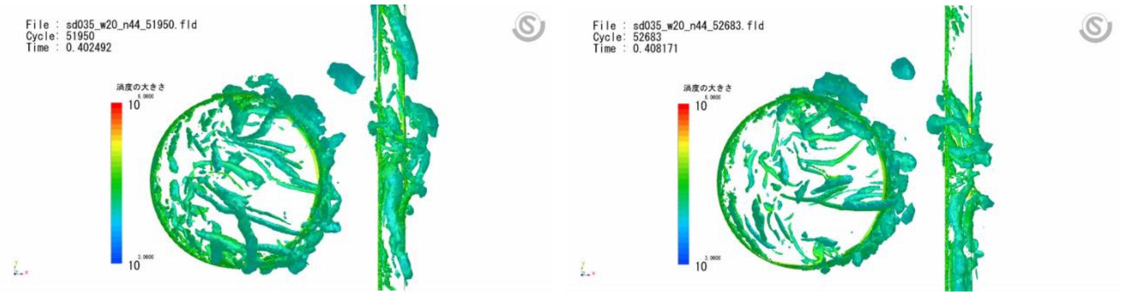

(a) Time = 0.4025 **(b) Time = 0.4082**

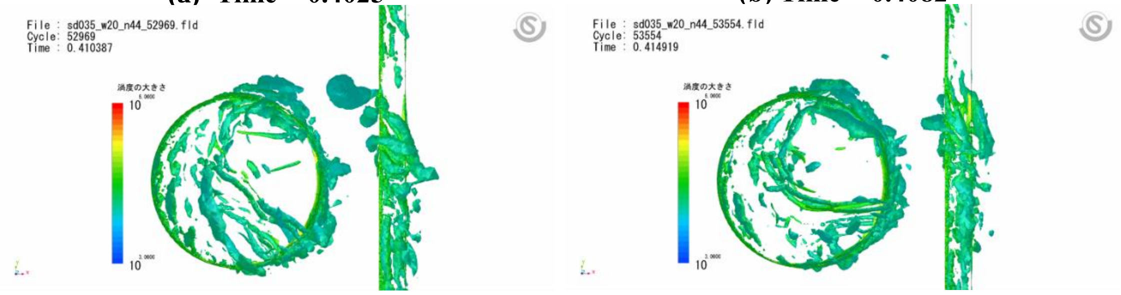

(c) Time = 0.4104 **(d) Time = 0.4149**

Fig.5-10 Visualization of longitudinal vortex from numerical analysis results in each time (Q criterion = 4×10^{7} 1/s ^{2}).

5.2 Transient response

In the previous section, it was experimentally found that the torque as the driving force fluctuates due to the periodic fluctuation of the outflow of the longitudinal vortex. In the practical use of wind turbines, the temporal stability and transient response of the power are necessary to know the behavior when the wind speed fluctuates in the real environment and the load fluctuates by braking. This is especially important for small and medium-sized wind turbines, which can be used in regions where the wind speed fluctuates rapidly, unlike large wind turbines. The response of vertical axis wind turbines to step wind (Hayashi et al., 2008), the effect of the moment of inertia on the transient response (Hayashi et al., 2013), and the response of small wind turbines to wind speed and load fluctuations have been investigated. (Hayashi et al., 2013), and the response of small wind turbines to fluctuations in wind speed and load (Karasudani et al., 2007). In the case of circular cylinder blade wind turbines, it is considered that the vortex stability affects the power from the power theory. Therefore, in this section, experiments are conducted to clarify the effects of the wind turbine shape factor and load condition on the temporal characteristics of the power.

5.2.1 Procedure of the load variation experiment

In order to measure the torque that fluctuates with the change of driving conditions while the wind turbine is rotating, experiments were conducted using the power adding device shown in 2.3.2. The static power characteristics were obtained by setting the no-load speed as N_{max} and the maximum load speed as N_{tmax}. The load was controlled in increments of 50 rpm from N_{max} to N_{tmax}, and the change in time from the initial rotation speed Ni forced by the motor to the final steady-state rotation speed Ns

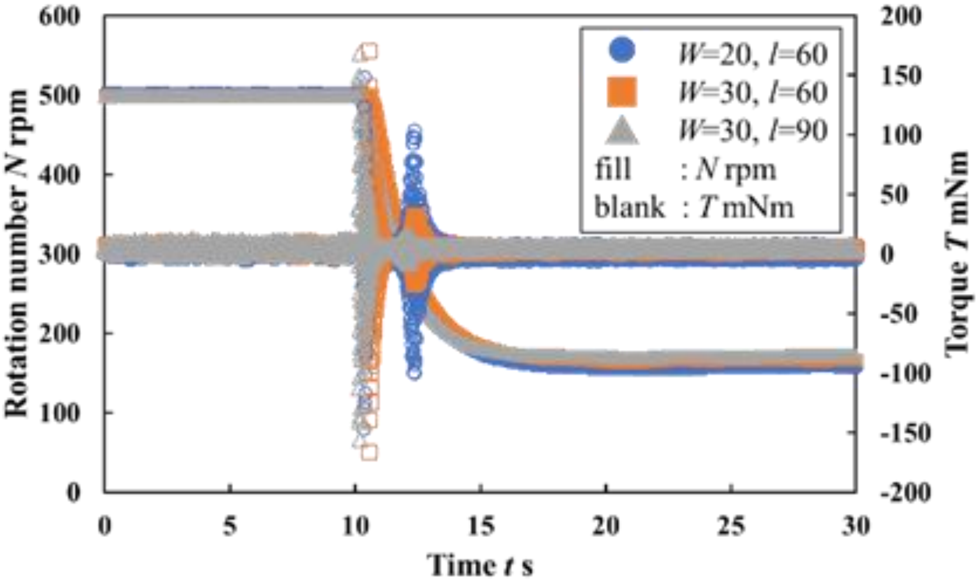

(a) Transient response at Ni=500rpm, Ns=160rpm.

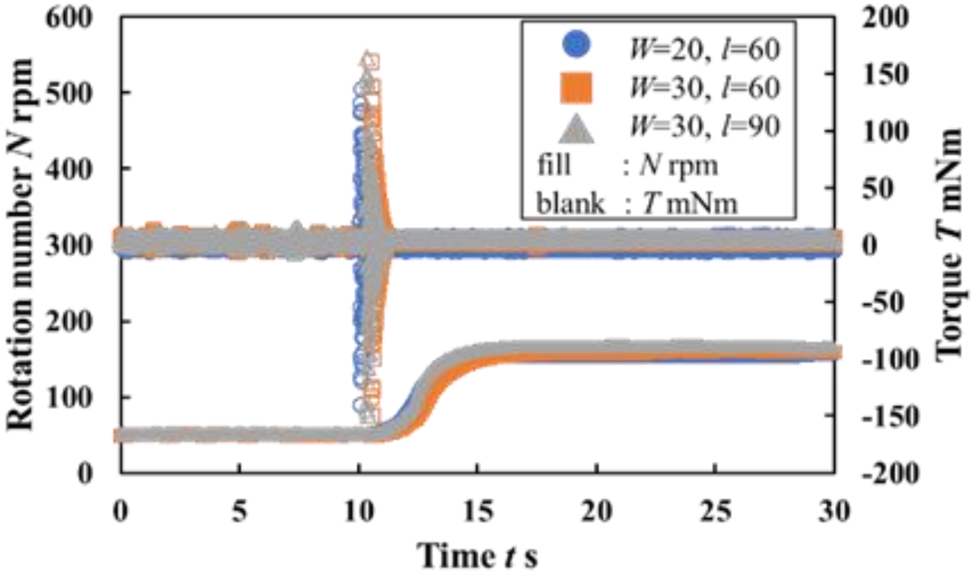

(b) Transient response at Ni=50rpm, Ns=160rpm.

Fig.5-11 Experimental results of transient response at s/d=0.35 d=20mm, W=20, 30mm, l=60, 90mm.

under constant load conditions was measured. The details of the experimental sequence are as shown in 2.4.4.

5.2.2 Effect of initial speed on transient response

Fig.5-11(a) shows the results for *Ni*=500 rpm and *Ns*=160 rpm, and Fig.5-11(b) shows the results for *Ni*=50 rpm and *Ns*=160 rpm. As shown in Fig.5-11(a), when *Ni*>*Ns, the* rotation speed immediately decreased after the forced rotation was unloaded. On the other hand, as shown in Fig.5-11(b), when Ni< *Ns*, there was a time difference until the rotation speed started to increase after the forced rotation was unloaded.

5.2.3 Effect of the difference between the steady-state speed and the initial speed on the rise time

The effect of the difference between the steady-state speed and the initial speed, *Ns-Ni, on* the time constant is evaluated. In Fig.5-12(a) and Fig.5-12(b), the time constants for W=20mm and W=30mm, respectively, are shown for the *s/d* condition. The positive region shows the experimental results where the rotation speed was decreased from Ni=50, 500 rpm under *Ni*>*Ns.* Fig.5-12 shows that the time constant becomes shorter as the difference in rotation speed increases in the case of *Ni*<*Ns* and recovery from low to high rotation speed. In the case of *Ni*>*Ns, the* time constant tended to become longer as the difference in rotation speed increased. In the case of *Ni*>*Ns, the* time constant was shorter and the change was smaller than that of *Ni<Ns*. From these results, aerodynamic drag is considered as a factor that acts as a brake against the driving force and the driving obtained by the longitudinal vortex. In the case of the transition from low to high rotation, the braking action gradually becomes stronger and the time constant becomes shorter as the difference in rotation speed becomes larger. Hayashi et al. (Hayashi et al., 2008) found that the time constant for the transient response of a straight blade vertical axis wind turbine is about 20s when the time constant is the time from the start of the change to 63.2% of the steady state value when the rotation speed changes from low to high. It can be said that the time constant of the wind turbine in this section is shorter and more stable than that of the straight blade vertical axis wind turbine.

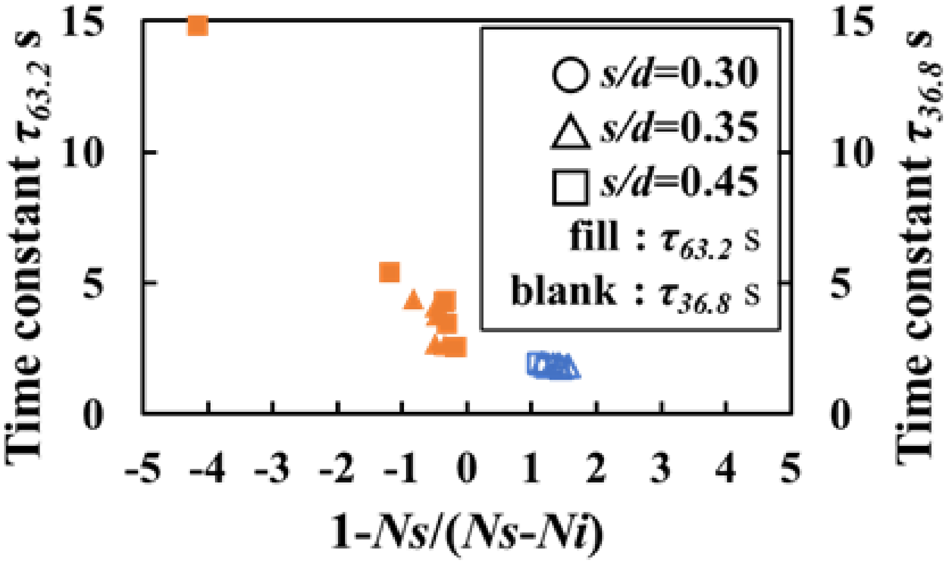

(a) Time constant at d=20 mm, W=20 mm, l/W=3.

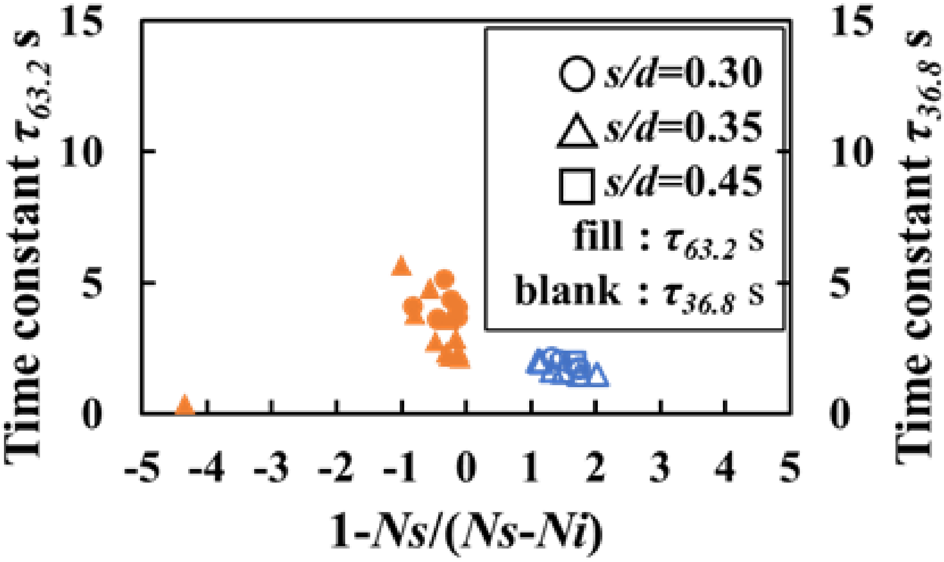

(b) Time constant at d=20 mm, W=30 mm, l/W=3.

Fig.5-12 Effect of the change in *1-Ns/(Ns-Ni)* on the time constant.

5.3 Chapter 5 Conclusion

In section 5.1, the frequency characteristics of the periodic fluctuation of the fluid force due to the longitudinal vortex that has been reported so far were obtained from experiments. From the results, it was found that the amplitude of the torque fluctuation increased significantly when the frequency of the harmonic component of the fluctuation due to the mechanical factor and the fluctuation component due to the longitudinal vortex matched.

The time-frequency characteristics of the crossed-cylindrical structures were compared with the results of the numerical analysis of the flow field. It is found that the longitudinal vortices are generated in the gap between the crossed cylinders and the flat plate when the crossed cylinders and the flat plate are installed in a uniform flow and that the stagnation state of the longitudinal vortices at the intersection greatly affects the magnitude of the fluid force.

In section 5.2, experiments were conducted to clarify the temporal characteristics of the power of a cylindrical blade wind turbine by changing the circular cylinder blade diameter, blade length, flat plate width, gap ratio, and initial rotation speed. As a result, it was found that the time constant became shorter in inverse proportion to the magnitude of the fluctuation when moving from low to high rotation, but the opposite was true when moving from high to low rotation. It was also found that the circular cylinder blade wind turbine driven by the longitudinal vortex is a very stable system compared with the lift-driven straight blade vertical axis wind turbine.

Chapter 5 References

Hayashi, T., Kang, I., Hara, Y. and Kawamura, T., Transient response of a straight-bladed vertical axis wind turbine to step wind, Transactions of the Japan Society of Mechanical Engineers, Series B, Vol. 74, No. 738 (2008), pp. 406-413.

Hayashi, T., Hara, Y., Azui, T., Kang, I., and Kawamura, T., Transient response of a vertical axis wind turbine in the change of wind speed (Effects of moment of inertia), Transactions of the Japan Society of Mechanical Engineers, Series B, Vol. 79, No. 801 (2013), pp. 953-965.

Hemsuwan, W. et al, A longitudinal vortex wind turbine: a numerical study, Journal of Wind Engineering and Industrial Aerodynamics, Vol. 180 (2018), 213- 230.

Hunt, J. C. R., Wray, A. A., and Moin, P., Eddies, streams, and convergence zones in turbulent flows, Center for Turbulence Research Report CTR-S88 (1988), pp. 193-208.

Karasudani, T., Ohya, Y. and Watanabe, K., On the response of small wind turbines to changes of wind speed and load, Journal of JWEA, Vol. 30, No. 2 (2007), pp. 120-123. 120-123.

6. Generation of galloping using a necklace vortex

6.1 Chapter 6 Introduction

Hemsuwan et al. performed a numerical analysis of a crisscrossing system in which the downstream side is a flat plate of width *w=d and* the upstream cylinder moves vertically along the downstream flat plate at a velocity *V* while keeping the gap *s* constant. It was shown that at specific values of the gap ratio *s/d* and velocity ratio *V/U*, a longitudinal Necklace vortex (NV) forms at a stationary position with respect to the moving upstream cylinder, and the asymmetric pressure distribution caused by the stationary NV generates a fluid force acting on the upstream cylinder in the direction of motion (Hemswan et al., 2018; Hemswan et al., 2019). Based on these results, Sakamoto et al. developed a wind turbine with a circular cylinder blade driven by the stationary formation of NV, called a longitudinal vortex linear drive wind turbine, and clarified its basic performance through wind tunnel experiments (Sakamoto et al., 2021). These previous studies suggested that the force acting in the initial motion direction is generated by the motion of the cylinder and that the fluid elastic instability oscillation is induced by the localization of NV. In other words, the velocity ratio between the mainstream velocity and the motion of the cylinder in the initial motion direction is considered to be an important parameter for the driving force of the cylinder. The cylinder is driven within the range where the fluid force acting on the cylinder matches the driving direction for this velocity ratio. When the fluid force exceeds the mechanical resistance such as air resistance and frictional force, the cylinder starts to rotate as a wind turbine. Therefore, by measuring the fluid force against the velocity ratio, it is possible to determine the starting and driving conditions when designing the wind turbine.

Therefore, in this chapter, wind tunnel experiments were conducted to confirm this hypothesis. First, λ-C_z was obtained by the method shown in Section 2.4.1 using the wind-tunnel type fluid force measurement device shown in Section 2.2.1. Next, the oscillation behavior was investigated using the pendulum-type amplitude measurement device shown in Section 2.2.4. Finally, a method to estimate the vibration amplitude based on the quasi-steady state theory is proposed, and the results of the vibration experiment are compared with the predictions using the results of the λ-C_z force obtained from the wind turbine type hydrodynamic measurement experiment. Since the main subject of this paper is a rotating wind turbine, the galloping described in this chapter is an example of an oscillating system.

In Chapter 5, the prediction method of the hydrodynamic force measurement experiment described in this chapter is extended to the yaw angle, and the change of the state of the longitudinal vortex during driving is discussed by comparing the results of the hydrodynamic force measurement.

6.2 Experimental results and discussion

6.2.1 Fluid force acting on a circular cylinder blade

Fig.6-1 shows the relationship between the hydrodynamic force coefficient C_z and the velocity ratio λ of the wind turbine type hydrodynamic force measurement system at U=10 m/s (Re=13,500) with different values of the gap ratio s/d. The solid line is an approximation of the relationship between the lift coefficient C_l of stationary NV and the velocity ratio λ proposed by Sakamoto et al. (Sakamoto et al., 2021). $s/d \leq 0.3$, C_z is negative, i.e., the force acting on the circular cylinder blade throughout the measurement range of λ is the drag force against rotation. For s/d=0.35, C_z was scattered around zero for λ<0.1, suddenly jumped to a positive value for λ=0.1, then decreased linearly with increasing λ, and became negative for λ>0.25. The trend of the λ-C_z relationship for 0.4≤s/d≤0.6 is that the linear relationship between C_z and λ *holds at the* minimum value of λ close to zero. The trend of the λ-C relationship for $0.4 \leq s/d \leq 0.6$ is similar to that for s/d = 0.35, except that the linear relationship between C and λ holds when the minimum value of λ is close to zero.

Overall, the λ-C_z relationship showed the following characteristics for all values of s/d: for $\lambda < 0.25$, C_z decreased linearly with increasing λ and approached a constant value as λ continued to increase. Compared with previous studies (Hemsuwan et al., 2018; Hemsuwan et al., 2019; Sakamoto et al., 2021), this can be explained as follows: when λ is smaller than a certain threshold depending on s/d, NV does not form in a stationary position and the rotation of the cylinder For s/d≥0.35 and λ above a threshold, the NV forms in a stationary position and positive hydrodynamic forces act in the span-width region near the downstream ring plate. As λ increases, the hydrodynamic force due to the NV disappears and the drag force becomes dominant, and the coefficient C_z becomes a negative constant. The tendency of the relationship between C_z and λ and the range of s/d and λ *when* C_z is positive are in

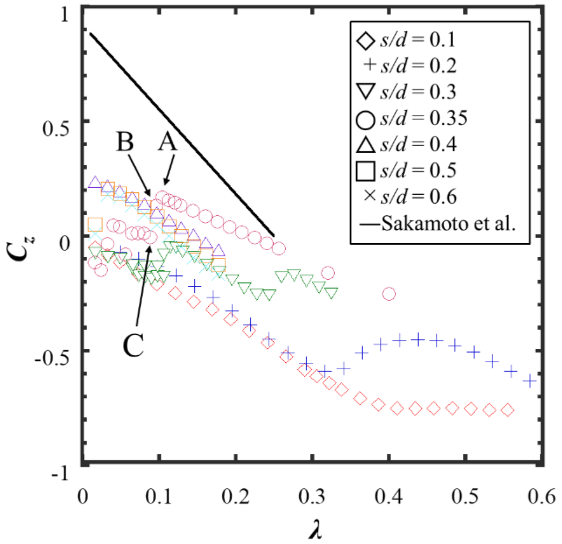

Fig. 6-1 Lift coefficient vs. velocity ratio at U = 10 m/s (Re = 13,500)

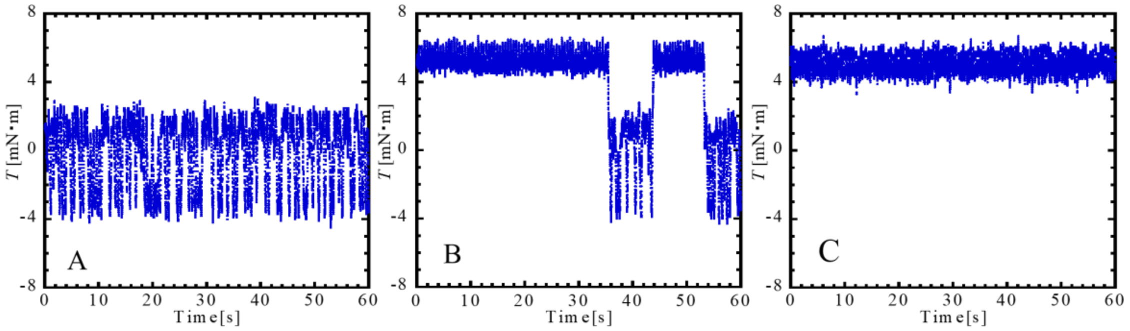

Fig. 6-2 **Torque signals for s/d=0.35 and U=10 m/s (Re=12,500) at A, B and C in Fig.** 6-1.

good agreement with the results of Sakamoto et al. (Sakamoto et al., 2021). The value of C_z defined by equation (2) is much lower than that of Sakamoto et al. because the drag force is excluded in their estimation and the effective blade length l_e is much larger than the virtual span length l_{NV} of NV used to define C_l.

The output signals of the torque meter corresponding to the three values of λ for s/d=0.35 shown in A, B and C in Fig.6-1 are shown in Fig.6-2. Comparing the torque signals of the three cases, it can be seen that the flow characteristics are different between A and C, and the transient period, B, is intermittently switched into two regions. That is, in A, NV is not formed at rest (λ = 0.09) and the torque fluctuates around a small negative value, whereas in C, NV is formed at rest against the rotating cylinder (λ = 0.11) and a positive torque is generated. At the intermediate value of λ = 0.1, the static formation of NV is not stable and the flow switches irregularly as shown in signal B. Thus, Fig. 6-1 and Fig. 6-2 confirm that the motion of the cylinder causes the static formation of NV and the generation of positive fluid force.

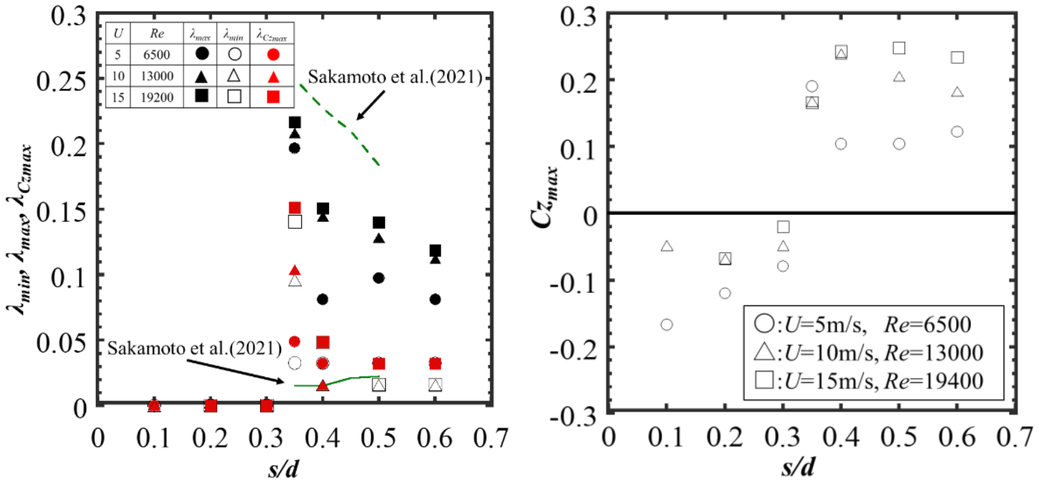

(a) Velocity ratio range for positive C_z (λ_{min}, λ_{max}) and λ_{Czmax} plotted against *s/d* for *U* = 5, 10, and 15 m/s (*Re* = 6480, 13500, and 19500) compared with operation range of λ for LV-WT by Sakamoto, et al. (2021).

(b) Maximum $C_z$vs. *s/d*

Fig. 1 -3 Velocity ratio for lift generation and maximum lift coefficient for *Re* = 6480, 13000, and 19500

In Fig. 6-3(a), the minimum and maximum values of λ for $C_z > 0$, $\lambda_{\min}$, and $\lambda_{\max}$ are plotted against s/d and compared with the results for the LV-WT operating range by Sakamoto et al. The range of positive C_z values of s/d and λ in Fig. 6-3(a) correlates well with the results obtained by Sakamoto et al. (Sakamoto et al., 2021) for the operating range of a circular cylinder blade wind turbine. In both experiments, the generation of hydrodynamic force was confirmed to be due to the steady-state formation of NV. The maximum value of the hydrodynamic force coefficient, $C_{z\max}$, seems to increase with the Reynolds number, *Re*, but its velocity ratio, $\lambda_{Cz\max}$, is independent of *Re*.

In order to predict the vibration amplitude using the method described in section 6.3, the relationship between C_z and λ was approximated by a linear decreasing function (Sakamoto et al., 2021).

$$C_z = C_a - C_b\lambda \tag{6-1}$$

From the results of Fig.6-1, the constants C_a and C_b are calculated by the least-squares method and plotted against *Re* and *s/d* in Fig.6-4. In Fig.6-4(a), the value of C_a increases slightly with increasing *Re* when *s/d* is fixed, but there is no systematic trend in the dependence of C_b on *Re*. However, as shown in Fig.6-4(b), C_a is almost independent of *s/d, and* C_b increases steadily with *s/d*.

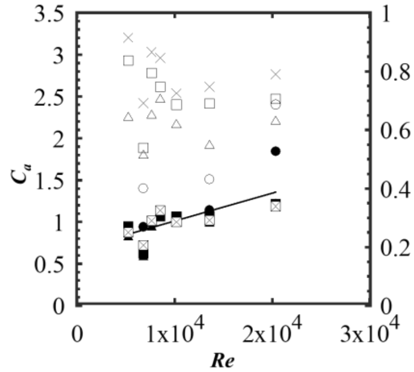

s/d	C_a	C_b
0.35	●	○
0.4	▲	△
0.5	■	□
0.6	⊠	×

- $C_a = 0.195 + 9.5\times10^{-6}\,Re$

(a) **C_a, C_b vs. *Re* for various *s/d***

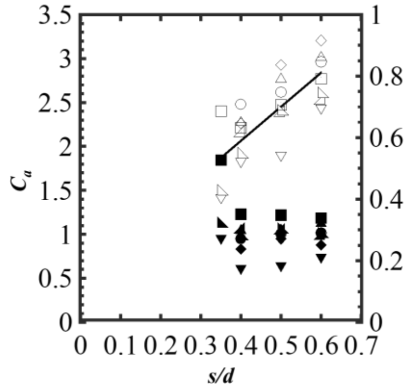

Re	C_a	C_b
5211	◆	◇
6780	▼	▽
7607	●	○
8502	▲	△
10169	◢	◿
13559	◣	◺
20339	■	□

- $C_b = 0.515 + 3.88 \times s/d$

(b) **C_a, C_b vs. *s/d* for various *Re***

Fig. 6-4 Coefficients C_a and C_b in approximation Eq. (6-1) for lift coefficient $C_z \sim \lambda$

6.2.2 Pendulum-type amplitude

Fig. 6-5 shows an example of the vibration response of the pendulum-type amplitude measurement system to the flow velocity *U*. The legend of Fig. 6-5 and the notes of Up and Down in Fig. 6-7 show the plots of the increasing and decreasing processes of *U*, respectively. When U is increased stepwise from a low value, the cylinder of the pendulum remains almost stationary up to a maximum velocity of about U=4 m/s. However, when a certain amount of displacement is applied at the maximum speed, oscillation with a constant amplitude and a frequency slightly lower than the natural frequency f_n is obtained, which is the final state. In Fig. 6-5, when *U* decreases slightly from 3 m/s, the Z_{rms} amplitude of the vibration suddenly drops to almost zero. In this chapter, the amplitude and velocity just before the sudden decrease of Z_{rms} observed in the Down process are defined as the critical amplitude of

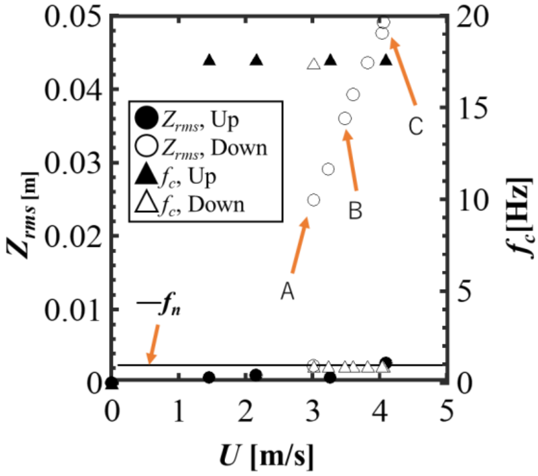

Fig. 6-5 Vibration amplitude and frequency vs. flow velocity for Model I (*s/d* = 0.5, *Sc* = 94)

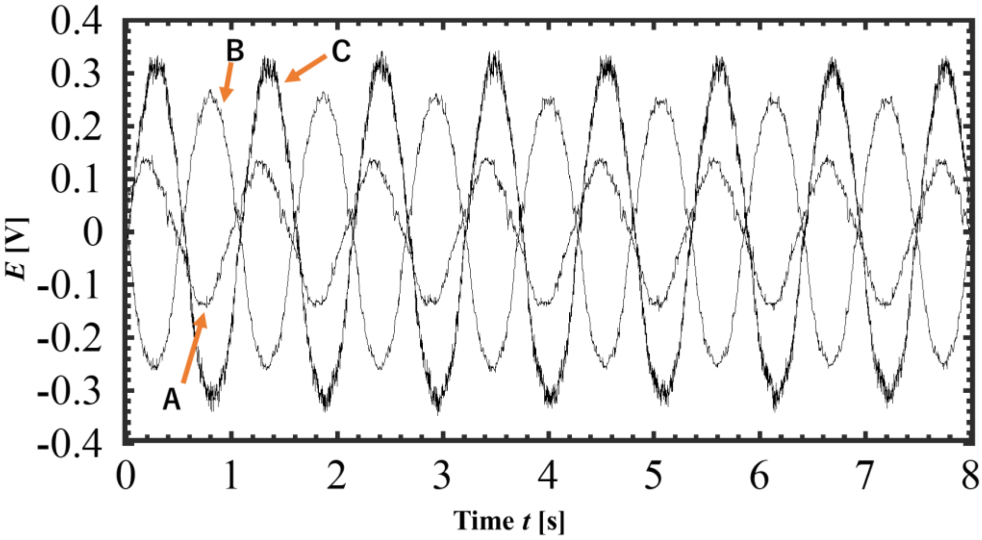

Fig. 6-6 Output signals for pendulum displacement at A (*U* = m/s), B (*U* = m/s), and C (*U* = m/s) in Fig. 6-4 (Model I, *s/d* = 0.5, *Sc* = 94)

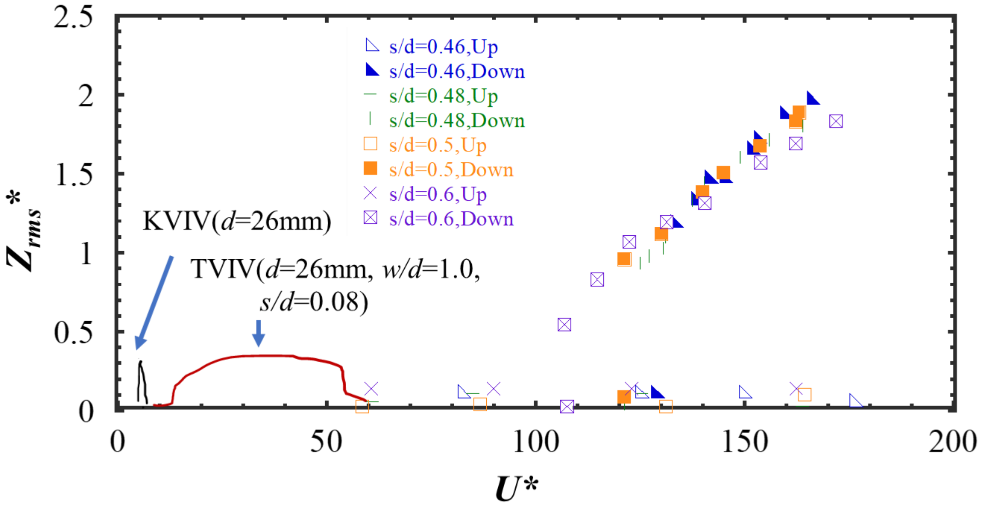

(a) **Model I, *Sc* = 94**

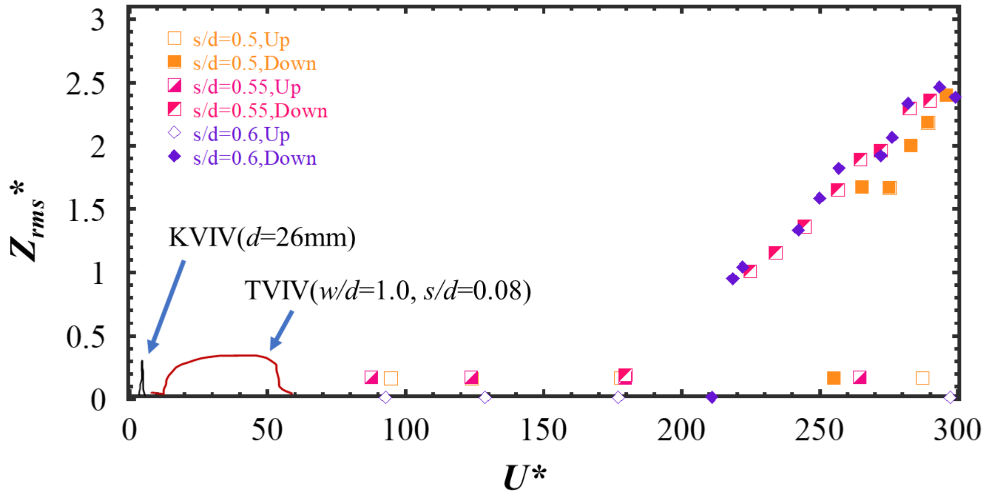

(b) **Model II, *Sc* = 430**

Fig. 6-7 Non-dimensional amplitude vs. reduced velocity for various *s/d* values compared with KVIV and TVIV

vibration $[Z_{rms}]_{crit}$ and the critical velocity U_{crit}. Fig. 6-6 shows the oscillograms of the displacement signals at three velocities with considerable amplitude of vibration for $U \geq U_{crit}$ shown in A, B and C of Fig. 6-5. The oscillations were found to be almost purely sinusoidal, independent of U and with a frequency slightly lower than f_n.

In Figs. 6-7, the vibration amplitudes, non-dimensionalized by the cylinder diameter *d, are* plotted against the reduction velocity $U^* = U/(f_n d)$ *for various* values of *s/d* (0.46 ≤ *s/d* ≤ 0.6 for Model I and 0.5 ≤ *s/d* ≤ 0.6 for Model II). The results are compared with those of KVIV for a single cylinder and TVIV for a crossed cylinder-plate system reported by Kato et al. As seen in Fig. 6-5, the frequency of the large oscillation at $U \geq U$ in the Down process is significantly higher than that in Model I (Fig. 6-7(a), *Sc* = 94). As can be seen in Fig. 6-5, the frequency f_c of the large oscillation at $U \geq U_{crit}$ in the

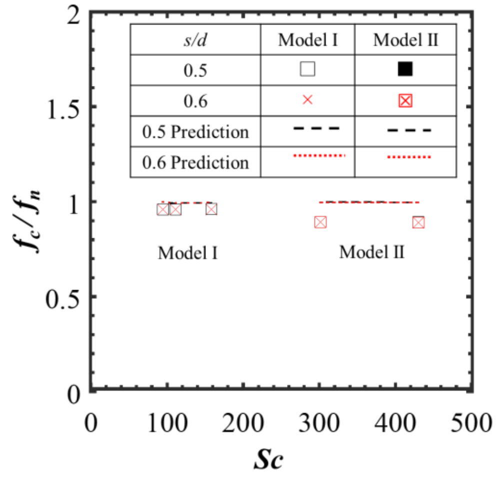

Fig. 6-8 Normalized vibration frequency vs. Scruton number for *s/d* = 0.5 and 0.6

down process is almost independent of *U*. Therefore, in comparison with the calculation given in section 6.3, f_c/f_n is plotted for *Sc* with *s/d*=0.5 and 0.6 in Fig. 6-8. As can be deduced from Eq. (6-5), f_c/f_n is slightly lower than 1 for these two models due to the lower value of the damping ratio ζ, indicating that the dependence on *U** and *Sc is insignificant*.

Fig. 6-9(a) plots the critical decay rate U^*_{crit} against *Sc* for various values of *s/d*, and Fig. 6-9(b) plots the dimensionless amplitude Z_{rms} $^*_{crit}$ of U^*_{crit} against *s/d*. As seen in Fig. 6-9(a), U^*_{crit} increases with *Sc,* but the dependence on *s*. As seen in Fig. 6-9(a), *U** increases with *Sc*, but there is no systematic trend in its dependence on *s/d*. However, Z_{rms} $^*_{crit}$ decreases steadily with *s/d*, but shows only a small dependence on *Sc (*see Fig. 6-9(b)). It should be noted that the jump in vibration amplitude given by $Z_{rms}{}^*_{crit}$ is considerably larger than that of a single prism (Kawabata et al., 2012; Azhar et al.,

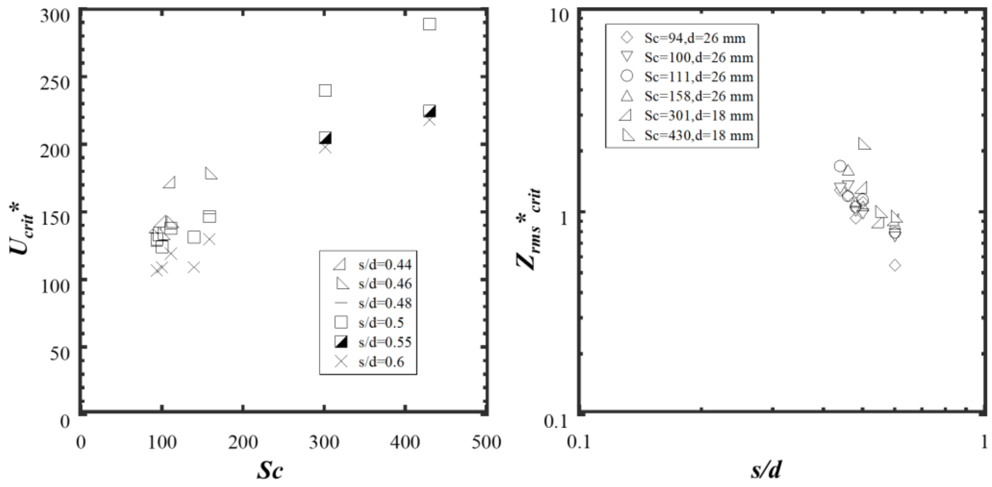

(a) U_{crit} * **vs.** ***Sc*** **for various values of** ***s/d*** (b) $Z_{rms}{}^*_{crit}$**vs.** ***s/d*** **for various values of** ***Sc***

Fig. 6-9 2Critical reduced velocity U_{crit} * and non-dimensional critical vibration amplitude at U_{crit}*

2020).

In Figs. 6-5~6-9, the features of the large vibration common to the two models are as follows: 1) the minimum reduction velocity of the vibration, U^*_{crit}, is much larger than that of the isolated cylinder KVIV or the crossed cylinder-plate TVIV; 2) the jump of the vibration amplitude, $Z_{rms}{}^*_{crit}$, at U^*_{crit} is very large; 3) the vibration amplitude $Z_{rms}{}^*$ increases divergently with $U^* > U^*_{crit}$ at frequencies close to the natural frequency f_n up to the maximum measured velocity, and 4) the hysteresis behavior is remarkable. Even when U^* *is* increased stepwise up to the maximum velocity, $Z_{rms}{}^*$ remains almost zero, and when an initial amplitude is given at the maximum velocity and stable vibration is induced, $Z_{rms}{}^*$ *decreases* gradually even when U^* is decreased stepwise, so that $U^* \geq U^*_{crit}$. This remarkable hysteresis can be attributed to the threshold of the velocity ratio λ at which NV is formed steadily, as shown in Fig. 6-3(a).

Among the above features, 1) and 3) are known to characterize isolated cylinder galloping (Azhar et al. 2021; Kawabata et al. 2013), while 2) and 4) are unique to the oscillations of the pendulum-type amplitude measurement device in this study. These facts suggest that the oscillations of the pendulum-type amplitude measuring device are caused by fluid elastic instability oscillations rather than periodic vortex outflows. Therefore, this vibration is classified as a kind of galloping caused by the downstream flat plate.

To investigate the dependence of the galloping amplitude on *Sc,* the values of $Z_{rms}{}^*$ at typical values of $U^* > U^*_{crit}$ ($U^* = 150$ for Model I and $U^* = 250$ for Model II) are plotted against *Sc* in Figure 6-10. The values of s/d=0.5 and 0.6 were selected because of the abundance of measurement data. In the absence of measurement data, interpolation was performed to obtain $Z_{rms}{}^*$ values at typical speeds. The solid lines in the figure are calculated by the method described in Section 6.3.

6.3 Amplitude prediction methods

In this section, the quasi-steady state theory is applied to the excitation force of the pendulum-type amplitude measuring device. In other words, it is assumed that the steady lift force obtained by the wind turbine-type hydrodynamic force measuring device acts on the cylinder of the pendulum-type amplitude measuring device at an arbitrary phase of vibration. This force is expressed by applying equation (6-1) to the fluid force coefficient. If we simplify the pendulum-type amplitude measuring device as a mass-zero string-suspended quality point, the equation of motion of the quality point can be written as

$$m_e\frac{d^2Z}{dt^2}+c_e+=kZ=(C_a-C_b\lambda)\cdot\frac{1}{2}\rho U^2(dl) \qquad (6\text{-}2)$$

Since the damping of the two models is under-damped and λ = V/U=(*dZ/dt*)/*U*, the solution to equation (6-2) for the initial conditions is

$$Z=Z_0 \text{ and } \frac{dZ}{dt}=0 \text{ at } t=0 \qquad (6\text{-}3)$$

$$Z=e^{-\frac{1}{2}Ct}\left(Z_0-\frac{F}{K}\right)\left(\cos\Omega_G t+\frac{C}{2\Omega_G}\sin\Omega_G t\right)+\frac{F}{K} \qquad (6\text{-}4)$$

where

$$C=\frac{1}{m_e}\left(c_e+\frac{1}{2}C_b\rho U\,dl\right)$$

$$F=\frac{C_a}{m_e}\left(\frac{1}{2}\rho U^2\,dl\right)$$

$$K=\frac{k}{m_e}$$

where Ω *is* $_G$the angular frequency of the vibration, given by

$$\Omega_G=\frac{1}{2}\sqrt{4K-C^2} \qquad (6\text{-}5)$$

When the displacement Z_P (i.e., $t=t_P=\pi/\Omega_G$) half a cycle after t = 0 is $-Z_0$. it becomes a steady oscillation with constant amplitude. Therefore, if $Z_P = [Z]_{tP} = -Z_0$ in equation (6-4), the amplitude of the steady oscillation is

$$Z_p = \frac{F}{K}\frac{1}{\tanh X} \tag{6-6}$$

where

$$X = \frac{1}{4}\,\pi C/\Omega_G \tag{6-7}$$

Equation (6-5) for the vibration frequency can be rewritten as follows

$$f_c/f_n = \Omega_G/(2\pi f_n) = \sqrt{1-\left\{\zeta+\frac{1}{2c_c}(C_b\rho U d l)\right\}^2} \tag{6-8}$$

Applying the equations in Fig. 6-4 to the constants C_a , C_b , the vibration amplitude Z_P and the frequency f_c/f_n can be calculated using equations (6-6) and (6-8) when *s/d*, *Sc* and *U* are given. The solid or dashed lines in Figs. 6-8 and 6-10 show the results of the calculations. In Figs. 6-11 and 6-12, the results of the calculation of the relationship between Z_{rms} and *U* are* compared with the measurement results of the two models. In Figs. 6-11 and 6-12, the calculated relationship between Z

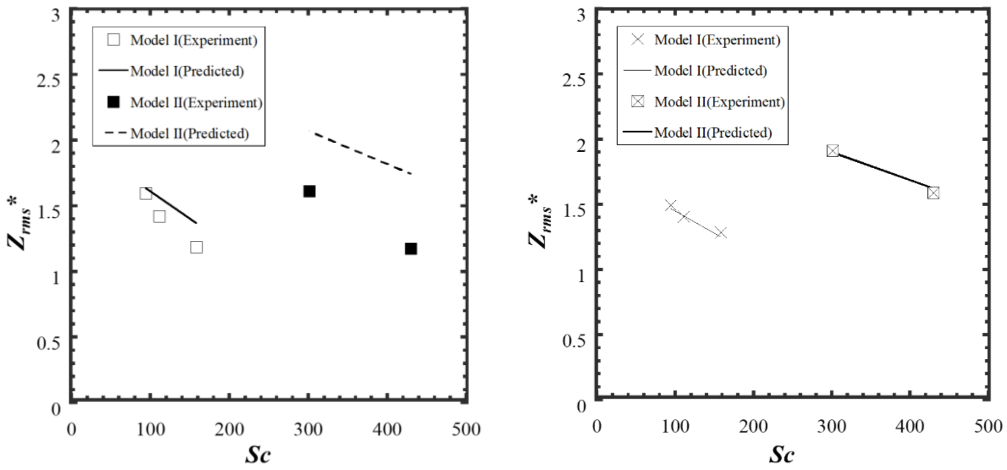

(a) Z_{rms}* at U*=150 (Model I) and U*=250 (Model II) vs. *Sc* for s/d=0.5.

(b) Z_{rms}* at U*=150 (Model I) or U*=250 (Model II) vs. *Sc* for s/d=0.6.

Fig. 6-10 Non-dimensional galloping amplitude Z_{rms}* vs. *Sc* for s/d=0.5 and 0.6 (U*=150 for Model I and U*=250 for Model II)

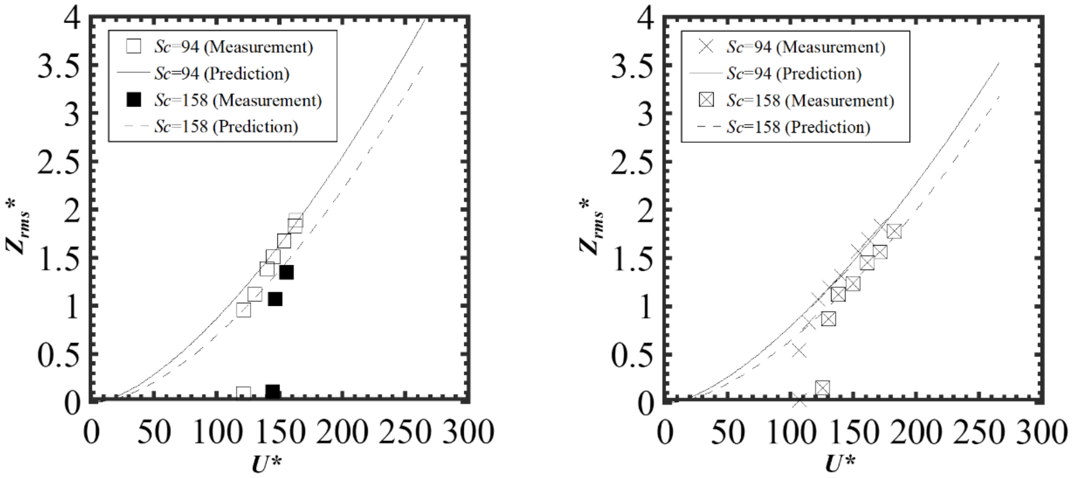

(a) *s/d* = **0.5** (b) *s/d* = **0.6**

Fig. 6-11 Z_{rms}*vs. *U**for Model I at *Sc* = 94 and 158 (comparison between measurement and prediction)

and *U*.

Although simplification and coarse approximation are adopted in the analysis, the agreement between the calculated and measured results is generally good for the galloping amplitudes with $U^* > U^*_{\text{crit}}$.

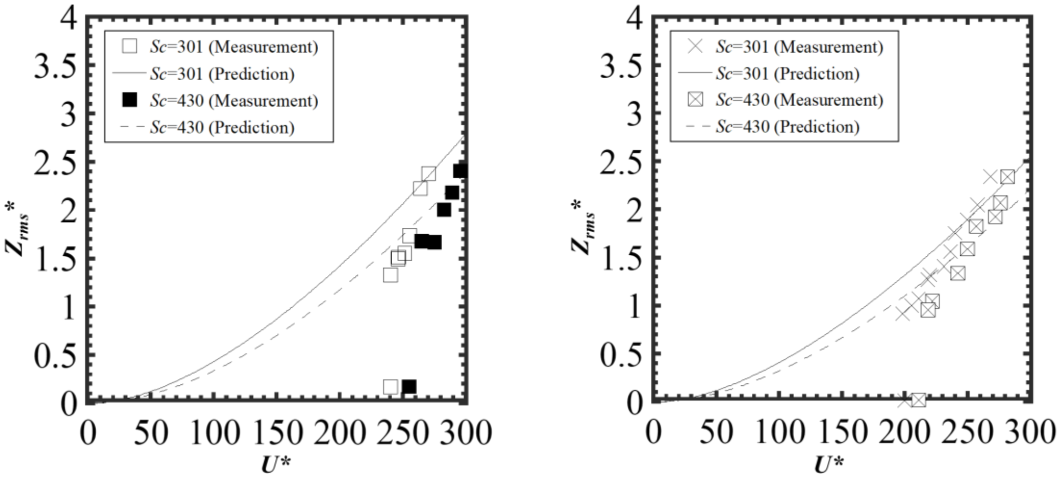

(a) *s/d* = **0.5** (b) *s/d* = **0.6**

Fig. 6-12 Z_{rms}*vs. *U**for Model II at *Sc* = 301 and 430 (comparison between measurement and prediction)

6.4 Chapter 6 Conclusion

In the development of the wind turbine driven by the longitudinal vortex in the previous study, it was shown that the driving force is generated by the stationary formation of NV. In other words, when the upstream cylinder of the crossed cylinder-plate moves along the downstream plate, two longitudinal vortices, NV and TV, are formed at a stationary position with respect to the moving upstream cylinder, and the asymmetric pressure distribution caused by NV exerts a fluid force on the cylinder in the moving direction.

This phenomenon raises the idea that the static formation of NV destabilizes the motion of a cylinder and causes a new type of fluid-elastic unstable vibration (FEV) when the cylinder is elastically supported. In this chapter, we measured the fluid force acting on the circular cylinder blade of a wind turbine type hydrodynamic force measurement system and investigated the vibration behavior of a pendulum type amplitude measurement system by wind tunnel experiments. As a result, the following conclusions were obtained.

1) It was confirmed that the range of gap ratio s/d and velocity ratio λ (= moving speed of the cylinder/velocity of the flow) required to generate the fluid force acting on the cylinder in the direction of rotation correlated well with the operating range of the circular cylinder blade wind turbine.

2) The mechanism of hydrodynamic force generation was confirmed to be the steady formation of NV, which periodically vanishes when λ is smaller than a certain threshold.

3) Cross-flow oscillations of a cylinder in a pendulum-type amplitude measuring apparatus were observed in the range of s/d and λ *required* for fluid force generation. This oscillation was classified as galloping because it has a feature commonly observed in galloping of a single cylinder in a uniform flow.

4) Based on the quasi-steady theory, we proposed an analytical method to predict the vibration amplitude using the equation of the fluid force coefficient proposed in the previous study.

5) The oscillations of the pendulum-type amplitude measuring device were well predicted by the above method using the experimental equation of the fluid force coefficient, whose constant was determined from the experimental results of the wind turbine-type fluid force measuring device.

Thus, it is confirmed that the oscillations of the crossed circular cylinder-flat plate system are caused by the static formation of NV and are classified as galloping, although galloping does not occur in a single cylinder due to its axisymmetric cross-sectional shape. In addition, the measurement results of the fluid force showed that the direction of the fluid force coincided with the direction of rotation of the circular cylinder blade wind turbine. This will enable us to set the appropriate rotational speed against the mainstream speed when designing a practical wind turbine.

Chapter 6 References

Azhar, M., Sheikh Ahmad Zaki, Shirakashi, M., Mohamed Sukri Mat Ali, Muhammad Zulfahmi Samsudin, Ahmad Faiz Mohammad, Experimental investigation on vortex-induced vibration and galloping of rectangular cylinders of varying side ratios with a downstream square plate. J. Wind Eng. Ind. Aerodynamics, 211, 104563, (2021) 27 pages.

Hemsuwan, W., Sakamoto, K., Takahashi, T., Lift force generation of a moving circular cylinder with a strip-plate set downstream in a cruciform arrangement: flow field improving using tip ends, International J. Aeronautical and Space Sciences, 19 (3), (2018) 606-617.

Hemsuwan, W., Sakamoto, K., Takahashi, T., A longitudinal vortex wind turbine: Effect of the blade length. Springer, Fluid-Structure-(2019) pp.117- 123, Sound Interaction and Control.

Kawabata, Y., Takahashi, T., Haginoya, T., Shirakashi, M., Interference effect of downstream strip-plate on the crossflow vibration of a square J. Fluid Science and Technology, JSME, 8 (3) (2013) 348-363.

Sakamoto, K., Hemswan, W., Takahashi, T., Development of a wind turbine driven by longitudinal vortex: Wind tunnel experiment to investigate the basic J. Wind Eng. Ind. Aerodynamics, 210, 104492, (2021)15 pages.

7. Generation of Fluid Force Oscillation due to Wind Direction in a Longitudinal Vortex Driven Horizontal Axis Circular Cylinder Blade Wind Turbine

7.1 Chapter 7 Introduction

In this chapter, the wind direction characteristics of a circular cylinder blade wind turbine, which is a horizontal axis wind turbine, are discussed. When the main flow is not parallel to the rotational axis of the wind turbine but with a specified yaw angle, a complicated three-dimensional detachment of the flow occurs on the blade surface. The power generation efficiency of the wind turbine decreases with the increase of the yaw angle, and the load due to the yaw moment acts on the blade, which greatly reduces the life of the wind turbine. Zhanwei et al. (Zhanwei et al., 2020) conducted an experiment on the load acting on the blade and the power output when there is inflow in the yaw direction, and showed that the axial inflow decreases with the yaw angle θ, and the power output decreases by more than 30 % at θ=30 deg. Xiaodong et al. (Xiaodong et al., 2019) also reported that the torque fluctuation due to the inversion of the yaw direction velocity increases as the yaw angle increases. In order for the Necklace vortex to exert a steady hydrodynamic force on the circular cylinder blade, the relative angle of attack, which is given by the main flow and the blade velocity (in the case of the wind turbine, the tip velocity in the vicinity of the wake ring plate), is important and the hydrodynamic force is given as a function of the relative angle of attack. The existence of yaw causes the relative angle of attack to change with the angle of rotation during one rotation of the blade. Depending on the main flow velocity and yaw angle, an angular range in which the stable formation of Necklace vortices is inhibited is expected to occur. From the above, the effect of yaw angle is different from that of general propeller type horizontal axis wind turbine in principle.

The purpose of this chapter is to measure the hydrodynamic forces on a single circular cylinder blade during one rotation around its axis of rotation, and to clarify the effects of the main flow velocity, rotational speed and yaw angle on the variation of the hydrodynamic forces with rotation angle. A motor is attached to the rotor shaft of a circular cylinder single-blade wind turbine, and the torque acting on the rotor shaft is measured while the blade is forced to rotate at a predetermined speed in the main stream at a constant speed. First, the relationship between the relative angle of attack of the wind and the hydrodynamic force on the circular cylinder blade is evaluated when the main flow is in the same direction as the axis of rotation, i.e., when the yaw angle is zero, and a model is constructed to predict the hydrodynamic force on the blade by two-dimensional geometrical considerations when the yaw angle is given. Furthermore, the relationship between the rotation angle of the circular cylinder blade and the fluid force is measured experimentally and compared with the model. The stable formation, disappearance, and re-formation of Necklace vortices when the yaw angle is not zero but the relative angle of attack changes during rotation are investigated in detail.

7.2 Experimental procedure

The experiments were conducted using the blowout type wind tunnel apparatus shown in Section 2.1. A single circular cylinder blade wind turbine and a single blade wind turbine with a counterweight on one side and a counterweight on the other side were used as wind turbines as shown in Section 2.2.1. In a given uniform flow field, a motor rotates a circular cylinder blade at an arbitrary speed to set an arbitrary speed ratio, and the fluid force acting on the cylinder is measured. The azimuth angle φ of the blade represents the angle of rotation of the blade in this device. A single circular cylinder blade wind turbine is used to measure the hydrodynamic force at θ=0 deg, and a single blade wind turbine is used to measure the hydrodynamic force by changing θ.

7.3 Results and Discussion

7.3.1 Prediction equation for fluid force acting on a circular cylinder blade and extension of the prediction equation for yaw angle

The results of this study are evaluated by the velocity ratio λ, which is calculated from the mainstream velocity U and the wind velocity V' *in the* rotational direction generated by the rotational motion of the wind turbine. The velocity ratio λ *is* defined as the ratio of the tip velocity of the blade tip to the wind speed in an ordinary horizontal axis wind turbine, while in a circular cylinder blade wind turbine, the velocity ratio λ is defined as the ratio of the tip velocity of the circular cylinder blade to the wind speed at the center of the width of the ring-shaped plate because the formation condition of the Necklace vortex that generates the rotational force is related to the relative velocity between the ring-shaped plate and the circular cylinder blade. Fig.7-1 shows the definition of the relative wind speed U_r for θ=0 deg. The velocity ratio is defined by the following equation.

$$V = -V' = \pi D \frac{m}{60} = \pi Dn \tag{7-1}$$

$$U_r = \sqrt{U^2 + V^2} \tag{7-2}$$

$$\lambda = \frac{V'}{U} = \frac{\pi Dn}{U} \tag{7-3}$$

The force acting on the blade of the wind turbine is evaluated using the fluid force coefficient C_z defined by Equations (7-4) and (7-5).

$$T = \frac{D}{2} \cdot F \tag{7-4}$$

$$C_z = \frac{F}{\frac{1}{2}\rho R d U^2} \tag{7-5}$$

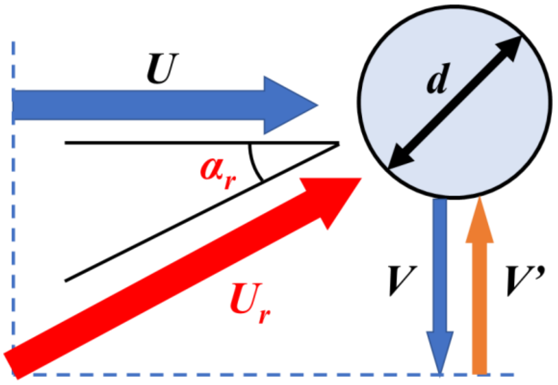

Fig. 7-1 Definition of relative wind velocity for a circular cylinder blade wind turbine.

In order to obtain the basic characteristics of a wind turbine, i.e., the λ-C_z relation when the main flow is parallel to the axis of rotation, i.e., θ = 0 deg, an experiment was conducted using a single circular cylinder blade with L = 220 mm. In the experiment, the wind speed is set to a predetermined value, and the torque is measured at a predetermined speed given by the motor (predetermined speed ratio λ*), and* C_z is calculated. Fig.7-2 shows the relationship between λ and C_z. When C_z is in the first and third quadrant, it means that the positive hydrodynamic force acts on the circular cylinder blade in the moving direction. This means that U and λ In other words, under the conditions of U and λ in these regions, the blade receives a force in the acceleration direction. Looking at the measured C_z, it can be seen that C_z does not exist in these regions near λ = 0 deg for any U*, and* that the steady lift due to the Necklace vortex is not generated. At U=5 m/s, the range where the Necklace vortex does not form is very narrow and the maximum of C_z is observed at λ=0.05. At U=10 m/s and 15 m/s, C_z is stable up to λ=0.1 and above. At U=10 m/s and 15 m/s, stable vortex formation does not occur until λ=0.1 or higher, but as λ *is* increased, C_z plots on the same line as at U=5 m/s. These results indicate that the stable formation of Necklace vortices requires a velocity ratio above a certain value of λ*, and the* value depends on the mainstream velocity. In the E region shown in Fig.7-3, the Necklace vortex does not form stably and the wind turbine loses its rotational force, while in the B and C regions, the Necklace vortex exerts hydrodynamic force in the direction of rotation. On the other hand, in regions A and C, the fluid force opposite to the direction of rotation acts on the blade to suppress the rotation. If there are no mechanical frictional forces or air resistance acting on the rotation of the blade, the blade rotates at λ *where* the λ-C_z straight line shown as a straight line in Fig. 7-3 intersects the boundary between the B and A regions, i.e., the horizontal axis showing C_z= 0. The blade cross-section of the circular cylinder blade wind turbine driven by the Necklace vortex is symmetrical to the direction of

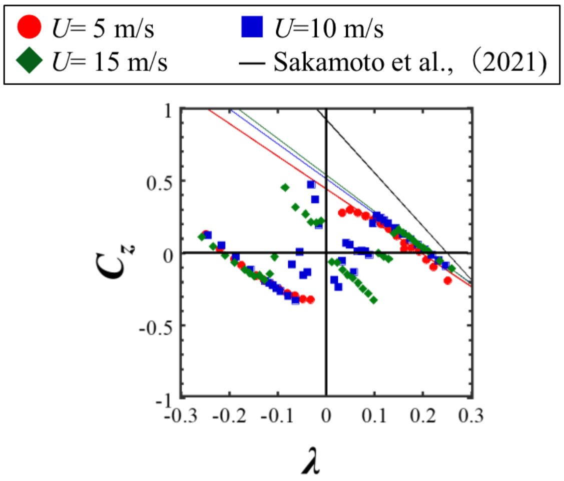

Fig. 7-2 Linear approximation of fluid force to velocity ratio. It shows that the stable formation of Necklace vortex requires a tip velocity above a given λ, and the value depends on the mainstream velocity.

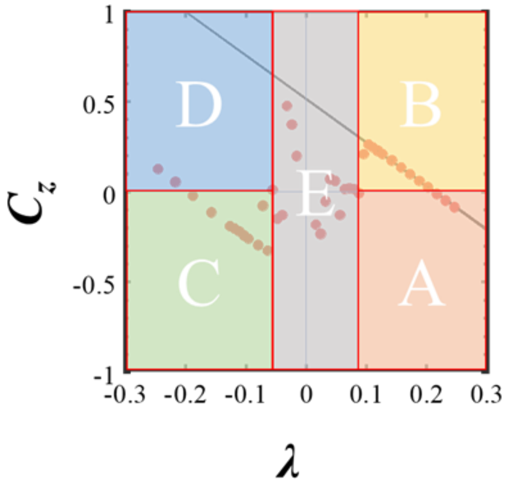

Fig. 7-3 Generation of longitudinal vortices in each region of λ-C_z. Assuming that there are no frictional forces or air resistance acting on the rotation of the blade, the straight line λ-$C_z$indicates that the blade rotates at λ intersecting the horizontal axis, which indicates the boundary between regions B and A, i.e., C_z=0.

rotation. This characteristic can be understood from the fact that Fig. 7-2 and Fig. 7-3 are axisymmetric with respect to the coordinate origin.

In order to predict the hydrodynamic force acting on a circular cylinder blade, the relationship between λ and C_z is modeled and expressed by a simple equation. The range of the E region, where the stable formation of Necklace vortices does not occur, varies with the flow velocity but is omitted for simplicity. The values of C in regions A to D, i.e., regions where the wind turbine rotates stably, are obtained as a function of λ. In these regions, the value of $C_z$decreases linearly with the increase of the absolute value of λ. *Therefore, it is* expressed by the following equation (7-6).

$$C_z = \begin{cases} -(Ca - Cb\lambda) & (\lambda < 0) \\ 0 & (\lambda = 0) \\ Ca - Cb\lambda & (\lambda > 0) \end{cases} \tag{7-6}$$

The coefficients C_a and C_b in Equation (7-6) are obtained from the results of each wind speed test conducted under the condition of yaw angle θ = 0 deg shown in Fig.7-2. As shown in Fig.7-2, the coefficients C_z and C of Eq. (7-6) do not depend greatly on the change of *U* in the range of A to D, i.e., the moving range of the wind turbine, but each coefficient increases slightly with the increase of *U* as shown in Fig.7-4. However, the coefficients increase slightly with the increase of U as shown in Fig.7-4. By considering the dependence of wind speed *U,* the equations for the two coefficients are obtained as follows.

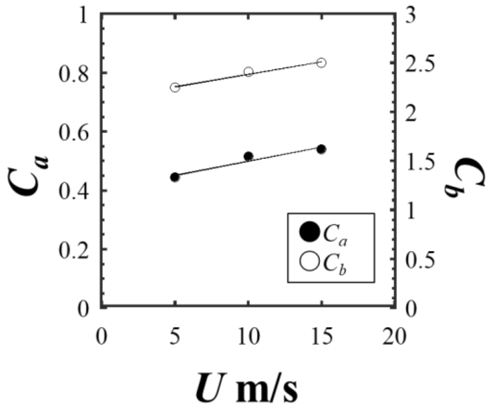

Fig. 7-4 Coefficients $C_a$and C_b in approximation Eq. (6) for lift coefficient λ-C_z.

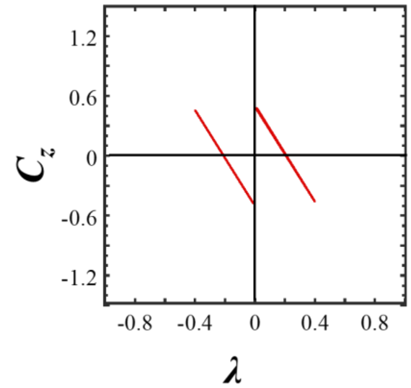

Fig. 7-5 Prediction of λ-C_z at θ=0 deg (U=10 m/s, m=192 rpm). Although $C_z$is predicted even near λ=0 deg, the lack of steady lift in the E region indicates that there is an effective lower limit for λ in this model.

$$C_a = 0.40 + 0.0096U \tag{7-7}$$

$$C_b = 2.1 + 0.025U \tag{7-8}$$

By substituting Equations (7-7) and (7-8) into Equation (7-6), C_z at $\theta = 0$ deg can be predicted. The relationship between λ and C_z calculated in the range of $\lambda = \pm 0.04$ under the conditions of main flow velocity $U = 10$ m/s and rotational speed $m = 192$ rpm is shown in Fig.7-5. Although C_z is predicted in the vicinity of $\lambda = 0$ deg in Fig.7-5, there is an effective lower limit for λ in this model because no steady lift is generated in the E region. The experimental expression for $\lambda_{\min}$ (7-9) was obtained by reading the smallest velocity ratio at which C_z occurs, i.e., the lower velocity ratio λ_{min}, from the values in the first quadrant of the results shown in Fig. 7-2 and considering the dependence of U.

$$\lambda_{min} = 0.01U + 0.0005 \tag{7-9}$$

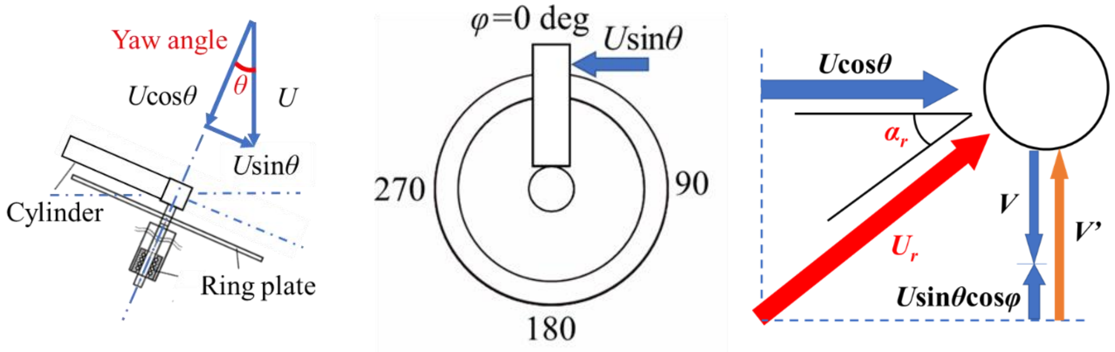

(a) Top view of wind velocity flowing into the rotating surface. **(b) Feont view of a wind turbine subjected to crosswind due to yaw** **(c) Relative wind velocity varying with yaw angle.**

Fig. 7-6 Effect of yaw angle on flow field and relative wind velocity.

Fig.7-6(a) shows a top view of a wind turbine with yaw angle θ set. Fig.7-6(a) shows a view of the wind turbine from above with the yaw angle θ set so that the direction of the main flow *U is* zero when it is perpendicular to the rotational axis of the wind turbine and positive when it is tilted to the left. Fig.7-6(b) shows a view of the rotational surface of the circular cylinder blade from vertically upstream, where the azimuth angle φ=0 deg is set when the blade is vertically upward and positive when it is tilted to the right. Fig.7-6(a) shows the figure when the circular cylinder blade is at φ=90 deg, and the wind speed of *Usinθ* acts in the radial direction. In Fig.7-6(b), the blade is located at φ=0 deg, and the wind speed of *Usinθ acts in the* rotational direction. Fig.7-6(c) shows the view of the circular cylinder blade in (b), and the wind velocity component related to the rotation of the blade is shown. Equation (7-10) shows the variation of λ' with azimuth angle φ in response to the change of yaw angle θ. Equations (7-11) and (7-12) show the extended expressions of equations (7-7) and (7-8).

$$\lambda' = \frac{V'}{U} = \frac{(\pi Dn + U\sin\theta\cos\varphi)}{U\cos\theta} \tag{7-10}$$

$$C_a = 0.40 + 0.0096U\cos\theta \tag{7-11}$$

$$C_b = 2.1 + 0.025U\cos\theta \tag{7-12}$$

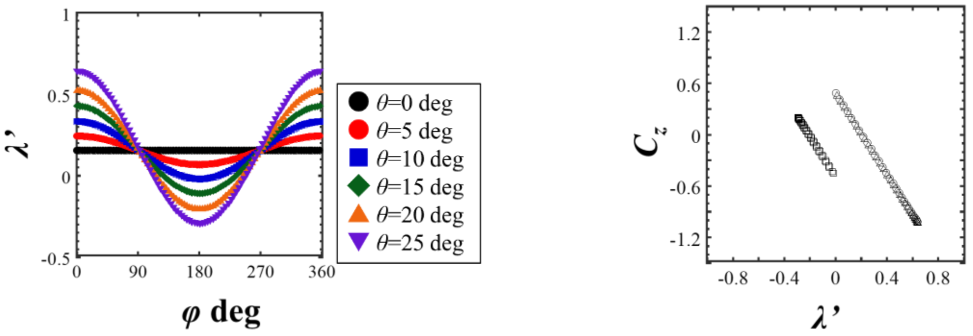

(a) Relationship between azimuth angle of blade and effective velocity ratio by yaw angle.

(b) Prediction of λ-C_z in the presence of yaw angle (θ=25 deg).

Fig. 7-7 Relationship between azimuth angle and velocity ratio for wind turbine with set yaw angle and prediction of fluid force against effective velocity ratio (U=10 m/s, m=192 rpm).

These prediction equations consider only the two-dimensional velocity component in the cross section perpendicular to the central axis of the circular cylinder blade, and neglect the spanwise velocity component. These prediction models are obtained from two-dimensional simplified geometric factors.

λ' was calculated from equation (7-10), and C_z was calculated by substituting equations (7-11) and (7-12) into equation (7-6). The relationship between the change in λ' during one rotation of the circular cylinder blade and λ'-C_z at θ=25 deg was calculated and is shown in Fig. 7-7. The relationship between λ' and λ'-C at θ=25 deg is shown in Fig.7-7. The φ-λ' shown in Fig.7-7(a) indicates that λ' *increases and decreases* in a positive range at θ=5 deg, while λ *is* constant at θ=0 deg. ' increased and decreased in a positive range at θ =5 deg. Fig.7-7(b) shows the prediction of the change of C_z in the range of increase and decrease of λ' at θ=25 deg. Fig.7-7(b) shows that when the yaw angle is not zero, the rotor rotates at a constant speed ratio in the right direction, but there are regions C and D shown in Fig.7-3, i.e., regions where the fluid force corresponding to the fluid force generated by the left rotation of the blade acts.

7.3.2 Comparison of predicted and measured fluid force against yaw angle

Fig.7-8 shows the results of the torque T obtained for different azimuth angles φ. At $\theta = 0$ deg, T *is* almost zero regardless of φ. At $\theta = 5$ deg, T is sinusoidal with a minimum torque at $\varphi = 0$ deg and a maximum torque at $\varphi = 180$ deg. When λ' is the smallest, it is the maximum torque. As θ increases, the torque increases rapidly toward φ=180 deg. At θ=25 deg, the torque reaches its maximum value around φ=120 deg to 180 deg and decreases rapidly at φ It can be seen that the torque increases rapidly in this region. It is considered that the Necklace vortex disappears in this region.

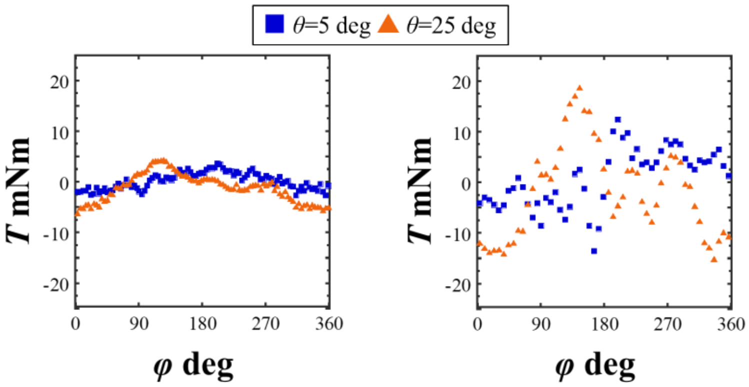

(a) *U*=10 m/s (b) *U*=16 m/s

Fig.7-8 Measurement results of the relationship between azimuth angle and torque. At $\theta = 5$ deg, the waveform is sinusoidal, with the minimum torque at $\varphi = 0$ deg and the maximum torque at $\varphi = 180$ deg. The maximum torque is obtained when λ' is the smallest. For θ=25 deg, the torque reaches its maximum value around φ=120 deg to 180 deg, and drops sharply for φ above that value. In this region, the Necklace vortex is considered to have disappeared.

Fig.7-9 shows the results of λ'-C_z measured for each yaw angle for U=10 m/s. The results for θ=5 deg in Fig.7-9(a) show that the predicted equations exist in the first and fourth quadrants and the measured results are consistent with the predicted equations. The results for θ=5 deg shown in Fig. 7-7(a) are also in accordance with the prediction equation because the range of $\lambda' > 0$. The results for

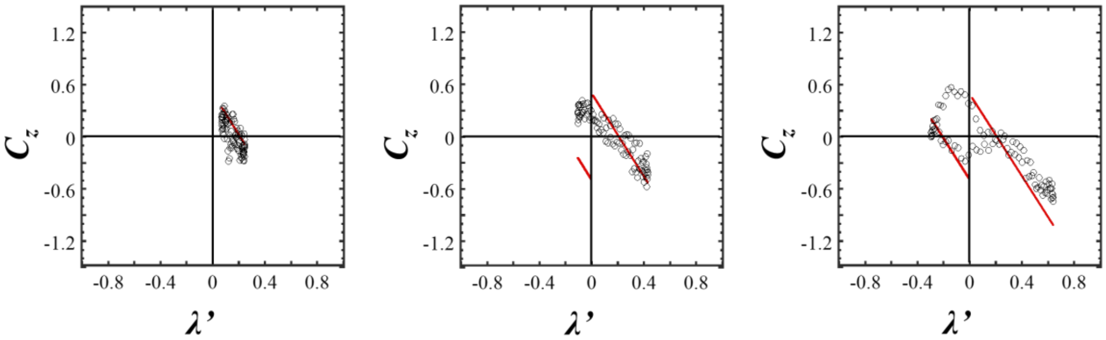

(a) θ=5 deg. (b) θ=15 deg (c) θ=25 deg

Fig. 7-9 Relationship between effective velocity ratio λ' and fluid force coefficient C_z (*U*=10 m/s). For θ=5 deg, the measurement results also agree with the trend of the prediction equation, and for θ=15 deg, the trend of increasing torque with decreasing λ' agrees with the prediction equation. For θ=25 deg, the results show that C_z is consistent with the predicted equation for λ'>0 and λ'<0. When going from the region of λ'>0 to below λ'=0, C_z increased to the extension of the predicted equation for C_z, and C_z changed to match the predicted equation for the range of λ'<0.

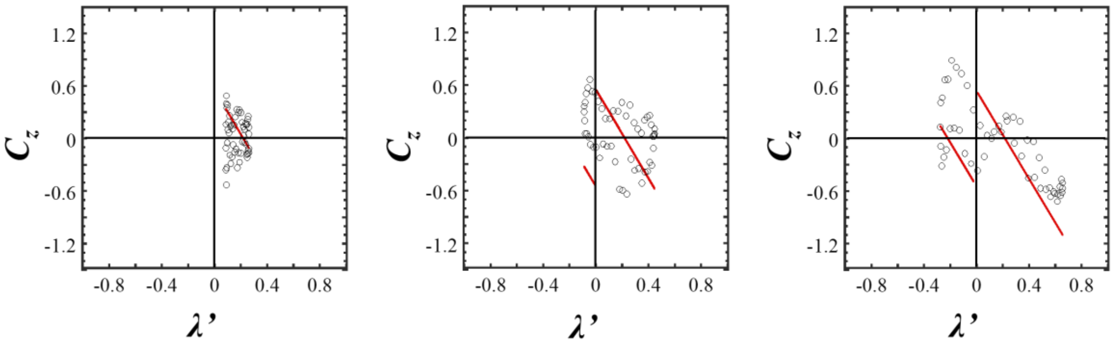

(a) θ=5 deg (b) θ=15 deg (c) θ=25 deg

Fig. 7-10 Relationship between effective velocity ratio *λ'* and fluid force coefficient C_z （*U*=16 m/s）. For *θ*=5 deg, the trend of *λ'*- C_z is consistent with that for *U*=10 m/s. For *θ*=15 deg, the results were closer to the predicted equation in the region of *λ'*<0, and C_z in the third quadrant was obtained. The plots appearing as an extension of the approximate equation when *λ'* changes negatively persisted through the lower range of *λ'*.

θ=15 deg shown in Fig. 7-9(b) show that the tendency of the torque to increase with decreasing *λ'* is consistent with the prediction equation. Fig.7-9(b) shows the results for *θ* =15deg. For θ=25 deg shown in Fig.7-9(c), the results for *λ'*> 0 and *λ* From the region of *λ'*> 0 to below *λ'*=0, C_{zz} increases to the extension of the predicted equation for C_z, and C changes to match the predicted equation for the range of *λ'*< 0. When C_z increases from *λ'*< 0 and exceeds *λ'*=0, C does not match the prediction equation from the middle of the prediction equation, and tends to approach the prediction equation in the range of *λ'*> 0. In the results for U=16 m/s shown in Fig.7-10, the trend of *λ'*-C_z is consistent with that for U=10 m/s. In the case of U=16 m/s shown in Fig.7-10, the trend of λ '-C is consistent with that of U=10 m/s. The results for θ=15 deg shown in Fig.7-10 (b) are closer to the prediction equation in the region of *λ'*<0, and $C_z$in the third quadrant is obtained. The results for θ=25 deg shown in Fig.7-10 (c) are compared with the results for U=10 m/s, and the trend of *λ* 's negative value, the plots of the approximate equation are persistent until the lower range of *λ'*. These results indicate that when the positive and negative values of *λ'* are reversed by adding the yaw angle, *C* does not $_z$change immediately according to the prediction model, but changes gradually under the influence of the Necklace vortex that had been generated until then.

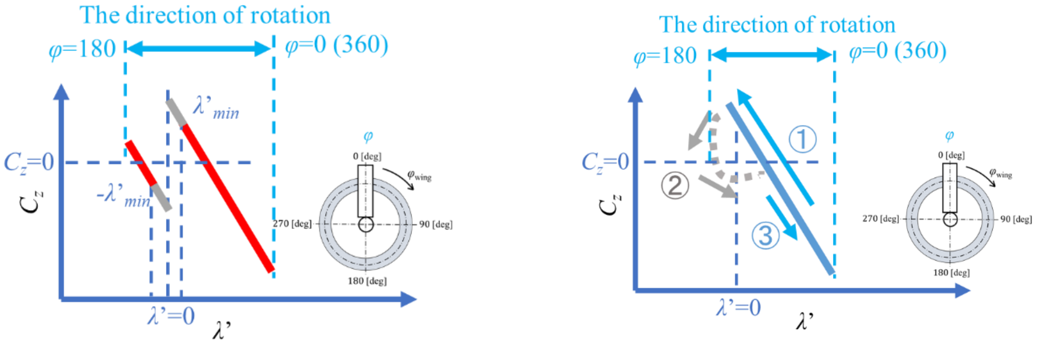

(a) Prediction of effective velocity ratio and fluid force coefficient by eq. (6).

(b) Tendency of the fluid force coefficients obtained in the experiment to the effective velocity ratio.

Fig. 7-11 Relationship between effective velocity ratio and fluid force coefficient corresponding to azimuth angle.

The relationship between the azimuth angle of the circular cylinder blade and the Necklace vortex is discussed from the results of λ'-C_z obtained so far. As shown in Fig.7-7(a), λ' is maximum at φ=0 deg and minimum at φ=180 deg, and the λ'-C_z diagram is shown in Fig.7-7(b). Fig.7-11(a) shows the predicted λ'-C_z diagram by substituting equations (7-11) and (7-12) into equation (7-6). The process of φ progressing from 0 to 180 deg is predicted by the prediction line where λ Fig.7-11(b) shows the experimental schematic of λ '-C_z obtained from the experiment. The steady lift due to the Necklace vortex is generated in the region (1) and disappears in the region (2). In the region of (2), even though λ' is the same as in (1), the rotation angle is different from that of (1) and is affected by the yaw angle, so there is a fluid force that is not represented in the prediction model.

Fig.7-12 shows a schematic diagram of the Necklace vortex outflow region based on the results

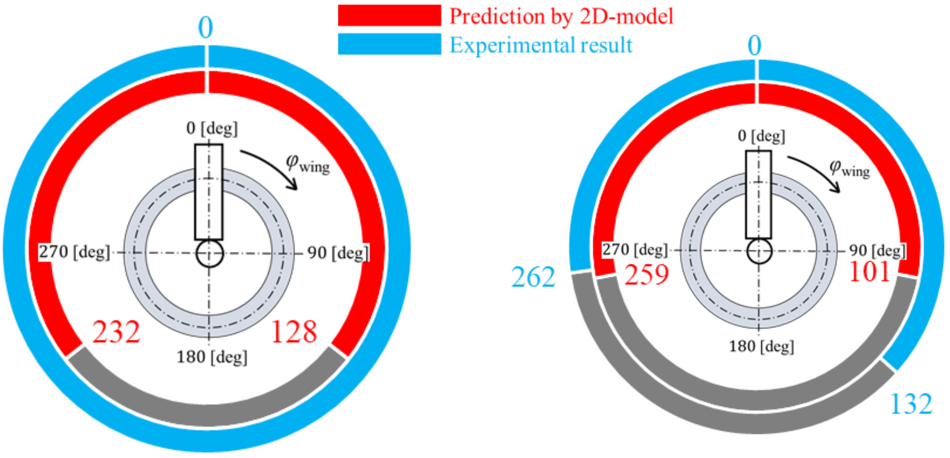

(a) θ=5 deg

(b) θ=25 deg

Fig. 7-12 Relationship between azimuth angle and longitudinal vortex in a wind turbine with a yaw angle (U=10 m/s).

obtained in Fig.7-9(a) and (c). The inner red region is the region where the hydrodynamic force due to the Necklace vortex is generated, which is calculated from equations (7-6) to (7-9), the prediction model obtained from the two-dimensional relative velocity components to the circular cylinder blade. The outer light blue region shows the range of the fluid force acting in the direction of rotation obtained from the experiment. Fig.7-12(a) shows the results for θ=5 deg. The predicted model shows that the Necklace vortex does not form stably in the angle range from 128 deg to 232 deg. In the case of θ=25 deg shown in Fig.7-12(b), the stable formation region of Necklace vortex ends at 101 deg in the prediction model, but in the experiment, the Necklace vortex continues to form until 132 deg. On the contrary, the Necklace vortex re-formed at 259 deg in the predicted model, but it re-formed at 262 deg in the experiment, which is later than the predicted model. In other words, the Necklace vortex may disappear and re-form during one rotation due to the change of the relative angle of attack caused by the change of λ' caused by the yaw angle, and these changes are affected by the previous state. These changes are affected by the previous state. The Necklace vortex maintains its formation state for a long time even after the disappearance condition is satisfied. On the other hand, the re-formation of Necklace vortices takes a short time after the condition is satisfied.

Based on the relationship between λ'-C_z obtained from the experiment, the Necklace vortex state was examined in more detail and classified into five angular regions based on the characteristics of the fluid force acting on the circular cylinder blade. The relationship between λ'-C_z, rotation angle and these angular regions is shown in Fig.7-13, and the details of the angular regions focusing on the outflow of the Necklace vortex and the direction of the fluid force are shown in Table 1. When the wind turbine is forced to rotate clockwise at a constant speed, the five angular regions are as follows. The five angular regions are as follows: A') Necklace vortices follow the right rotation, but the fluid force acts in the direction to suppress the rotation, B') Necklace vortices follow the right rotating circular cylinder blade and the fluid force acts in the direction to accelerate, C (C') A longitudinal vortex is generated in the direction of rotation of the circular cylinder blade and the fluid force acts in the direction of impeding the rotation, (D') A longitudinal vortex is generated in the direction of rotation of the circular cylinder blade but the fluid force acts in the direction of accelerating the rotation, (E') The Necklace vortex does not form stably. (E') Necklace vortex does not form stably. The next section describes the 12 angular regions based on the characteristics of λ'. Let n be the speed at which the wind turbine rotates without any load such as bearing friction for a given wind speed, and let λ'_n be the speed ratio at this time. λ' when C_z is the maximum is λ'_{czmax}, and λ' when C_z is the minimum in the third quadrant is λ '. In the third quadrant, when C is the minimum value, λ' is λ'_{czmin}. (1) is the same as region A', where λ' is positive and C_z becomes negative because the fluid force in the deceleration direction increases as λ' increases. (2) and (3) show the range where the fluid force increases in the region $0 < \lambda' < \lambda'_n$, but in the case of $\theta = 0$ deg, the rotation occurs only in the range from λ'_{min} to λ'_n obtained from equation (7-9). (2) and (3) are distinguished by using λ'_{min} as a boundary.

(4) and (5) are regions with negative λ' where the effect of (3) persists and drives when θ is large. Similarly to (3), (4) and (5) are regions where Necklace vortices do not occur when $\theta = 0$ deg. The region (6) is the region where the rotation is sustained due to the effect of the maximum C_z in (5), and the Necklace vortex disappears because C_z is positive but decreases rapidly with rotation. The Necklace vortex disappears because C is positive but decreases rapidly with rotation. ⑦ is the range where C_z becomes positive according to Equation (6), which appears in the region where λ' is negative when the yaw angle is large. In ⑦, the Necklace vortex that disappeared in ⑥ reappears, but it is formed in the forward direction of the cylinder rotation because λ' is negative. In (8) and (9), the forward vortex formed in (7) is within the range that impedes the rotation. The plots of ⑧ and ⑨ are symmetrical around the origin of ② and ③, respectively. In ⑩ to ⑫, the forward Necklace vortex that inhibited the rotation until ⑨ disappears. The combined range of ⑨ and ⑩ is the same as that of (3), but divided because the Necklace vortex disappears in the range of $\lambda_{czmin}' < \lambda'$. In the case of $\theta = 0$ deg, the relationship between λ and C_z is plotted on a graph as shown in Fig. 7-3, and it is point symmetric around the origin. On the other hand, when the yaw angle is added, the positive and negative values of λ' are reversed during one rotation to the right as shown in Fig. 7-13(a). In other words, the outflow position of the Necklace vortex reverses from the backward to the forward direction of the cylinder.

Furthermore, comparing the part of $\lambda' < 0$ in region B' with $\lambda' > 0$ in E', the plot is not origin-symmetric even when$|\lambda'|$ is equal. This can be attributed to the fact that λ' fluctuates periodically, and the position of the Necklace vortex differs between the front and the rear of the circular cylinder blade

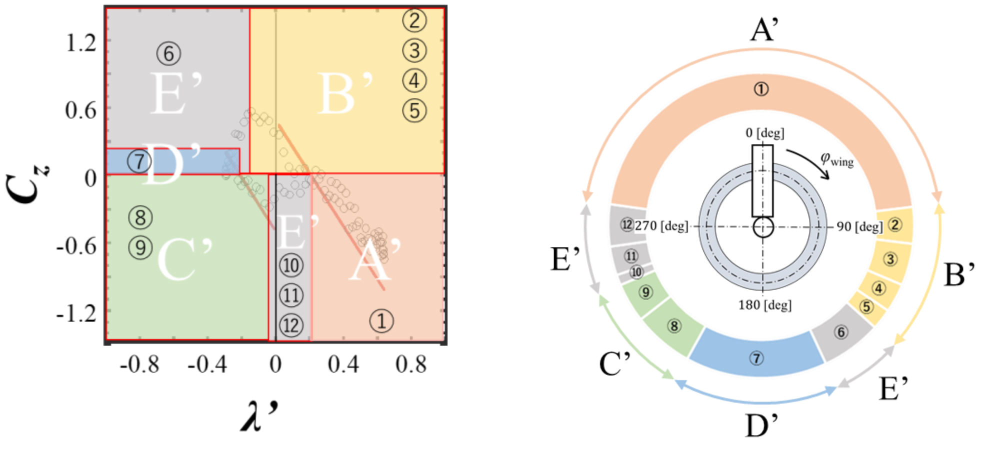

(a) Generation of longitudinal vortices in each region of λ'-C_z in a wind turbine with a yaw angle.

(b) Relationship between the tip velocity ratio corresponding to the azimuth angle and the region of longitudinal vortex generation.

Fig. 15 Effect of yaw angle on driving force generated by longitudinal vortex.

depending on λ', and it is driven by the influence of the front.

The five angular regions related to the hydrodynamic force and the twelve regions related to the Necklace vortex formation, λ', may all or only some of them appear depending on the yaw angle, wind speed and rotational speed of the circular cylinder blade. Therefore, it is clarified that the power characteristics of the circular cylinder blade driven by Necklace vortices are more complicated than those of ordinary propeller type wind turbines in relation to yaw angle.

Table 1 Classification of azimuth angle by distribution of fluid force coefficient against velocity ratio.

Region	State number	Effective velocity ratio	Fluid force
A’	①	$\lambda'_n < \lambda'$	$0 > C_z$
B’	②	$\lambda'_{min} < \lambda' < \lambda'_n$	$C_z > 0$
B’	③	$0 < \lambda' < \lambda'_{min}$	$C_z > 0$
B’	④	$-\lambda'_{min} < \lambda' < 0$	$C_z > 0$
B’	⑤	$\lambda'_{czmax} < \lambda' < -\lambda'_{min}$	$C_z >0$
E’	⑥	$\lambda' < \lambda'_{czmax}$	$C_z > 0$
D’	⑦	Area close to Eq （6）	$C_z > 0$
C’	⑧	$\lambda' < -\lambda'_{min}$	$0 > C_z$
C’	⑨	$-\lambda'_{min} < \lambda' < \lambda'_{czmin}$	$0 > C_z$
E’	⑩	$\lambda'_{czmin} < \lambda' < 0$	$0 > C_z$
E’	⑪	$0 < \lambda' < \lambda'_{min}$	$0 > C_z$
E’	⑫	$\lambda'_{min} < \lambda'$	$0 > C_z$

7.4 Chapter 7 Conclusion

The relative angle of attack derived from the velocity ratio determined by the wind speed and the tip speed of the circular cylinder blade is an important factor for the stable formation of the Necklace vortex which is the power source of the circular cylinder blade wind turbine. In this study, the possibility that the Necklace vortex does not form stably was examined. In this study, the velocity ratio and the hydrodynamic force acting on the circular cylinder blade were measured in the wind in the direction of the axis of rotation of the wind turbine, i.e., $\theta = 0$ deg, and a prediction model were proposed to represent the change of the hydrodynamic force coefficient with the rotation of the circular cylinder blade in the situation where the yaw angle was given. The model shows that as the yaw angle increases, there exists an angular region where the stable formation of Necklace vortices is difficult during one rotation of the circular cylinder blade. The experimental verification confirmed the existence of this region and showed that the region corresponded to the prediction model to some extent. However, it is also found that some complicated phenomena occur that do not match the prediction. It was found that the formation or disappearance of the Necklace vortex was affected by the previous vortex state even though it was formed or disappeared in the predicted model. Furthermore, it was found that the time required for the formation of the Necklace vortex was much shorter than the time required for the disappearance of the Necklace vortex, indicating that the Necklace vortex has a strong property of maintaining its shape. Based on the experimental results, the characteristics of the hydrodynamic forces acting on the circular cylinder blade were classified into five angular regions and based on the characteristics of the effective velocity ratio considering the yaw angle, the classification was made into 12 angular regions. Depending on the yaw angle, wind speed and rotational speed of the blade, all of these regions may appear or only some of them may appear. Therefore, the yaw angle characteristics of the circular cylinder blade wind turbine driven by the Necklace vortex are found to be very complicated.

Chapter 7 References

Xiaodong, W., Zhaoliang, Y., Shun, K and Hui, H., Investigations on the Unsteady Aerodynamic Characteristics of a Horizontal-Axis Wind Turbine during Dynamic Yaw Processes, Energies, Vol. 12, No. 16 (2019) DOI: 10.3390/en12163124

Zhanwei, L., Binrong, W., Xingjan, D., Zhike, P., Yegao, Q., Wenming, Z., Aerodynamic and aeroelastic characteristics of flexible wind turbine blades under periodic unsteady inflows, Journal of Wind Engineering & Industrial Aerodynamics, Vol. 197 (2020) DOI: 10.1016/j.jweia.2019.104057

8. Conclusion

In this study, the generation mechanism of longitudinal vortices acting hydrodynamic forces on a crossed plate - cylinder system was clarified, and experiments and numerical analyses were carried out to improve the performance considering practical conditions of wind power generation.

In Chapter 1, the vortex excitation phenomenon, which is an important engineering problem, and its examples are described first, and the main countermeasures are also described. Next, the control method of the longitudinal vortex excitation phenomenon, which was developed from the control of the Kalman vortex excitation, is described. In addition, the development process of the circular cylinder blade wind turbine driven by the longitudinal vortex, which is the subject of this study, is described. In addition, the position of the circular cylinder blade wind turbine is shown by explaining the general wind turbine and the power generation using the vortex oscillation which is paid attention in recent years.

In Chapter 2, we summarize the experimental apparatus used in this paper and describe the basic experimental method.

In Chapter 3, the effect of the shape factor of the blade tip on the power characteristics of a circular cylinder blade wind turbine was clarified by measuring the rotation speed and torque of a circular cylinder blade driven by a longitudinal vortex with a drag reducing component such as an end plate attached to the blade tip through wind tunnel experiments. The installation of an end-plate at the blade tip of a circular cylinder blade wind turbine enables the turbine to rotate stably at a low speed even at high loads, and also to increase the maximum speed by reducing the drag at high speeds. In the case of a disk end plate, the torque coefficient can be improved by up to 20% by attaching a disk end plate with a diameter 2.5 to 3 times the diameter of the cylinder to the outer blade tip only. In the case of multi-blades, the improvement effect may decrease with larger diameter end plates as the number of blades increases.

The purpose of Chapter 4 is to reduce the size of the flat part of the crossed cylinder-flat plate system in consideration of the increase in the number of blades and the size of the circular cylinder blade wind turbine. The position of the outflow of the longitudinal vortex was confirmed by visualization of the wind turbine with fin-shaped plates, and the necessary length of the plates behind the rotating direction was examined. Similarly, the outflow position of the longitudinal vortex was confirmed by visualization when the width and angle of the upper part were changed, and the effect of the increase in the flow rate to the intersection on the outflow position of the longitudinal vortex was clarified. From the results, it was suggested that the fin-shaped plate could increase the dynamic pressure from the main flow and also increase the suction force of the longitudinal vortex. In addition, it is possible to reduce the size of the plate without losing the torque, which means that the wind load on the wind turbine pole can be greatly reduced when it is enlarged.

In Chapter 5, the frequency characteristics of the torque during steady-state rotation and the stability of the torque against the change of rotation conditions are investigated in order to clarify the suitable driving conditions for the wind turbine from the torque fluctuation of the circular cylinder blade wind turbine. First, the frequency characteristics of the periodic fluctuation of the fluid force due to the longitudinal vortex were obtained from the experiment. From the results, it was found that the amplitude of the torque fluctuation increased significantly when the frequency of the harmonic component of the fluctuation caused by mechanical factors and the fluctuation component caused by the longitudinal vortex matched. Next, to clarify the temporal characteristics of the power of the circular cylinder blade wind turbine, experiments were conducted by changing the circular cylinder blade diameter, blade length, flat plate width, gap ratio, and initial rotation speed. As a result, it was found that the time constant became shorter in inverse proportion to the magnitude of the fluctuation when moving from low to high rotation, but the opposite was true when moving from high to low rotation.

In Chapter 6, wind tunnel experiments were conducted to confirm that fluid elastic unstable oscillations are induced by stationary NV as suggested in previous studies. First, the fluid force was measured using a wind turbine, and then the vibration behavior was investigated using a pendulum-type amplitude measuring device. Finally, a method to estimate the vibration amplitude based on the quasi-steady theory is proposed and compared with the experimental results. From the results, it is confirmed that the vibration of the crossed cylinder-plate system is caused by the static formation of NV and is classified as galloping, although galloping does not occur in a single cylinder due to its axisymmetric cross-sectional shape.

In Chapter 7, to clarify the behavior of Necklace vortices in response to changes in the flow field due to the yaw angle, a motor was attached to the rotating shaft of a circular cylinder single-blade wind turbine and the blades were forced to rotate at a specified speed. From the relationship between the torque and the blade rotation angle, the relationship between the variation of the velocity ratio and the fluid force was determined. Based on the results, the region of the blade rotation angle related to the stable formation, disappearance and re-formation of the Necklace vortex was investigated. The results show that even if λ' becomes negative at yaw angles $\theta = 5$ and 15 deg, the hydrodynamic force C_z is plotted on a straight line that decreases as $\lambda'|$ increases during one cycle. At θ=25 deg, the absolute value of the hydrodynamic force C_z becomes small due to the large deviation from the straight line in the region where $\lambda'|$ is negative. The Necklace vortex is maintained and the fluid force C_z is continuously generated even when λ' becomes negative, but when the yaw angle becomes large, the Necklace vortex cannot be maintained and a range of rotation angles in which the Necklace vortex is lost occurs, and the wind turbine loses its rotational power. It became clear that

Chapter 8 summarizes the important conclusions of the chapters in this thesis and discusses the evaluation of the steady lift force by the longitudinal vortex acting on the circular cylinder blade and the clarification of the generation mechanism. and stability conditions, so that it can contribute to the improvement of the performance of wind turbine design.

謝辞

本博士論文は多くの皆様のご支援により完成しました．初めに，研究室での 5 年間を通してご指導，温かいご支援，励ましを頂いた長岡技術科学大学機械創造工学専攻の高橋勉教授に心より感謝いたします.

長岡技術科学大学の白樫正高名誉教授には，論文の執筆にあたり，添削や修正，研究や論文の在り方のご指導を頂きました．心より感謝いたします.

そして，審査委員会の長岡技術科学大学技術科学イノベーション専攻の山田昇教授，山崎渉准教授，長岡技術科学大学機械創造専攻の倉橋貴彦准教授，鳥取大学機械物理系学科の原豊教授には大変お世話になりました．すべての審査委員会からの指導とコメントにより，博士論文の質を大きく向上させることができました.

また，実験について多くのご指導とご助言を頂きました山田修一技官，実験の手伝いをして頂いた風組の皆様に感謝いたします.

最後に，研究室で共に過ごした佐藤靖徳先生，斎藤啓太君をはじめとした流体工学研究室の同期，先輩，後輩の皆様に感謝いたします.

2022 年
長岡技術科学大学
仲田翔太